UNIVERSITÀ DELLA CALABRIA

Dipartimento di Fisica

Doctorate School of Science and Technique
"Bernardino Telesio"

A thesis submitted for the degree of Doctor of Philosophy in Science and Technology of Mesophases and Molecular Materials

XXVI Cycle

SSD FIS/07 (02/B3)

"Strategies to control linear anisotropy and chirality in polymeric materials: from the basic issues to the micro-devices developments"

School Director
Prof. Roberto Bartolino

Curriculum Coordinator
Prof. Carlo C Versace

Supervisor
Prof. Gabriella Cipparrone

Candidate
Dr. Eugenia Lepera

December 2013

Abstract

The development of devices with increasing levels of functionality represents an important technological issue. To this aim, innovative materials with tunable functionalities play a crucial role. The challenge is to obtain multifunctional materials through simple procedures with high performance and low cost, and eventually external control parameters. Moreover the understanding of multifunctionality of materials is hence an exciting scientific opportunity. For these purpose, the main objectives of the present work have been to explore two main strategies.

In the first one, azobenzene based materials and their light induced functionalities has been exploited to develop microdevices for polarimetric applications. Already know effects of linear and circular photoinduced optical anisotropies in azobenzene based polymers was investigated coupling the materials properties with holographic techniques, both to characterize the photoinduced properties of the materials and to develop diffractive devices useful for the above cited applications.

The second topic is addressed towards the development of a materials science approach to build up polymeric matrices with controllable supramolecular chiral structures and subnanometric cavities. Both explored features are connected to intriguing topics as chirality and small size cavities. Their chirooptical properties and supramolecular structures suggest high potentiality for development of chiral sensors or filtration devices.

Key words: micro-devices, azo-polymers, polarization holography, syndiotactic polystyrene, supramolecular chirality.

Contents

0 Introduction and objective 1

1 Polarization holograms for micro-devices developments 5

1.1 Introduction 7

1.2 Polarization Holography 8

1.3 Polarization sensitive materials 13

1.3.1 Azo-compound 14

1.3.2 Liquid Crystals 16

1.4 Experimental Part I: 20

Cycloidal Optical Axis Gratings

1.4.1 Polarization Hologram 21

1.4.2 Materials 25

1.4. 3 Experiment 28

1.4.4 Fabricating of high quality cycloidal OAG 29

1.4.5 Results: characterization of grating structures and diffraction 33

1.5 Experimental Part II: 45

Spatial light modulator-assisted polarization holography

1.5.1 Microlens Array holograms 46

1.5.2 Writing the MA and results 50

1.6 Spectro-polarimetric applications of OAGs 58

1.6.1 Circular Dichroism spectrograph 59

1.6.2 Two-grating photopolarimeter 60

1.7 Conclusions 63

References 65

2 Advanced Materials based on chiro-optical supramolecular architectures 71

2.1 Introduction 73

2.2 Guest-Host strategy 74

2.2.1 Syndiotactic polystyrene (s-PS) 75

2.3 Experimental section 80

2.3.1 Chiral recognition and quantification 80

2.3.2 Induction of chirality with a non-racemic guest 82

2.3.3 Stable supramolecular chirality 89

2.3.4 Guest exchange with achiral chromophores 92

2.4 Conclusions and perspectives 100

References 102

3 Photo-induced linear and circular birefringence in azo-polymers 107

3.1 Introduction 109

3.2 Functionalized polymeric materials 110

3.3 Experimental Part I: 112

Intrinsic and induced anisotropy analysis

3.3.1 Theoretical model 114

3.3.2 Materials: Chiral/achiral liquid crystal azo-polymers. 120

3.3.3 Experiment and Results 122

3.5 Conclusions and perspectives 131

References 132

4 Summary 135

List of Publications 138

Introduction

The development of devices with increasing levels of functionality currently represents an important issues of the research, where innovative materials play a key role. To this aim the modern materials science has moved toward the study and the processing of materials exhibiting well-defined and complex functionalities, and organic molecular materials have attracted considerable interest. The attention to these materials, driven by their light-weight and by unique mechanical properties, as the prospect of manufacturing flexible and low-cost devices, is primarily due to the possibility to design molecules with properties tailored for specific applications, that can give rise to intermolecular interactions with high added value. Among these materials, multifunctional materials are especially of interest owing to the fine control of their functions. The ability to transform the functionalities of molecules into the macroscopic properties of a material will offer significant advantages in the development of functional devices. The distinct change in the macroscopic properties of polymers can be mediated by different strategies, here were investigated two of them.

The first strategy is to utilize external stimuli (such as polarization and intensity of light and electric fields) to directly mediate the macroscopic change in the structures, functions and properties of materials. Photo-irradiation, which represents a most fascinating external stimulus, is a precise and efficient method for the chemical-physical proprieties control of properly functionalized materials and to induce linear and circular anisotropies in polymers. For this purpose we used photosensitive aligning organic materials for the realization of highly stable and efficient polarization gratings. Among the many polarization-sensitive materials, azobenzene-containing media have been investigated intensively during the last years, and remains the most efficient for this purpose. The gratings will be achieved by a polarization holographic technique by recording polarization holograms in azodye photo-aligning substrates for liquid crystalline materials. The holograms recorded on the substrates can work as a template for the LC film, either in low molar mass liquid crystal cells or in reactive mesogen layers, and orient the nematic director parallel to the local easy axis becoming as a replica of the polarized hologram and amplifying the diffraction efficiency of the resulting pattern. The stability of the recorded gratings and the high induced birefringence of the liquid crystalline

material, open up the possibility of interesting applications, as the development of microdevices for polarimetric applications and microlens array. In order to analyze and characterize the formation of structures connected to the birth of linear and circular birefringence, different azo-polymers have been investigated. The photo-induced anisotropies obtained by irradiating polymers by single beam with different polarization states have been studied and the issues related to the circular anisotropies and chirality were analyzed.

The second strategy is to utilize the enantiomeric interaction between polymers and guest chiral molecules to trigger a stepwise conformational change in polymers, which then results in transformation of macroscopic properties. In particular, chirality has been induced in melt extruded syndiotactic polystyrene (s-PS) films of different thickness, by co-crystallization with a non-racemic guest (R or S carvone). The induction and amplification of chirality in the syndiotactic polystyrene (s-PS) by co-crystallization with non-racemic guest molecules occurs by a supramolecular mechanisms, involving the formation of non-racemic helical crystallites based on a racemic unit cell (including both right- and left-handed polymer helices, δ phase). The supramolecular nature of the induced chiral response of s-PS is also confirmed by the intense chiral optical response of achiral chromophores (azulene and 4-nitro-aniline), when they replace the non-racemic guest in the crystalline cavities of s-PS co-crystalline phases. The low cost, commercial availability, robustness and easy melt processing of the polymer are expected to facilitate design and production of chiral optical materials and devices, based on co-crystalline phases of s-PS with achiral o racemic chromophores.

It is worth to underline that this work deals not only with basic research on the materials and on the strategies used to control linear anisotropy and chirality of polymeric materials, but also design and implementation of the new micro-devices.

Overview of this study:

Chapter 1: the first chapter deals with polarization holography recording on an azo-compound photoisomerizable system. We describe the properties of the material chosen for the holographic recording, and the two methods used to record polarization holograms: a conventional polarization holography and a spatial light modulator (SLM)-assisted holographic

recording. The first method was adopted to generate pure phase polarization holograms with high efficiency, *cycloidal optical axis gratings* (OAG), while several programmable *microlens array* (MA) with different focal length and shapes was generated using the second one. We experimentally investigate two viable approaches to produce cycloidal OAGs: nematic LC OAG and reactive mesogen RM OAG. The characterization of this device revels that the singular diffraction features and the long time stability, make it particularly appropriate for polarimetric investigations.

Chapter 2: in the second chapter we start with a short introduction to the characteristics of the investigated polymer, i.e. syndiotactic polystyrene (s-PS). We describe how is possible to induce chirality in s-PS films by a non-racemic guest and the exchange of the non-racemic guest with achiral chromofores.

Chapter 3: in the final chapter are reported preliminary investigations on photoinduced anisotropies, performed on chiral and achiral liquid crystal azo-polymers. We measure the intrinsic and the induced optical anisotropy of the materials using the polarization grating (OAG).

Scope of the thesis

Today's market for optical components and systems calls for innovative products that are small, light, more powerful, faster and cheaper to produce. Innovative materials with tunable functionalities play a crucial role to meet these demands, especially where established polymer processing methods and technologies enable high-quality, high functionalities and high volume production at low cost. Thus, the main objective of this work is to obtain multifunctional/structured materials with high performance through simple procedures and low cost exploiting different strategies.

Polarization holograms for micro-devices developments

1.1 Introduction

In this chapter we discuss the possibility to obtain highly efficient liquid crystal based polarization gratings, exploiting polarization holographic technique, in order to achieve optical elements for the development of micro-devices.

Taking advantage of the interactions at the interface between a holographic patterned substrate and a thin film of liquid crystal, we obtain diffractive devices characterized by high diffraction efficiency, low scattering and whose diffracted and transmitted beams can be modulated in intensity by means of a low external voltage[1]. The idea of our work is based on the fact that holograms recorded on some photosensitive material provide a periodic alignment to liquid crystalline materials (LC). This effect originates from the anisotropic van der Waals interactions between elongated partially conjugated liquid crystal molecules and strongly conjugated molecules[2-4]. Therefore, recording the holographic grating on a polarization sensitive photoanisotropic material and putting the grating in contact with the liquid crystal, we expect that the latter to reorient according to the polarization pattern and then to amplify the diffraction properties of the grating.

In this chapter, we shall examine first the principles of interference and holography and extend them to the concept of polarization holography. Then, we will describe the two methods used to record polarization holograms: a conventional (or traditional) and a spatial light modulator (SLM)-assisted polarization holography. The standard holographic method consists of overlapping of two laser beams, with orthogonal polarizations and equal intensities, that impinges on a layer of a photosensitive material placed into the interference region. At the same time a generalized and versatile experimental approach has been performed with the aim to realize complex variants of polarization holograms by means of reconfigurable holographic techniques, in real time as well, by using spatial light modulators (SLM) that produce computer generated arbitrary phase pattern.

Using the first method we obtained pure phase polarization gratings in thin films, *cycloidal optical axis gratings* (OAG), while several programmable diffractive *microlens array* (MA) have been produced with different focal length and shapes using the second one. Both are

based on the nematic LC amplification of the optical anisotropy of thin photoaligning layers and will be described in the following sections. We experimentally investigate two viable approaches to produce cycloidal OAGs. In the first case, low molar mass the nematic LC layer, is confined between two parallel substrates, both imposing spatially periodic planar alignment. In the second case, a photopolymerizable liquid crystal (reactive mesogen RM), is spin-coated as thin film on top of a single aligning substrate and then photopolymerized to permanently harden the periodic anisotropic structure. Both approaches share the same photoaligning azobenzene material and deposition procedure[5,6], which enable to obtain high quality thin command layers.

The beauty of the photoanisotropic materials lies in the fact that, since they are sensitive to the polarization of light, its polarization states can be visualized easily. Furthermore, such polarization elements are achromatic, i.e., they can be devised for a broad wavelength range, in which they preserve the diffraction properties and used at a completely different wavelength, differing only in terms of the efficiency, since this depends on the magnitude of the anisotropy. Finally, the stability of the recorded gratings and the light induced functionalities of the selected material has been exploited to develop microdevices for polarimetric applications.

1.2 Polarization Holography

Polarization holography is a very sophisticated and versatile technique that in the last years has demonstrated unique features in several optics, photonics, and spectroscopic applications.[7]

This technique exhibits several unique properties:

- *high efficiency*, which consists in the possibility to achieve theoretically 100% diffraction efficiency even in thin films;
- *special polarization properties*, it is possible to fabricate polarization-sensitive optical elements;

- *achromaticity*, the optical elements fabricated with polarization can be used in a wide wavelengths range.

Before going into details it would be correct to explain the fundamental concepts of *holography*. The holographic method was first proposed by D. Gabor[8] in 1948 and is based on the interference of two waves. The interference of two waves produces a spatially periodic light intensity and/or polarization distribution which, in turn, changes the optical properties of a photosensitive material placed into the interference region. The spatial modulation of the optical material parameters acts as a diffraction grating.
So, the process of creating holographic patterns consists of three steps:

- creating an interference pattern of coherent polarized light,
- capturing the interference pattern in a photo-sensitive film,
- reconstructing the hologram by diffraction of light from this film.

The experimental arrangement for the production of holographically induced optical gratings is sketched in figure 1.1 : light from a coherent source (i.e., laser) is split into two beams 1 and 2, with wave vectors $\bar{k}_1$ and $\bar{k}_2$, electric field amplitudes $\bar{A}_1$ and $\bar{A}_2$, and intensities I_1 and I_2. The two beams intersect at an angle α at the sample and create an interference pattern[9], the grating vector $\bar{q} = \mp(\bar{k}_1 - \bar{k}_2)$.

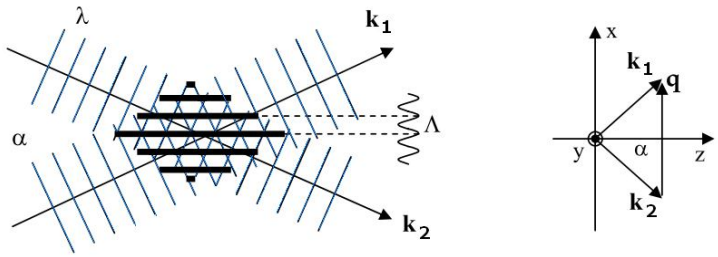

Fig. 1.1: Interference pattern of 2 plane waves with grating production by interference of two light waves and the representation of the k-vectors and definition of the basis and coordinate system.

If the beams (k_1 and k_2) are placed in the *xz*-plane with an angle of α and $-\alpha$ from the *z*-axis respectively, the intensity will be independent of *y* and modulated in the *x*-direction with a periodicity determined by Λ related to $\bar{q}$ in the followed way $\Lambda = 2\pi/|\bar{q}|$, and can be expressed in terms of the wavelength of the writing field and α as $\Lambda = \lambda/[2\sin(\alpha/2)]$.

One of the main advantages of this technique is that different grating spacings can be obtained with a single setup, by varying only the intersection angle of the two beams.

The interference patterns can be created to have spatially periodic intensity modulations and/or spatially varying polarization state. When two coherent beams of arbitrary polarization interfere, the polarization state and the intensity of the total field change spatially in orientation and magnitude because of the phase difference between the two beams.[10]

Afterwards, accordingly to the polarization state of the two interfering beams, it is possible to distinguish two different holographic recordings: purely intensity-modulated interference patterns with constant polarization state (*intensity holography*), and purely polarization-modulated interference patterns with constant intensity (*polarization holography*).

The intensity holography is the modulation of intensity generated by two plane waves with the same polarization. In the following scheme (figure 1.2) few interference patterns are reported, which are produced by pair of beams with equal and parallel polarization states.

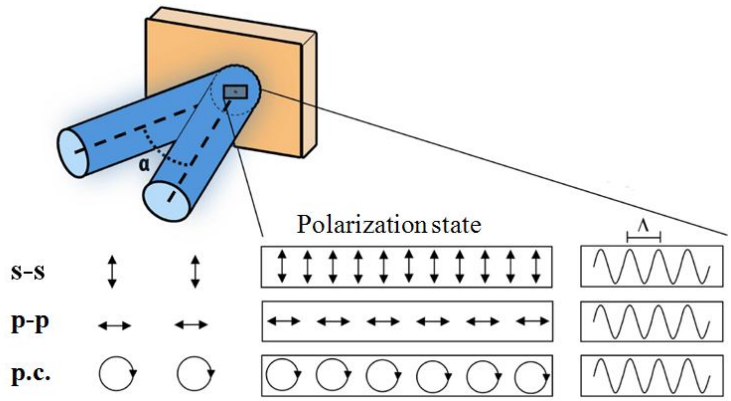

Fig. 1.2: Polarization geometries produced by different pair of beams with parallel polarization states. **s**: linear s; **p**: linear p; **p.c.**: parallel circular.

The figure 1.2 shows the polarization state of the two interfering plane waves and the resulting total field interference pattern. The first three cases (**s-s**, **p-p**, **p.c.**) describe holographic intensity patterns, in which the two recording beams present the same polarization state. The polarization state of the total field is everywhere equal to the writing beams and its direction remains unchanged. The phase modulation between the two interfering beams is encoded as a pure intensity modulation. On the contrary, polarization holography employs beams with two orthogonal polarizations for recording information. Polarization holography has many similarities to intensity holography. Both are pattern transfer techniques that make use of the interference of coherent (laser) light. The period of the holographic structure is determined by the angle and the wavelength of the overlapping plane waves. To record the interference pattern, a light sensitive material is placed into the interference pattern and a corresponding pattern is somehow imprinted (through various mechanisms) in the material. As explained above the difference between polarization holography and intensity holography is the type of modulation. For polarization holography two plane waves interfere with orthogonal polarization states resulting in a modulation of the polarization state, not the intensity. This process was discovered by Sh.D. Kakicheshvili which proposed to make use of the fact that "interference" has vectorial character[11-13] . So, when the interfering wave are orthogonally polarized the interference pattern results modulated and this polarization modulation is a function of the phase difference between the two waves. Some examples of pure polarization modulation are reported in which the light intensity in the interference area is constant and only polarization is modulated.

The last four cases (**s-p**, **±45°**, **o.e.** , **o.c.**), reported in figure 1.3, illustrate holographic polarization patterns, in which the two recording beams have orthogonal polarization states. Unlike the previous case, the spatial intensity distribution is almost uniform, and the phase variation is encoded in the polarization state modulation of the total field. It is important to underline that even in opposite polarizations configurations, the presence of a small intensity modulation depends on the crossing angle, especially in the opposite circular and ±45° configurations, and small crossing angles yield negligible intensity modulations. For large angles of incidence the interference patterns are not so symmetrical. This has been discussed by Eichleret al.[14] and Viswanathanet al.[15]

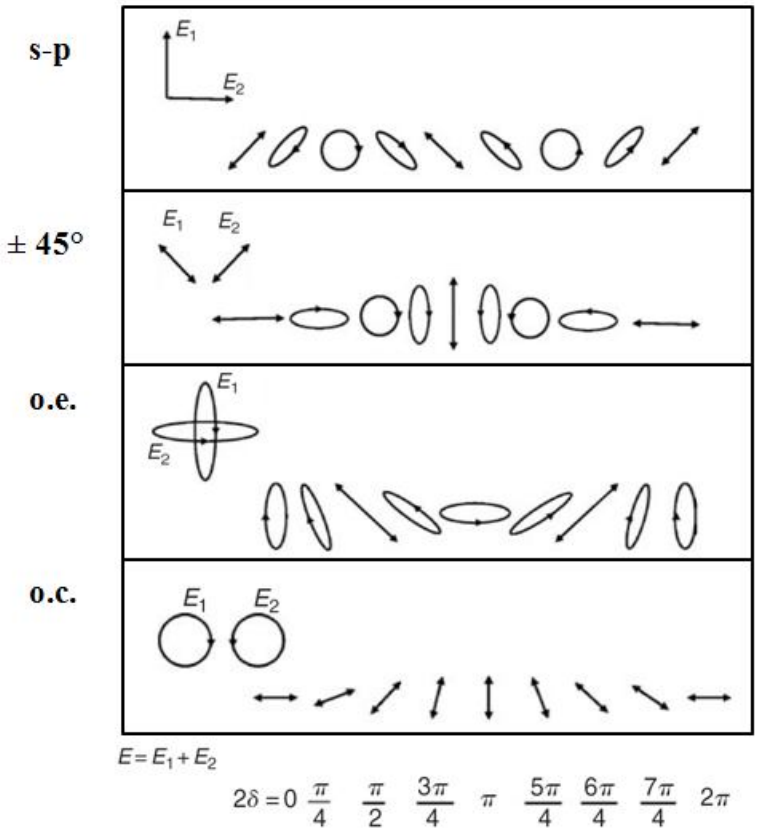

Fig. 1.3: Polarization pattern produced by two waves with orthogonal linear, ±45° linear (**s-p**), elliptical (**o.e**) and circular (**o.c**) polarization and equal intensities The resultant light-field intensity is constant and only the polarization is modulated according to the phase difference 2δ between the two waves.

As a consequence, numerous interfering geometries that produce countless polarization gratings can be obtained simply changing the polarization state of the writing beams. The possibility to have numerous interference patterns depending on the polarization states of the writing waves, represents a great advantage for creation and characterization of diffractive devices for optoelectronics, that makes polarization holography a technique characterized by a very high flexibility.

1.3 Polarization sensitive materials

Recording the interference polarization pattern to form a polarization grating (a modulation of birefringence) requires materials that are sensitive to polarized light. It is obvious that the interference light fields shown in figure 1.3 and previously described could not be fixed in a conventional light-sensitive material, because conventional recording materials are sensitive only to light intensity. Exposed to such an interference pattern they would be uniformly darkened or bleached and there would be no diffraction from them at the reconstruction stage. In order to make use of the polarization modulation it is necessary to use a recording material that has a different response when exposed to light with different polarizations and can record the information about the polarization to form a polarization grating (a modulation of birefringence). Such materials are called *photoanisotropic materials*. When exposed to polarized light they become optically anisotropic and their anisotropy is in accordance with the type and the direction of light polarization. Photoinduced anisotropy was first observed by F. Weigert[16] in 1919 and the ability of a material to exhibit birefringence or dichroism is called the Weigert effect and has been reported in literature since the beginning of the 20th century.[17,18] Many of the known photoanisotropic media have been used in experiments in polarization holography, for example AgCl emulsions, alkali-halide crystals with anisotropic color centers, some chalcogenide materials, and a great number of organic dyes incorporated in solid matrices. In all these materials the polarization modulation in the interference pattern can be encoded as periodic modulation of the induced anisotropy in the optical constants.

Special attention is paid to two classes of materials: azobenzene polymers[19] and liquid crystals[20] , both types of materials embody the periodic anisotropy of polarization holograms differently and are addressed separately in this section.

The *azobenzene-containing polymers* or *compound* are the most efficient and the most studied photoanisotropic material at the moment, that induce birefringence upon irradiation.

1.3.1 Azo-compound

Azobenzene and many of its derivatives have been known and studied for a long time.[21] The molecule consists of an azo-benzene core and terminal constituents R_1 and R_2. The role of the azobenzene core is crucial: under illumination, it manifests reversible trans-cis-trans isomerization. The chemical formula of a generic azo-compound with the trans and cis isomers is shown in figure 1.4:

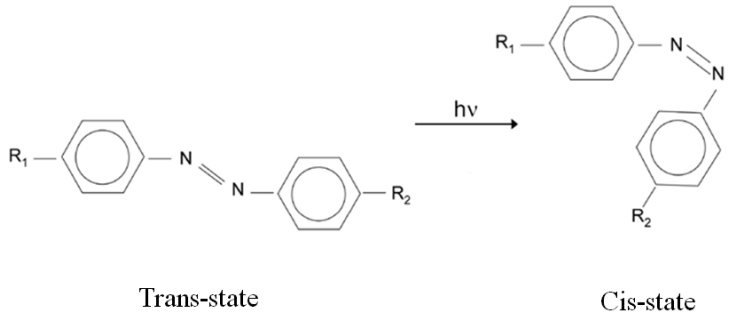

Fig. 1.4 Chemical formula of a generic azo-compound in the trans and cis state.

Photoisomerization is the reversible chemical transformation of a material due to photon absorption, in two different states, trans and cis. After photoisomerization the dye molecule has optical properties distinct from those in its original ground state: for example, the trans and cis states present different absorption spectra.

This photochemical reaction changes only the spatial configuration of the molecule, as demonstrated in figure 1.4. The exact mechanism behind the trans-cis isomerization is not completely understood: both a rotation around the excited N=N bond and an inversion mechanism may be activate in the azobenzene photoisomerization. Whereas the direct reaction

trans-cis is induced by light, the inverse reaction cis-trans can take place both photo-chemically or thermically or occurs spontaneously.

Isotropic dye molecules absorb a photon with equal probability for arbitrary spatial orientation of the linear input polarization but, for a highly anisotropic dye molecule, the absorption cross section depends on the molecule orientation relative to the polarization direction of the light, in addition to its saturating dependence on light intensity. In particular, for anisotropic molecules, the transition probability from the fundamental state to the excited state is proportional to $|\vec{\mu}_{trans} \cdot \vec{E}|^2$, where $\vec{\mu}_{trans}$ is the transition dipole moment of molecule, and $\vec{E}$ is the electric field. Then, when the principal absorption oscillator axis of dye molecule is parallel to the incident polarization direction, the probability for the molecule of absorbing a photon is the highest; the probability is lowest when the oscillator axis is perpendicular to the polarization direction. As a result of this anisotropic transition probability, for uniform orientational distribution, more dye molecules whose absorption axes are parallel to the polarization direction are isomerized than molecules that have other absorption axis orientation. Qualitatively, the explanation of the photoinduced optical orientation can be as follows: because the cis state is thermally unstable at room temperature, the molecules spontaneously go back in the trans state, with the molecular axis oriented casually.[22,23] For prolonged expositions, therefore, the molecules undergo numerous cycles trans-cis-trans. This situation continues until the molecules reorient with the axis orthogonal to the polarization direction: in this case, the molecules have lower probability to be excited. The final result is that the molecules are preferentially oriented with their axis perpendicular to the polarization direction.

In conclusion, photoisomerization is the basic mechanism for the photo induced reorientation of chromophores under action of polarized light and appearance of the corresponding photoinduced optical anisotropy.[10,24,25]

A polarization sensitive photoaligning material, which exhibits photoinduced optical anisotropy and is insoluble in liquid crystals, is needed for polarization holographic recording and for replicating the surface polarization holograms in the liquid crystal bulk.

1.3.2 Liquid Crystals

It is worth nothing that *liquid crystals* (LCs) are state of matter intermediate between that of a crystalline and an isotropic liquid. They possess many of the mechanical properties of liquid, *e.g.*, high fluidity, formation, and coalescence of droplets. At the same time they are similar to crystals in that they exhibit anisotropy in their optical, mechanical, electrical, and magnetic properties. The characteristic feature of LCs is the presence of long-range *orientational* order in the arrangement of constituent molecules, and sometimes one- or two-dimensional quasi long range *translational* or *positional order*. LCs exhibit a great variety of phases, which differ one from another by their structure and physical properties. The main property of a LC is its anisotropy. The optical, mechanical, electrical and magnetic properties of LC medium are defined by the orientation order of the constituent anisotropic molecules. Due to the anisotropy of the electrical and magnetic properties, the orientation of the LC molecules is effectively controlled by weak electric or magnetic fields. As a result, changing the LC molecules orientation, it is possible to change optical, mechanical properties of the medium. All of these are important to the functioning of devices based on LCs: digital watches, calculators, flat TV-displays, thermometers and LC displays are all examples of what LC technology can achieve.

In particular, the liquid crystalline material used belongs to the class of *thermotropic* LCs. Thermotropic LC phases are formed by organic molecules in a certain temperature range and hence the prefix *thermo-*, referring to phase transitions caused by temperature change. About 1% of all organic molecules melt from the solid crystal phase to form a thermotropic LC phase before eventually transforming into an isotropic liquid at still higher temperatures. These mesophase is usually formed by organic materials with anisotropic shape. These molecules usually consist of a central rigid core (often aromatic) and a flexible tail (generally aliphatic groups) as is shown in figure 1.5 where A_1 and A_2 are aromatic rings, Z is the linking group, T_1 and T_2 are the two side-chains. There are three types of thermotropic liquid crystals. These are based on a system proposed by G. Friedel[26] in 1922. They are smectic, nematic, and cholesteric types. They are smectic, nematic, and cholesteric types.

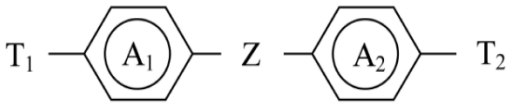

Fig. 1.5 Schematic representation of a generic thermotropic LC.

They differ in order of molecular orientation, due to the tendency of the molecules to arrange themselves in a common direction, and for translational order, which corresponds to the relative position of the centers of mass of the molecules.

On average, the nematic liquid crystals are aligned in one direction. This orientational order results in a preferred direction called the director *n*. The degree of variation from the director can be quantified, and this is done by defining an order parameter. This is done by considering the angle between the director and the molecular axis, θ. Macroscopically the order parameter is defined by[27]

$$S = \langle \frac{1}{2}(\vec{m}\cdot\vec{n})(\vec{m}\cdot\vec{n}) - \frac{1}{2} \rangle = \langle \frac{3}{2} cos^2\theta - \frac{1}{2} \rangle$$

where $\vec{m}$ and $\vec{n}$ are unit vectors in the direction of the molecular axis and the director respectively and θ is an angle between the individual molecular long axis and the director $\vec{n}$. An isotropic fluid would have a value of $S = 0$ and a perfectly orientated solid would have $S = 1$. Liquid crystals typically have values between $S = 0.3$ and 0.8. [28]

The uniaxial symmetry around the director in the LC phase leads to an *anisotropy* in many physical properties. For example, the refractive index, the dielectric permittivity, the magnetic susceptibility, viscosity and conductivity have a different value parallel to the director $\vec{n}$ and perpendicular to it. The LC aligned are therefore *birefringent*, in the sense that exhibit different properties depending on the propagation of light in the medium, with the electric field parallel or perpendicular to the director molecular (or optical axis). In liquid crystals birefringence is a result of the anisotropy of the molecular structure, each bond contributes and the total birefringence can only be determined by summing all of the individual bonds. For example, calamitic liquid crystals are considered to be rodlike. Clearly one molecular axis is much larger than the other two, there is an anisotropy in length and width (see figure 1.6) and in general

there will be different refractive indices associated with the long and short axes of the molecule.

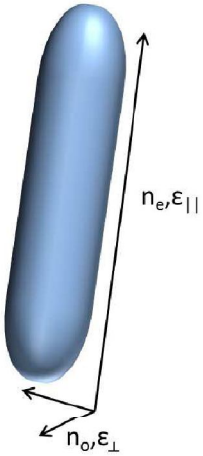

Fig. 1.6 : Thermotropic calamitic liquid crystals molecules can be modeled as rods.

Note, in calamitic liquid crystals this anisotropy is only apparent when the molecules are well ordered. The anisotropic nature of liquid crystals results in different susceptibilities to an electric field,

$$\vec{\varepsilon} = \varepsilon_0(1 + \vec{\chi})$$

$\vec{\varepsilon}$ is the dielectric tensor, ε_0 is the vacuum permittivity and $\vec{\chi}$ is the electric susceptibility tensor. There can be different dielectric constants parallel and perpendicular to the molecular axis. The difference between the two dielectric constants call the dielectric anisotropy, which is given by

$$\Delta\varepsilon = \varepsilon_{\parallel} - \varepsilon_{\perp}$$

where $\varepsilon_{\parallel}$ is the dielectric permittivity along the director and $\varepsilon_{\perp}$ is the dielectric permittivity perpendicular to the director. The difference in dielectric constants means that the response of the molecule to light will depend on its polarization. If the polarization is parallel to the director then the $\varepsilon_{\parallel}$ will be probed whereas, if the polarization is perpendicular then $\varepsilon_{\perp}$ will be probed. If the polarization is not aligned in one of these two directions then, the light is split into two components, one in each of these directions with the relative magnitudes depending on the initial polarization. Each component experiences a different refractive index, parallel and perpendicular to the direction of anisotropy as $n = \sqrt{\varepsilon}$. The difference in the refractive indices is the birefringence, given by

$$\Delta n = n_e - n_o$$

where n_e is the extraordinary refractive index along the molecular axis and n_o is the ordinary refractive index perpendicular to the molecular axis. Most calamitic liquid crystals are uniaxial, i.e. they only have two different refractive indices, one associated with the long molecular axis and the others with the two short molecular axes. It is possible for a liquid crystal to be biaxial, in this case the two orthogonal directions perpendicular to the long molecular axis have different refractive indices to each other and the index associated with the long molecular axis. For positive uniaxial liquid crystals $n_e > n_o$ as shown in figure 1.6.

Birefringence in liquid crystal can be controlled with an aligned layer, an electric field or a flow, but for polarization holograms only an orientation layer is feasible. As the liquid crystal has a very sensitive molecular reorientation easily influenced by external stimuli, its use simplifies the detection of the birefringence changes induced by a photosensitive polymer placed in contact with it.

1.4 Experimental Part I: Cycloidal Optical Axis Gratings

The term probably most used in the literature for the class of optical components that periodically modulate the polarization state of light is Polarization Gratings (PGs). In this section we will describe the properties and illustrate the fabrication of an important subclass of polarization gratings: Cycloidal Optical Axis Gratings (OAG). Holographic OAGs are generally recorded with orthogonal linear or orthogonal circular polarized beams to ensure spatial homogeneity of the light intensity distribution. OAGs recorded with orthogonal circular polarized beams, so-called cycloidal gratings, are the most interesting OAGs. The optical axis orientation in these gratings[29], shown below in figure 1.7, uniformly rotates along the x-axis (i.e., $n(x)$=[cos(πx/Λ), sin(πx/Λ), 0] in the grating plane (*xy*-plane) .

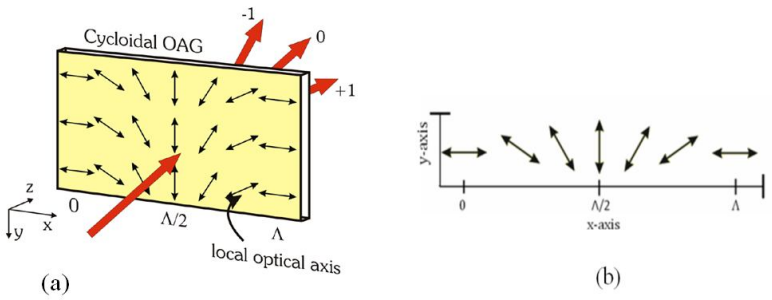

Fig. 1.7 Cycloidal optical axis grating (OAG), in which the local optical axis lies in the plane of the film (xy-plane) and uniformly rotates along the *x*-axis. An optical beam impinging on it is diffracted into the 0- and the ±1-orders only**.**

The ability of Optical Axis Gratings (OAGs) consist in fully transfer the energy of an unpolarized incident light beam into the $\pm 1^{st}$ diffraction orders. Indeed, there are only three beams at the output of cycloidal OAGs: the transmitted (0^{th} order diffraction) and the $\pm 1^{st}$ order diffracted beams. When a light beam with generic polarization impinges on the OAG, the $\pm 1^{st}$

order are always orthogonally circularly polarized and their intensities are proportional to the right-handed (RCP) and left-handed (LCP) circularly polarized light component of the incident beam.

Because of their properties these gratings may have numerous applications in photonic systems and displays,[30-32] including highly efficient projection displays, polarized beam splitting devices, multiplexing and polarization dispersion applications.

While many unique properties have been theoretically identified and compelling applications studied their practical use has been severely limited due the difficulties in producing cycloidal OAGs with optimal performances, such as high polarization contrast and diffraction efficiency, small spatial period, low scattering, chemical, optical and thermal stability.

Our work is based on the creation of liquid crystal based OAGs in which the liquid crystalline materials are aligned using an azodye layer exposed to a polarization interference pattern. In particular, the uniform rotation imposed to the liquid crystal optical axis is obtained in an indirect way: in fact, the periodic alignment previously stored by holographic technique at the aligning surfaces, is transferred to the molecular director of the liquid crystal in the bulk.

1.4.1 Polarization Hologram

When two orthogonally circularly polarized beams with equal intensity overlay at a small angle α, the resulting modulation pattern can be evaluated in the following way:[33,34] if $\vec{E}_{LCP}$ is the field of the left circularly polarized wave and $\vec{E}_{RCP}$ is the field of the right circularly polarized wave, the resulting field is linearly polarized but rotates along the grating wave vector with a constant angular frequency (induction of a periodically modulated birefringence), and can be written as:

$$\vec{E}_{TOT} = \vec{E}_{LCP} + \vec{E}_{RCP} = \frac{1}{\sqrt{2}}\begin{pmatrix}1\\ i\end{pmatrix}e^{-i\delta} + \frac{1}{\sqrt{2}}\begin{pmatrix}1\\ -i\end{pmatrix}e^{i\delta} = \sqrt{2}\begin{pmatrix}\cos\delta\\ \sin\delta\end{pmatrix} \qquad (1.1)$$

where

$$\delta = \frac{2\pi}{\lambda}\sin\frac{\theta}{2}x = \frac{\pi}{\Lambda}$$

is the phase difference at the location *x* of the writing wave.

The transmission matrix of the recorded polarization grating J^{OAG} can be obtained as:

$$J^{OAG} = R^{-1}JR \tag{1.2}$$

where

$$R = \begin{bmatrix} \cos\theta & \sin\theta \\ -\sin\theta & \cos\theta \end{bmatrix} \tag{1.3}$$

describes a rotation through an angle θ

and

$$J = \begin{bmatrix} e^{i\Delta\phi} & 0 \\ 0 & e^{-i\Delta\phi} \end{bmatrix} \tag{1.4}$$

is the transmission matrix that describes the linear birefringence, with

$$\Delta\phi = \frac{\pi\,\Delta nd}{\lambda}$$

in which is contained the information related to the refractive index, Δn is the *photoinduced birefringence*, d is the thickness of the film and λ is the wavelength of the writing waves.[35] Finally, we obtain for the transmission matrix of the polarization grating J^{OAG} the following form:

$$J^{OAG} = \begin{bmatrix} \cos(\Delta\phi) + i\sin(\Delta\phi)\cos qx & i\sin(\Delta\phi)\sin qx \\ i\sin(\Delta\phi)\sin qx & \cos(\Delta\phi) - i\sin(\Delta\phi)\cos qx \end{bmatrix} \quad (1.5)$$

where

$$q = \frac{2\pi}{\Lambda}$$

and

$$\cos qx = \cos\frac{2\pi x}{\Lambda}$$

describes the spatial periodicity of the grating. This means that the polarization grating behaves as a medium whose optical properties, as for example the refractive index *n*, change periodically along *x*. If a monochromatic plane wave

$$\vec{E}_{IN} = \begin{pmatrix} \tilde{E}_x \\ \tilde{E}_y e^{i\delta} \end{pmatrix} \quad (1.6)$$

arbitrarily polarized, in which $\tilde{E}_x$ and $\tilde{E}_y$ are the components of the field along the *x* and *y* axes, and δ is the phase difference between the two components, impinges at normal incidence on the grating, using the above transmission matrix J^{OAG} we obtain the expression of the light field just after the grating:

$$\vec{E}_{out} = J^{OAG}\vec{E}_{in} = \begin{bmatrix} \cos(\Delta\phi) + i\sin(\Delta\phi)\cos qx & i\sin(\Delta\phi)\sin qx \\ i\sin(\Delta\phi)\sin qx & \cos(\Delta\phi) - i\sin(\Delta\phi)\cos qx \end{bmatrix} \begin{pmatrix} \tilde{E}_x \\ \tilde{E}_y \end{pmatrix} =$$

$$= \cos(\Delta\phi)\begin{pmatrix} \tilde{E}_x \\ \tilde{E}_y e^{i\delta} \end{pmatrix} + i\frac{\sin(\Delta\phi)}{2}\begin{bmatrix} e^{iqx} + e^{-iqx} & ie^{-iqx} - e^{iqx} \\ ie^{-iqx} - e^{-iqx} & -e^{iqx} + e^{-iqx} \end{bmatrix}\begin{pmatrix} \tilde{E}_x \\ \tilde{E}_y e^{i\delta} \end{pmatrix} \quad (1.7)$$

The terms containing e^{iqx} and e^{-iqx} represent the waves diffracted into the +1 and -1 orders, the term with $\cos(\Delta\phi)$ represents the zero order.[36-38] Using the Jones formalism, the three waves $\vec{E}_0$, $\vec{E}_{+1}$ and $\vec{E}_{-1}$ can be written as:

$$\vec{E}_0 = \cos(\Delta\phi)\begin{pmatrix}\tilde{E}_x\\ \tilde{E}_y e^{i\delta}\end{pmatrix}$$

$$\vec{E}_{+1} = i\,\frac{\sin(\Delta\phi)}{2}(\tilde{E}_x - i\tilde{E}_y e^{i\delta})\begin{pmatrix}1\\ -i\end{pmatrix}$$

$$\vec{E}_{-1} = i\,\frac{\sin(\Delta\phi)}{2}(\tilde{E}_x + i\tilde{E}_y e^{i\delta})\begin{pmatrix}1\\ i\end{pmatrix} \tag{1.8}$$

It is possible to see that the zero order wave is the same as the incident wave except for the amplitude factor $\cos(\Delta\phi)$; moreover the +1 order is a left circularly polarized wave, but it is proportional to the right component of the incident wave; the -1 order is a right circularly polarized wave, but it is proportional to the left component of the incident wave. For linearly polarized probe beam, the intensities of the first orders are equal

$$I_{+1} = I_{-1} = I_0\frac{(sin\Delta\phi)^2}{2} \tag{1.9}$$

and the corresponding diffraction efficiencies, defined as the ratio of the first diffracted beam intensity to the total incident intensity, are

$$\eta_{+1} = \eta_{-1} = \frac{I_{+1}}{I_0} = \frac{I_{-1}}{I_0} = \frac{(sin\Delta\phi)^2}{2}$$

$$\eta_0 = cos^2(\Delta\phi) \tag{1.10}$$

For a circular incident wave, only the +1 or -1 order appears depending on its handedness; in particular, if the probe beam is left circularly polarized the diffracted beam is right circularly polarized with intensity $I_{+1} = I_0(sin\Delta\phi)^2$, whereas when the incident probe beam is right circularly polarized the diffracted beam is left circularly polarized and the intensity is equal to $I_{-1} = I_0(sin\Delta\phi)^2$. For both cases, the diffraction efficiency is $\eta_{\pm1} = (sin\Delta\phi)^2$.

For an elliptical polarization state of the probe beam we observe a different intensity of the two diffracted beams, but their sum $\eta_{+1} + \eta_{-1}$ remaining constant. Due to the above described behavior of the grating we can conclude that this kind of device is able to recognize the polarization state of a light beam that impinges on it. The transmitted waves obtained in the polarization grating are multiplied for the amplitude factors, $\cos(\Delta\phi)$in the zero order wave and $(sin\Delta\phi)^2/2$ in the ±1-orders waves: they describe the characteristic of the material used and the variations induced by the writing light field.

As it is well know, the diffraction efficiency $\eta_{\pm1}$ in the first order spots and the zero order diffraction η_0, can be controlled by the photo induced optical anisotropy $\Delta n = n_e - n_o$ of the photosensitive material and by the thickness of the film d through the value of its phase retardation $\Delta\phi$.[39-41]

1.4.2 Materials

The dichroic azobenzene dye used in this work belongs to the class of sulphuric bis-azobenzene dyes which are drawing interest as photoaligning agent for low-molecular-weight LCs, polymeric and polymerizable LCs, because of their photosensitivity, high thermal, photochemical and electrochemical stability. The chemical formula of the azodye P4G is reported in figure 1.8:

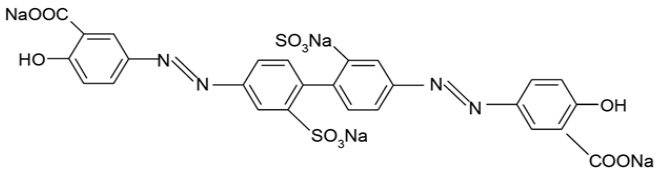

Fig. 1.8: Chemical formula of P4G.

In figure 1.9, is reported the absorption spectrum of the azodye P4G, in which the writing wavelength $\lambda = 457\ nm$ and the probe beam wavelength $\lambda = 632{,}8\ nm$ are highlighted.

The photoinduced alignment of a liquid crystal on azo-dye films and new photoaligning materials has been subject of extensive researches for the liquid crystal display applications,[42] because photo alignment is a non contact method which enables the creation of high quality orientation of the liquid crystal layer without mechanical damage of the substrate, electrostatic charge or dust contamination. The quality of the photoaligned cells based on photochemical reactions proves to be very high,[43] and the substances developed can be classified by the physical origin of the photoaligning phenomenon. In fact, there are several photo chemical reactions involved in the photoalignment phenomena: reversible cis-trans isomerization, photodimerization or crosslinking and photodegradation. The photosensitive azo compounds are known to produce alignment of the liquid crystal director as a result of the reversible cis-trans isomerization chemical reaction. But, in case of P4G[43] both photochemical reactions and cis trans-isomerization should not significantly contribute to the photo-induced reorientation in azodye. One of the possible photoaligning mechanisms in films of P4G is a pure reorientation of the azo dye molecules.[43] When the azo dye molecules are optically pumped by a linearly polarized light beam, the probability of reorientation is proportional to the square of cosine of the angle between the absorption oscillator of the azo dye molecules and the polarization direction of the light.

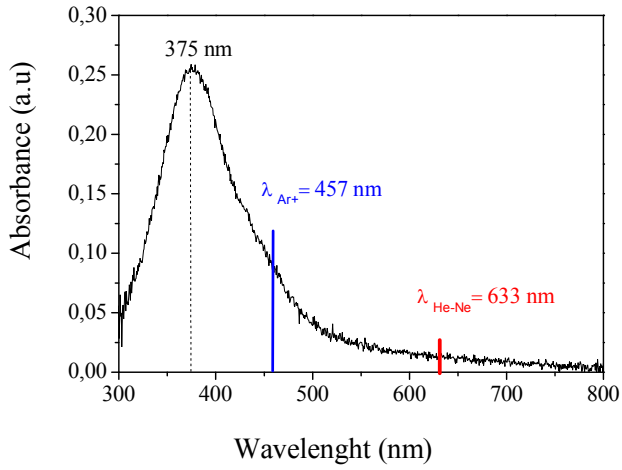

Fig. 1.9: Absorption spectrum of P4G, in which are highlighted the writing wavelength $\lambda = 457\ nm$ and the probe beam wavelength $\lambda = 632.8\ nm$.

Therefore, the azo dye molecules which have their absorption oscillators, the chromophores, parallel to the light polarization will most probably acquire the increase in energy which results in their reorientation from the initial position. This results in an excess of chromophores aligned in a direction such that the absorption oscillator is perpendicular to the polarization of the light. For P4G, the chromophores are parallel to the long molecular axis of the azo dye, that is the azo dye molecules tend to align with their long axes perpendicular to the light polarization. Hence, a thermodynamic equilibrium in the new oriented state will be established. Consequently, anisotropic dichroism or birefringence is photoinduced permanently. The azimuthal anchoring energy of the photoaligned substrate is $E > 10^{-4} J\ m^{-2}$, which is comparable with the anchoring of rubbed polyimide layer[43]. Then, the photo aligning phenomenon in case of the P4G can be explained by a model of rotational diffusion of the azo dye molecules in the field of the polarized light, whereby, in the final state, the azo dye chromophores or molecular long axes are perpendicular to the polarization direction of the light.

1.4. 3 Experiment

Here we discuss on two viable approaches to produce near ideal cycloidal OAGs,[44] both share the same photoaligning azobenzene dye and deposition procedure,[5,6] which enable to obtain high quality thin (i.e. less than 10 nm-thick) command layers, characterized by fairly high azimuthal anchoring energy (i.e. 10^{-4} J/m^2, comparable to rubbed polyimide).

In the first case, the nematic LC layer, made of low molar mass mesogens, is confined between two parallel substrates, both imposing spatially periodic planar alignment. In the second case, a reactive mesogen (RM) is coated on a single aligning substrate and then photopolymerized to permanently harden the periodic anisotropic structure.

The dye is dissolved in N-N-dimethylformamide at concentration of 1% by weight. The solution is filtered to 0.22 μm and spin coated (FR10KPA, CaLCTecS.r.l) on glass substrates at 800 rpm for 10s then at 3000 rpm for 60s. The substrates were cleaned in an ultrasonic bath of NaOH in water (5% by weight) at 40°C for 10 minutes and then in a plasma cleaner for 10 minutes to remove organic contamination, immediately before coating the dye layer. The dye films are dried at 100°C for 30 minutes, to let the solvent evaporate and to promote the adhesion of the dye molecules to the glass substrates. Figure 1.10 shows the experimental set-up used for the storage. Two circularly polarized left and right Ar^+ laser beams with wavelength $\lambda = 457\ nm$ and identical intensity $\sim 15\ mW/cm^2$ impinge on the dye coated film in the superposition region. The permanent polarization pattern of Eq.(1.1) is obtained exposing the sensitive substrate to the interference optical field for 2 minutes. In order to fulfill the stability condition for a perfect bulk replica of the director distribution imposed by the surfaces (typically $d/2\Lambda < 0.3$),[45] the spatial periodicity Λ of the optical axis pattern has been chosen equal to 8 μm, so that it is much larger than the typical thickness $d \approx 0.7 \div 3$ μm of the LC layer.

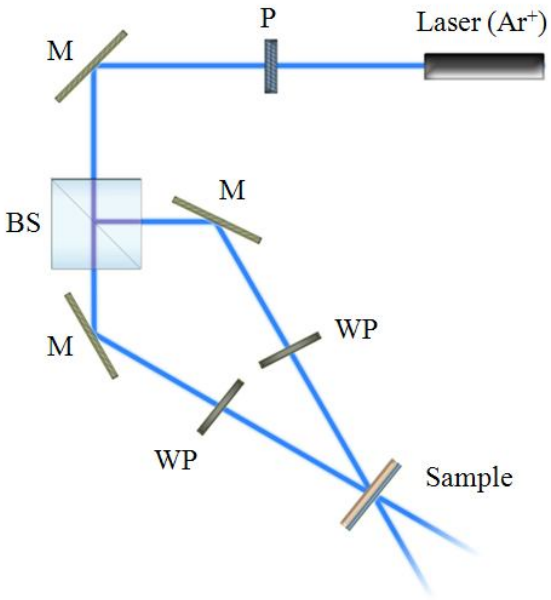

Fig. 1.10: Experimental set-up used for the holographic writing: BS beam splitter; M mirror; WP wave plate; P polarizer.

1.4.4 Fabricating of high quality cycloidal OAG

If a photosensitive photoaligning layer is exposed to the interference field of Eq.(1.1), a polarization hologram is produced via photoinduced anisotropy, whose local axis is correlated to the corresponding polarization direction. Such a patterned layer can work as a template for the adjacent nematic LC slab, by providing the necessary anchoring energy to orient the LC director parallel to the local easy axis.[46,47] Thus, the LC layer behave as a replica of the polarization hologram recorded on the photosensitive layer, in which the liquid crystal director

$\vec{n}$ is confined in the *xy*-plane and monotonously rotate in transverse direction *x*, so that a periodic structure

$$\vec{n} = \vec{n}_0(x) = [\cos(qx), \sin(qx), 0] \qquad q = 2\pi/\Lambda,$$

is realized. Here Λ is the director's modulation period. Such liquid crystal film is locally birefringent, with the optical axis lying in *xy*-plane and rotating along the *x* direction continuously, see figure 1.11(a) and 1.11(b).

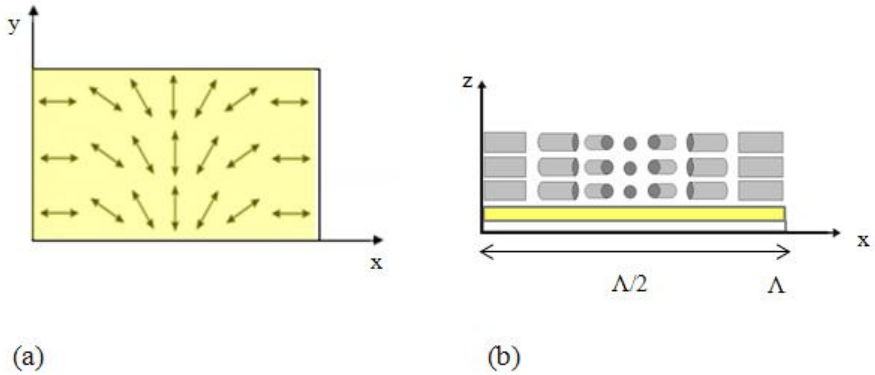

Fig. 1.11: Orientation of liquid crystal in a planar cell $0 \leq z \geq d$, in which the liquid crystal director $\vec{n}$ is confined in the (*x*, *y*)-plane and monotonously rotate in transverse direction *x*. Top view (a) and side view (b).

It is possible to obtain OAGs that exhibit 100% diffraction efficiency according to the spectral range of interest by the control of photo induced optical anisotropy $\Delta n = n_e - n_o$ of the photosensitive material and, further can be obtained for proper architecture of the liquid crystal layer: in fact, if the thickness of the cell d satisfies the half-wave plate condition,[48,49] then the light absorption and scattering is reduced and all power of incident wave is transferred in the diffracted beams and

$$d(n_e - n_o) = \left(m - \frac{1}{2}\right)\lambda \qquad (1.11)$$

with m integer and λ the wavelength.

A linear birefringence results after the deposition of a liquid crystal layer onto the alignment layer. No circular birefringence is induced ($\Delta n_{cir}= 0$). The linear birefringence originates from the difference between the ordinary and extra-ordinary refractive index of the liquid crystals and is independent of the exposure dose of the holographic recording in the photoaligning layer. The magnitude of birefringence remains constant over the exposed area and is determined by the degree of oriented liquid crystal.
Our goal is to preserve for the liquid crystal in the bulk the same rotation imposed at the surfaces. When thickness d is small, the director distribution in the bulk should follow the configuration imposed by the surfaces. For thicker cells, such distribution becomes unstable. Indeed, the increasing contribution of the elastic energy in the bulk over the aligning energy at the surfaces promotes the relaxation of the modulation imposed by the surfaces towards a homogeneous director configuration in the bulk. The onset of this instability is characterized by the value of a critical thickness, above which the structure of the pattern can not be achieved over the liquid crystal film. The choice fell on the easier phase of liquid crystals, the nematic phase which results the most photostable.

-Liquid crystal OAGs

In the first approach, two substrates are used to assemble a cell of proper thickness in a cleanroom environment (Class 100). The empty cell, with the dye-coated surfaces facing each other, is exposed to the polarization pattern in order to record two registered polarization holograms on two photosensitive aligning layers. The cell is filled by capillary action with an eutectic nematic LC mixture E7 above the clearing temperature (at 65°C) and slowly cooled to the nematic phase, down to room temperature (see figure 1.12). Close to 100% diffraction efficiency into the ±1-orders can be obtained controlling the cell thickness d and/or adjusting the effective birefringence Δn by temperature or by reorienting the nematic director with an external electric field.[50]

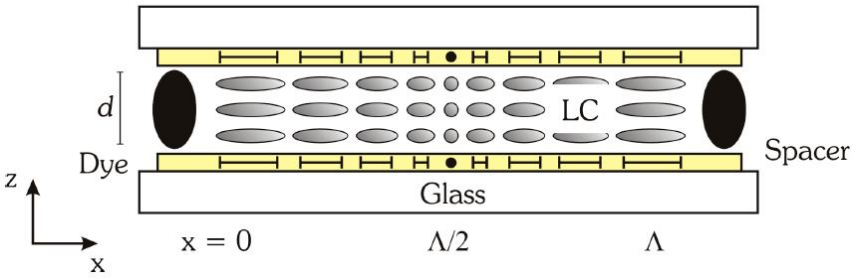

Fig. 1.12: Scheme of the LC OAG confined between two dye-coated glass substrates separated by proper spacers and assembled to form a cell of thickness d. the polarization holograms are recorded on both the photoaligning layers and then the LC is infiltrated. A single grating period is shown.

-Reactive Nematic Mesogen OAGs

In the second approach, a single photoaligning substrate is exposed to the interference field of Eq.(1.1) and, afterward, it is coated by a solution of reactive nematic mesogens (RM).[47,51-53] The RM film can be fully polymerized to achieve OAGs with enhanced optical and mechanical stability. Here we report the results obtained by using a commercial RM mixture (30% by weight) in propylene glycol monomethyl ether acetate (RMS03-001C by Merck KGaA, clearing point after coating and drying T_{NI} ~ 75°C, n_0 = 1.529 and Δn= 0.155 @ 589nm, 20°C). The RM solution is spin-coated on the previously patterned aligning substrate at 3000 rpm for 30 s. The coated substrate is baked on a hot-plate at 55°C for 60s to let the residual solvent evaporate and to favor the alignment of the uncured RM layer. The latter is then photopolymerized under nitrogen atmosphere by exposing it to the unpolarized UV light of a fluorescent lamp (λ_{MAX} = 365 nm, intensity ~ 0.1mW/cm^2) for 2 hours (see figure 1.13). All the processes, beside the polarization hologram recording, are carried out in clean-room environment (Class 100).

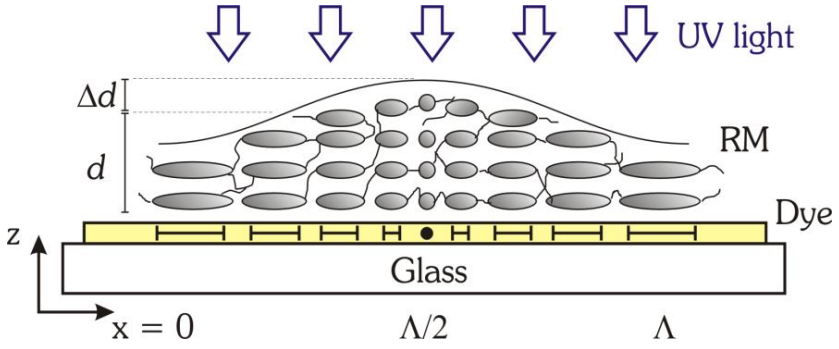

Fig. 1.13: Scheme of the RM OAG. The RM mixture is spin-coated on a single photoaligning substrate and, after thermal annealing, is polymerized via exposure to UV light under nitrogen atmosphere. A single grating period is shown.

1.4.5 Results: characterization of grating structures and diffraction.

The resulting LC OAGs show excellent optical and diffraction properties, such as low scattering, high contrast ratio and polarization selectivity. The microscope images of the LC OAG between crossed polarizers (see figure 1.14 (a)) show a neat optical modulation without defects. In figure 1.14(c) we report the diffraction patterns produced by the grating, depending on the polarization of the probe beam.

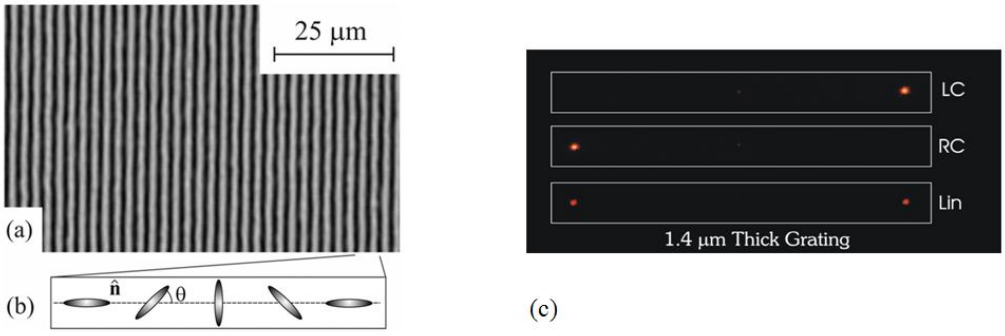

Fig. 1.14: Optical microscope image of the grating between crossed polarizers: (a) Director configuration along the grating wave vector in the liquid crystal film. (b) Nematic director orientation. (c) Diffraction patterns produced by the grating for 1.4 μm cell thick in the wedge cell. LC: left circular polarization state of the impinging beam; RC: right circular polarization state of the impinging beam; Lin linear polarization state of the impinging beam.

It is possible to see that for linear polarized impinging beam, both the first +1 and -1 order are present, with equal intensities and opposite circularly polarization states; for right (left) circular polarized impinging beam, only one order is present with intensity doubled with respect to the previous case and with left (right) circular polarization state. In all the cases, zero order is almost absent: we are in 100% diffraction efficiency condition.

A He-Ne laser beam (λ=*633 nm*) with linear and circular polarization was used as a probe beam in order to investigate the polarization state of the diffracted beams. The probe beam does not influence the recorded gratings because it is not absorbed by the azo dye. For the LC-OAG, linearly *p*-polarized light beam is uniformly diffracted into the ±1-orders (i.e., typically $|\eta_{+1} - \eta_{-1}|/(\eta_{+1} + \eta_{-1}) \approx 10^{-3}$), which exhibit almost ideal opposite circular polarizations, see figure 1.15.

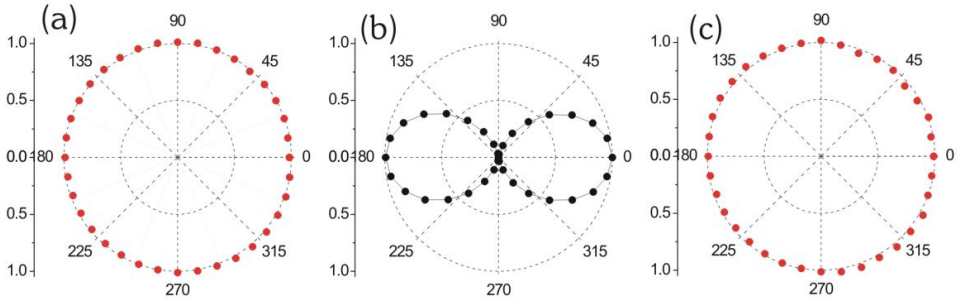

Fig. 1.15 : Polarization analysis of the three diffracted beams +1 (a), 0 (b) and -1 (c) of the LC OAG for a p-polarized probe beam. The normalized intensity of the 0- and ±1-orders are measured after a linear polarizer, versus the angle of its transmission axis.

In figure 1.15, we report the polar plots of the normalized intensity of the 0-order and the ±1-orders beams after a linear polarizer versus the angle of the polarizer axis. For both the ±1-orders the intensity after the polarizer is nearly constant (standard deviation ~0.01), indicative of excellent circular polarization. The 0-order preserves the linear polarization state of the incident beam.

Unfortunately, the LC OAGs produced according to this method still have few important weaknesses such as the inaccurate control of the grating thickness in the 1µm range and the reduced optical stability of the aligning surfaces.

Otherwise, the resulting polymeric RM OAG has an average thickness of d ~1µm and exhibits a long-range variation within 5% over a fairly large area (several cm^2). Moreover, it is easier to control the mean film thickness either by changing the concentration of solid content in the RM solution, by adjusting the rotational speed or even by stacking multiple RM layers.

In figure 1.16 are reported optical microscope image for two different magnifications (20x and 40x) of the RM OAG between crossed polarizers.

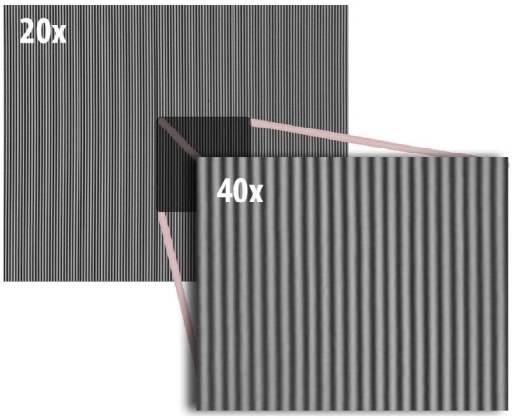

Fig. 1.16: Optical microscope image of the RM OAG between two crossed polarizers (parallel to the x- and y-axis, respectively) for two different magnifications.

On the other hand, first attempts to fabricate RM OAGs according to this approach have produced gratings with inadequate optical properties. In figure 1.17, polarization analysis of the three diffracted beams (0-order and the ±1-orders beams) of the RM OAG for a *s*-polarized probe beam are reported.

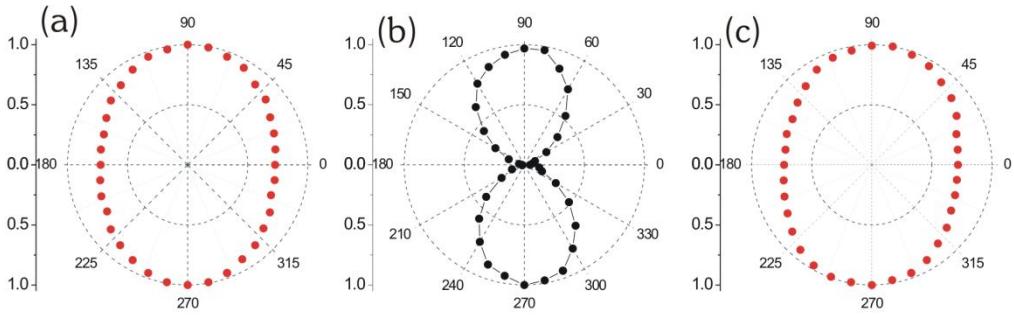

Fig. 1.17: Polarization analysis of the three diffracted beams +1 (a), 0 (b) and -1 (c) of the RM OAG for a *s*-polarized probe beam (He-Ne, λ = 633 nm). The normalized intensity of the 0- and ±1-orders are measured after a linear polarizer, versus the angle of its transmission axis. It is evident that both ±1-orders are not circularly polarized.

The normalized intensity of the ±1-orders beams after a linear polarizer (see figure 1.18) changes significantly versus the angle of the polarizer axis, signifying that the ±1-orders are not circularly polarized, as they should be in case of an ideal cycloidal OAG.

Furthermore, removing the polarizer on the diffracted beams path and using a half-wave plate to rotate the polarization plane of the linearly polarized He-Ne probe beam, the ±1-orders diffraction efficiency of RM OAG is measured versus the azimuthal angle α of the linearly polarized light (see figure 1.18(a)). In figure 1.18(b) we report the diffraction efficiency of the +1-order versus the angle α over a 2π-range. Also in this case, the data make evidence of a significant deviation from the theoretical behavior of a pure OAG, according to which the diffraction efficiency of the ±1-orders does not depend on the angle of polarization (see Eq.(1.9)).

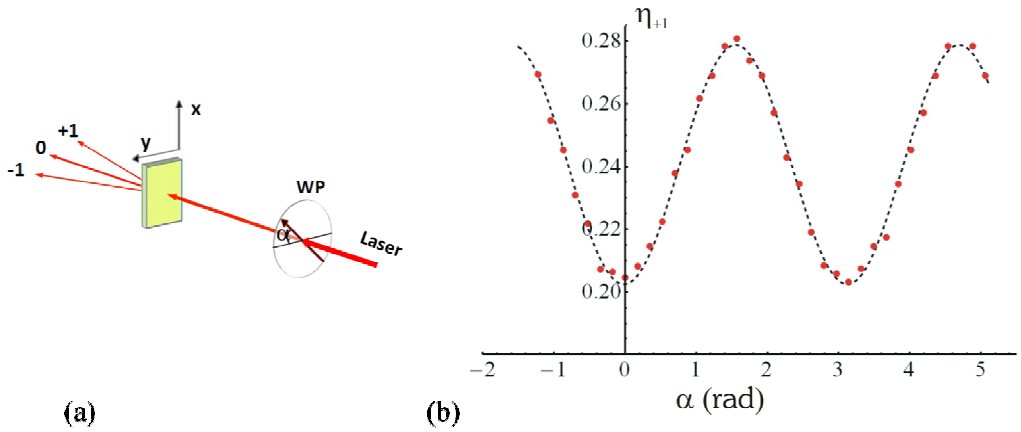

Fig 1.18: (a) Experimental geometry used for the measurement of the diffraction efficiency versus the angle α. (b) Diffraction efficiency of the RM OAG at the +1-order (red dots, ●) is measured versus the azimuthal angle α the polarization plane of the incident He-Ne beam forms with the x-axis (α = 0 and π/2 for p- and s-polarized incident beam, respectively). Dashed line is the fit of the experimental data using the function of Eq. (1.15).

With this respect, it is known that recording of polarization gratings in anisotropic media is often associated with the formation of surface relief gratings (SRG), which may significantly

affect the diffraction properties of the former ones.[54-57] While the occurrence of SRGs is hindered in the first approach, since the OAGs are confined between two solid substrates, they are possible in this second approach at the air-RM interface. Indeed, investigation of the RM film topography via atomic force microscopy (AFM) shows an undulation of the free surface characterized by the same periodicity of the OAG and a peak-to-valley depth of ~50nm (see figure 1.19).

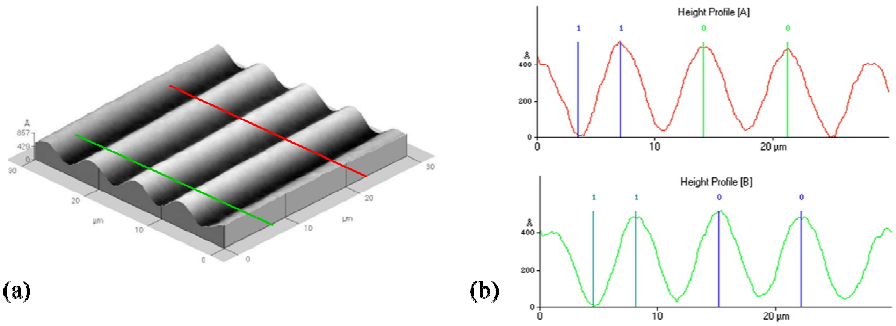

Fig. 1.19: Topography of the RM OAG measured by AFM shows periodic relieves with a peak-to-valley depth ~50nm and the same spatial periodicity of the optical axis grating (~8µm).

A simple theoretical model based on Jones calculus is considered here to verify if the sole periodic modulation of the surface topography is enough to explain the diffraction properties of the RM grating. The model takes into account both the OAG and the SRG, which is regarded as a sinusoidal correction to the polymer film thickness

$$d + \Delta d \cos(qx + \delta_0) \qquad (1.12)$$

Where Δd is the modulation amplitude (half of the relief depth) and δ_0 the spatial phase shift of the SRG with respect to the OAG $n(x)=[\cos(\pi x/\Lambda), \sin(\pi x/\Lambda), 0]$. The Jones transmission matrix of the SRG of Eq.(1.12) is[54]

$$J^{SRG} = \begin{pmatrix} e^{i\Delta\psi cos\,(qx+\delta_0)} & 0 \\ 0 & e^{i\Delta\psi cos\,(qx+\delta_0)} \end{pmatrix} \tag{1.13}$$

where $\Delta\psi = 2\pi\,\Delta d(n_p - n_a)/\lambda$ is half of the phase shift due to the surface relief, $n_p$and n_a are the refractive index of the polymer (i.e., average value between n_0 and $n_e = n_0 + \Delta n$) and of the adjacent medium (i.e., $n_a \approx 1$ for air), respectively. The diffracted fields can be evaluated multiplying the incident linearly polarized field by the total transmission matrix

$$E_{out} = J^{SRG} J^{OAG} E_{in} \begin{pmatrix} \cos\alpha \\ \sin\alpha \end{pmatrix} \tag{1.14}$$

The total transmission matrix J^{TOT} can be written as the matrix product of $J^{SRG} J^{OAG}$

$$J^{TOT} = \begin{pmatrix} e^{i\Delta\psi\cos(qx+\delta_0)} & 0 \\ 0 & e^{i\Delta\psi\cos(qx+\delta_0)} \end{pmatrix} \times$$

$$\begin{pmatrix} \cos(\Delta\phi) + isin(\Delta\phi)\cos qx & i\sin(\Delta\phi)\sin qx \\ i\sin(\Delta\phi)\sin qx & \cos(\Delta\phi) - isin(\Delta\phi)\cos qx \end{pmatrix} =$$

$$= \begin{pmatrix} A & B \\ C & D \end{pmatrix}$$

where

$$A = e^{i\Delta\psi\cos(qx+\delta_0)}[\cos\Delta\phi + i\sin\Delta\phi\cos qx]$$

$$B = -ie^{i\Delta\psi\cos(qx+\delta_0)}[\sin\Delta\phi\cos qx]$$

$$C = -ie^{i\Delta\psi\cos(qx+\delta_0)}[\sin\Delta\phi\cos qx]$$

$$D = e^{i\Delta\psi\cos(qx+\delta_0)}[\cos\Delta\phi - i\sin\Delta\phi\cos qx]$$

Using the following expansion

$$e^{i\Delta\psi\cos(qx+\delta_0)} = J_0(\Delta\psi) + 2\sum_{n=1}^{\infty}(-1)^n[-iJ_{2n-1}(\Delta\psi)\cos\{(2n-1)(qx+\delta_0)\} + J_{2n}(\Delta\psi)cos\{2n(qx+\delta_0)\}] = \sum_{n=-\infty}^{\infty} i^n J_n(\Delta\psi)e^{in\,(qx+\delta_0)}$$

$$= J_0(\Delta\psi) + \sum_{n=1}^{\infty} i^n J_n(\Delta\psi)(e^{in(qx+\delta_0)} + e^{-in(qx+\delta_0)})$$

we can write the expression for A,B,C and D

$$A = \left[J_0(\Delta\psi) + \sum_{n=1}^{\infty} i^n J_n(\Delta\psi)(e^{in(qx+\delta_0)} + e^{-in(qx+\delta_0)})\right] \times \left[\cos(\Delta\phi) + isin\,(\Delta\phi)\frac{(e^{iqx} + e^{-iqx})}{2}\right]$$

$$B = -i\left[J_0(\Delta\psi) + \sum_{n=1}^{\infty} i^n J_n(\Delta\psi)(e^{in(qx+\delta_0)} + e^{-in(qx+\delta_0)})\right] \times sin\,(\Delta\phi)\frac{(e^{iqx} + e^{-iqx})}{2i}$$

$$C = -i\left[J_0(\Delta\psi) + \sum_{n=1}^{\infty} i^n J_n(\Delta\psi)(e^{in(qx+\delta_0)} + e^{-in(qx+\delta_0)})\right] \times sin\,(\Delta\phi)\frac{(e^{iqx} + e^{-iqx})}{2i}$$

$$D = \left[J_0(\Delta\psi) + \sum_{n=1}^{\infty} i^n J_n(\Delta\psi)(e^{in(qx+\delta_0)} + e^{-in(qx+\delta_0)})\right] \times \left[\cos(\Delta\phi) - isin\,(\Delta\phi)\frac{(e^{iqx} + e^{-iqx})}{2}\right]$$

In the above expression, J_n are Bessel functions of first kind and the subscript denotes the order of the Bessel function. If we pick out the term which only involve the +1st order diffracted beam, we get the following matrix

$$J_{TOT}^{+1} = \begin{bmatrix} A^{+1} & B^{+1} \\ C^{+1} & D^{+1} \end{bmatrix}$$

$$A^{+1} = \frac{i}{2}\left[J_0(\Delta\psi)\sin(\Delta\phi) + 2J_1(\Delta\psi)\cos(\Delta\phi)e^{i\delta_0} - J_2(\Delta\psi)\sin(\Delta\phi)e^{i2\delta_0}\right]$$

$$B^{+1} = -\frac{1}{2}\sin(\Delta\phi)\left[J_0(\Delta\psi)\sin(\Delta\phi) + J_2(\Delta\psi)\sin(\Delta\phi)e^{i2\delta_0}\right]$$

$$C^{+1} = -\frac{1}{2}\sin(\Delta\phi)\left[J_0(\Delta\psi)\sin(\Delta\phi) + J_2(\Delta\psi)\sin(\Delta\phi)e^{i2\delta_0}\right]$$

$$D^{+1} = \frac{i}{2}\left[-J_0(\Delta\psi)\sin(\Delta\phi) + 2J_1(\Delta\psi)\cos(\Delta\phi)e^{i\delta_0} + J_2(\Delta\psi)\sin(\Delta\phi)e^{i2\delta_0}\right]$$

Using these expression we can write for the total field diffracted for the +1st order

$$\begin{bmatrix} E_{TOT,x}^{+1} \\ E_{TOT,y}^{+1} \end{bmatrix} = \begin{bmatrix} A^{+1} & B^{+1} \\ C^{+1} & D^{+1} \end{bmatrix} \begin{bmatrix} E_{IN,x} \\ E_{IN,y} \end{bmatrix}$$

In this way we obtain the intensity of the +1st order of diffraction and the polarization state of the output beam. Adopting the approximation $J_0 \approx 1$, $J_1 \approx \Delta\psi/2$ e $J_2 \approx 0$ and considering a generic linear polarization in input [cosα sinα] we can obtain the following electric field vector in output:

$$\begin{bmatrix} E_{TOT,x}^{+1} \\ E_{TOT,y}^{+1} \end{bmatrix} = \begin{bmatrix} -\frac{1}{2} sin\alpha\ sin\Delta\phi + \frac{i}{2}\cos\alpha(2e^{i\alpha}\Delta\psi\cos\Delta\phi + sin\Delta\phi) \\ \frac{i}{2}\sin\alpha(e^{i\alpha}\Delta\psi\cos\Delta\phi + sin\Delta\phi) - \frac{1}{2}\cos\alpha\sin\Delta\phi \end{bmatrix}$$

where $E_{TOT,x}^{+1}$ and $E_{TOT,y}^{+1}$ are the horizontally and the vertically component, respectively, of the diffracted beam.

If we know the electric field components the beam intensity can be derived as

$$I_{TOT} = \left|E_{TOT,x}{}^{+1}\right|^2 + \left|E_{TOT,y}{}^{+1}\right|^2$$

The total efficiency $\eta_{\pm1}(\alpha)$, defined as the ratio of the 1st order intensity on the total incident intensity, can be expressed according to the previous relation:

$$\eta_{\pm1}(\alpha) = \frac{1}{8}[2 + \Delta\psi^2 + (\Delta\psi^2 - 2)\cos(2\Delta\phi) + 2\Delta\psi\sin(2\Delta\phi)\cos(\delta_0 + 2\alpha)] \qquad (1.15)$$

We can fit the data reported in figure 1.18(b) considering the above function for the values of the parameters

$$\Delta\psi \approx 0.77$$

$$\Delta\phi \approx 0.15$$

$$\delta_0 \approx \pi$$

The value of spatial phase shift means that the peaks of the SRG correspond to the regions in which the optical axis is oriented orthogonally to the grating vector (i.e. n(x)=[0,1,0] along the fringes, see figure 1.13). Assuming $\Delta n = 0.155$, $n_p = 1.6$ and $n_a = 1$we can calculate the average film thickness d and the relief modulation amplitude Δd.

We can look at two situations: with a horizontally or a vertically linearly polarized beam.

For horizontally polarized input light $\begin{bmatrix}1\\0\end{bmatrix}$ we get:

$$\begin{bmatrix}E_{HH}{}^{+1}\\E_{HV}{}^{+1}\end{bmatrix} = J_{TOT}{}^{+1}\begin{bmatrix}1\\0\end{bmatrix} = \frac{1}{2}\begin{bmatrix}i\{J_0(\Delta\psi)\sin\Delta\phi + 2J_1(\Delta\psi)\cos\Delta\phi e^{i\delta_0} - J_2(\Delta\psi)\sin\Delta\phi e^{i\delta_0}\}\\-\sin\Delta\phi\{J_0(\Delta\psi) + J_2(\Delta\psi)e^{i\delta_0}\}\end{bmatrix}$$

For vertically polarized input light $\begin{bmatrix}0\\1\end{bmatrix}$ we get:

$$\begin{bmatrix}E_{VH}{}^{+1}\\E_{VV}{}^{+1}\end{bmatrix} = J_{TOT}{}^{+1}\begin{bmatrix}0\\1\end{bmatrix} = \frac{1}{2}\begin{bmatrix}-\sin\Delta\phi\{J_0(\Delta\psi) + J_2(\Delta\psi)e^{i\delta_0}\}\\i\{-J_0(\Delta\psi)\sin\Delta\phi + 2J_1(\Delta\psi)\cos\Delta\phi e^{i\delta_0} + J_2(\Delta\psi)\sin\Delta\phi e^{i\delta_0}\}\end{bmatrix}$$

Where $E_{HH}{}^{+1}$ is the horizontal component of the diffracted light with horizontal input polarization, $E_{HV}{}^{+1}$ is the vertical component of the diffracted light with vertical input polarization, $E_{VH}{}^{+1}$ and $E_{VV}{}^{+1}$ are the same for vertical input polarization.
The intensities detected for the 1st order are

$$I_{HH} = |E_{HH}|^2, \quad I_{HV} = |E_{HV}|^2, \quad I_{VV} = |E_{VV}|^2, \quad I_{VH} = |E_{VH}|^2,$$

From symmetry considerations we should expect that $\delta_0 \in \left\{0, \frac{\pi}{2}, \pi, \frac{3\pi}{2}\right\}$. In all measurements we found that $I_{VV} \neq I_{HH}$, in particular $I_{VV} < I_{HH}$ that means $\delta_0 = \pi$. As we have found $\delta_0 = \pi$ we can write the total expression for the detected intensities in the +1st order as:

$$I_{HH}{}^{+1} = \frac{1}{4}[J_0(\Delta\psi)\sin\Delta\phi + 2J_1(\Delta\psi)\cos\Delta\phi - J_2(\Delta\psi)\sin\Delta\phi]^2$$

$$I_{HV}{}^{+1} = \frac{1}{4}sin^2\Delta\phi[J_0(\Delta\psi) + J_2(\Delta\psi)]^2$$

$$I_{VH}{}^{+1} = \frac{1}{4}sin^2\Delta\phi[J_0(\Delta\psi) + J_2(\Delta\psi)]^2$$

$$I_{VV}{}^{+1} = \frac{1}{4}[-J_0(\Delta\psi)\sin\Delta\phi + 2J_1(\Delta\psi)\cos\Delta\phi + J_2(\Delta\psi)\sin\Delta\phi]^2$$

From the measured intensities ${I_{HH}}^{+1}$, ${I_{HV}}^{+1}$, ${I_{VH}}^{+1}$and ${I_{VV}}^{+1}$ we can calculate $\Delta\phi$ and $\Delta\psi$:

$$|\Delta\phi| \cong sin^{-1}\left(2\sqrt{I_{HV}}\right) = sin^{-1}\left(2\sqrt{I_{VH}}\right)$$

As $\Delta\phi$ is known we can derive the equation for $\Delta\psi$

$$\sqrt{I_{VV}} - \sqrt{I_{HH}} = 2J_1(\Delta\psi)\cos\Delta\phi$$
$$\sqrt{I_{VV}} - \sqrt{I_{HV}} = J_1(\Delta\psi)\cos\Delta\phi + J_2(\Delta\psi)\sin\Delta\phi \approx J_1(\Delta\psi)\cos\Delta\phi$$
$$\sqrt{I_{HV}} - \sqrt{I_{HH}} = J_1(\Delta\psi)\cos\Delta\phi - J_2(\Delta\psi)\sin\Delta\phi \approx J_1(\Delta\psi)\cos\Delta\phi$$
$$\Delta\psi \approx 2J_1(\Delta\psi) = \frac{\sqrt{I_{VV}}-\sqrt{I_{HH}}}{\cos\Delta\phi} \approx \frac{\sqrt{I_{VV}}-\sqrt{I_{VH}}}{\cos\Delta\phi} \approx \frac{\sqrt{I_{HV}}-\sqrt{I_{HH}}}{\cos\Delta\phi}$$

We calculate the average film thickness $d \approx 1\,\mu m$ (from $\Delta\phi = (\pi\,\Delta n d)/\lambda$) and the relief modulation amplitude $\Delta d = 25\,nm$ (from $\Delta\psi = 2\pi\,\Delta d(n_p - n_a)/\lambda$) (i.e. peak-to-valley relief depth ≈ 50 nm), which are both in excellent agreement with the AFM measurements. These results confirm the adequacy of the simple theoretical model discussed here to interpret the optical diffraction properties of the RM OAG, and suggest that the discrepancy versus the ideal cycloidal OAG is merely due to the superimposed SRG. With this respect, we are exploring few strategies to overcome the disadvantage of the SRG for the optical properties of the grating by managing the air-RM interface, both with surfactants, aimed at enforcing in-plane orientation of the nematic director at the free RM surface, and with an overlaid planarizing coating made of photoreactive isotropic monomers, aimed at transferring a planar topography on the underlying RM grating. An ongoing work in our laboratory is based on the use of the nematic RM infiltrated between two aligning solid substrates and then photo-polymerized, in order to guarantee the mechanical and optical stability of the polymeric OAG and simultaneously avoid the formation of the SRG, thus taking advantage of both the described approaches.

1.5 Experimental Part II: Spatial light modulator-assisted polarization holography

In the first experimental part we have seen how the vectorial nature of light can be used to obtain peculiar polarization light patterns and the coupling of this holographic technique with polarization-sensitive materials has enabled optical devices with special performance.
More recently, spatial light modulator (SLM)-assisted polarization holography made it possible to create complex light field configurations, like two-dimensional (2D) polarization patterns achieved by the interference of two pairs of beams with perpendicular planes of incidence and orthogonal polarizations (i.e. linear or circular), for the creation of reconfigurable 2D periodic microstructures with peculiar diffraction properties.[58]
Our idea was to extend this SLM-assisted approach to generate highly efficient microlens array (MAs) in which the size, the shape, and the focal length of each microlens can be controlled independently of the other.[59] In particular, the interference optical field is also obtained with two waves with orthogonally circular polarization and equal intensity (as described in section 1.4), but one of the two beam contains the phase of each microlens. The phase information of the MAs is directly stored in thin azodye layers. Exploting the photoinduced linear birefringence, various combinations of MAs including spherical and cylindrical microlens have been created by controlling the gradient refractive index of each microlens.

A "microlens array" is an array of microlenses and means any microstructure which is capable of focusing light. The micro/nano optic element array has been applied in many new optical devices due to its small volume, light weight, flexible design.[60-64] This kind of array can offer a lot of new functions which cannot be realized by the traditional optical device. Depending on the application, one may require a microlens of accurate profile with controlled focusing properties or, in the case of an array, high quality over most lenses in the array. Thus, several methods to fabricate MAs has been developed. Current fabrication methods for the microscale

lens have several shortcomings, in that the preparation process is relatively complex due to multiple steps, and there is a lack of controllability over the shape and array formation of lens. A variety of strategies have been adopted for fabricating microlens structures. In general, they can be broadly classified into three categories:

- imprinting methods;[65,66]
- surface-tension-driven techniques consisting of melt-reflow[67-69]and ink-jet printing;[70]
- lithographic, photolithography[71,72] or interference lithography.[73,74]

While these approaches demonstrate the ability to produce microlens arrays with uniform surface profiles, the techniques are either high-cost or require long fabrication times. Our approach offers several advantages over previous methodologies of microlens fabrication, including:

- the ability to create microlens arrays rapidly;
- ease of tuning the dimensions of the microlenses;
- versatility in the process that allows the formation of microlens arrays.
- the ability to create any desired configuration of MAs with different focal length.

1.5.1 Microlens Array holograms

Microlens array in thin film can be achieved take into account the interference of a plane wave $\vec{E}_P$ and a properly tailored phase wave $\vec{E}_L$, having opposite circular polarization, whose propagation axes form a small angle θ:

$$\vec{E}_{TOT} = \vec{E}_P + \vec{E}_L = \frac{1}{\sqrt{2}}\begin{pmatrix}1\\ i\end{pmatrix} e^{i\delta} + \frac{1}{\sqrt{2}}\begin{pmatrix}1\\ i\end{pmatrix} e^{i\psi(x,y)} e^{i\delta} \qquad (1.16)$$

where $\delta = \frac{\pi}{\Lambda}x$, with $\Lambda = \frac{\lambda_R}{2\sin(\theta/2)}$ representing the spatial period of the polarization pattern, λ_R

is the recording wavelength and

$$\psi(x,y) = \sum_{n=1}^{N}\sum_{m=1}^{N}\psi_{nm}(x,y)$$

is the phase of the N x M microlens array. The phase of each microlens in $\psi(x,y)$ can be written as follows $\psi_{nm} = \pi(a_{nm}(x-x_{nm})^2 + b_{nm}(y-y_{nm})^2)/(\lambda_R f_{nm})$, where $a_{nm}b_{nm}$ are constant values in the range (0,1), (x_{nm}, y_{nm}), f_{nm} are the center coordinates and focal distance of each microlens, respectively.

The resulting pattern in the superposition region is given by

$$\vec{E}_{TOT} = \frac{1}{\sqrt{2}}\begin{pmatrix} e^{i\delta} + e^{i\psi_{x,y}}e^{-i\delta} \\ ie^{i\delta} - ie^{i\psi_{x,y}}e^{-i\delta} \end{pmatrix}$$

If we expose a photo-birefringent material with this polarization interference pattern, a polarization hologram will result.

The matrix of the recorded hologram is written considering the Stokes parameters[75]

$$S = \begin{pmatrix} S_0 \\ S_1 \\ S_2 \\ S_3 \end{pmatrix} = \begin{pmatrix} 1 \\ 2\cos(2\delta-\psi) \\ 2\sin(2\delta-\psi) \\ 0 \end{pmatrix}$$

$$L = e^{i\gamma_s kdS_0}\begin{pmatrix} \cos M + ikd\gamma_{lin}S_1\dfrac{\sin M}{M} & ikd\gamma_{lin}S_2\dfrac{\sin M}{M} \\ ikd\gamma_{lin}S_2\dfrac{\sin M}{M} & \cos M - ikd\gamma_{lin}S_1\dfrac{\sin M}{M} \end{pmatrix} \quad (1.17)$$

where

$M = kd\sqrt{\gamma^2{}_{lin}({S_1}^2 + {S_2}^2)}$, k is the wave number, d is the thickness of the film, $\gamma_{lin}$is a coefficient related to the photoinduced linear birefringence and γ_s is a coefficient related with the scalar photoresponse of the material.

After replacing the Stokes parameters in the matrix, the latter can be written as a sum of three matrices that determine the existence of three waves after the hologram, associated with the zero non diffracted wave and the ±1st order wave:

$L = L_0 + L_{+1} + L_{-1}$

$$L_0 = \begin{pmatrix} 1 & 0 \\ 0 & 1 \end{pmatrix} \cos(2kd\gamma_{lin}) \tag{1.18}$$

is for the directly transmitted wave (0th order).

$$L_{+1} = \frac{1}{2}\begin{pmatrix} i & -1 \\ -1 & -i \end{pmatrix} \sin(2kd\gamma_{lin})e^{i\psi} \tag{1.19}$$

determines a wave with right circular polarization in the +1 order, and

$$L_{-1} = \frac{1}{2}\begin{pmatrix} i & -1 \\ -1 & -i \end{pmatrix} \sin(2kd\gamma_{lin})e^{-i\psi} \tag{1.20}$$

determines a wave with a left circular polarization in the -1 order.

As reported in the work,[59] and recalling that $\vec{E}_{out} = L\vec{E}_{in}$ if a linear polarized plane wave

$\vec{E}_{in_l} = \begin{pmatrix} 1 \\ 0 \end{pmatrix}$

impinges on the MA the expected diffracted fields has the components

$$\vec{E}^{out}{}_{+1} = \frac{i}{2}\sin(2kd\gamma_{lin})\, e^{-i\psi}\begin{pmatrix}1\\ i\end{pmatrix}$$

$$\vec{E}^{out}{}_{-1} = \frac{i}{2}\sin(2kd\gamma_{lin})\, e^{i\psi}\begin{pmatrix}1\\ -i\end{pmatrix} \tag{1.21}$$

From the equation ($\vec{E}^{out}_{+1}$) can be noted that the +1 -order appears the conjugated phase of the recording MA, it means that microlens with negative focal length present a divergent behavior, while the -1-order has a convergent behavior.

Considering a normally incident plane wave with left circular polarization

$$\vec{E}_{in_{LCP}} = \frac{1}{\sqrt{2}}\begin{pmatrix}1\\ -i\end{pmatrix}$$

the only diffracted wave in this case is a right circularly polarized, +1 order wave

$$\vec{E}^{out}{}_{+1} = \sqrt{2}i\Theta\sin(2kd\gamma_{lin})\, e^{-i\psi}\begin{pmatrix}1\\ -i\end{pmatrix} \tag{1.22}$$

On the other hand, if the incident beam is a right circularly polarized beam

$$\vec{E}_{in_{RCP}} = \frac{1}{\sqrt{2}}\begin{pmatrix}1\\ i\end{pmatrix}$$

The diffracted wave is left circularly polarized, -1 order wave

$$\vec{E}^{out}{}_{-1} = \sqrt{2}i\Theta\sin(2kd\gamma_{lin})\, e^{i\psi}\begin{pmatrix}1\\ i\end{pmatrix} \tag{1.23}$$

where Θ is a function taking the values 1 (or 0) for the diffracted +1 order and 0 (or 1) for the diffracted -1 order when the incident beam is left –handed (right-handed) circularly polarized.

Thus, when a circularly polarized beam impinges on the polarization hologram only one diffracted order appears, and by managing the polarization helicity, we can obtain diverse microlens array distributions.

It is worth noting that, in the equations of the diffracted beams, the focalization of the ± 1 orders is off axis and that the +1 order has a conjugated phase with respect to the -1 order and $\vec{E}_L$. For example, the microlens hologram recorded with the diverging $\vec{E}_L$ field produces a convergent (divergent) field in the +1(-1) order.

1.5.2 Writing the MA and results

Photosensitive aligning layers of the P4G azodye on indium tin oxide (ITO) coated glass substrate have been obtained as described in section 1.4.3. After spin coating, the substrates were heated to remove the solvent from the alignment layers. The empty cells were prepared by sandwiching these two substrates with the alignment layers facing each other and then exposed to the interference pattern. The figure 1.20 shows the experimental setup employed to record the MAs. The optical system under study consisted in two identical lenses, sharing a common focal point where was placed the aperture stop. This is commonly called a 4f system in which the distance between the object and the image will be four times the common focal length.

An expanded Argon laser beam ($\lambda_R = 488\, nm$) insides over a spatial light modulator (SLM) which displays a synthetic phase hologram SPH[76] to generate a plane wave and the phase element corresponding to the microlenses array. The lens L_1 realize the Fourier transform of the SPH on its focal plane. In order to transmit only the two orders corresponding to the interfering fields, the SPH pass thought a spatial filter (SF) that blocks several noise order, e.g. the zero order. To obtain orthogonal linear polarizations a half wave plate (HWP) rotates 90° the linear polarization of one of the two generated waves.

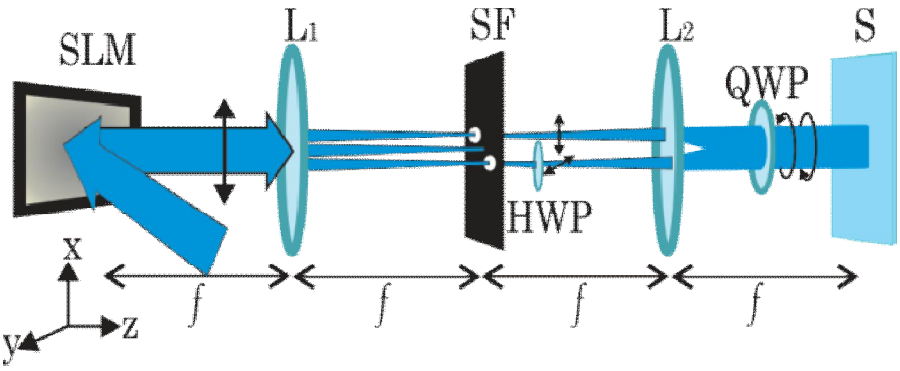

Fig. 1.20: Experimental setup to record the Mas hologram: SLM spatial light modulator, L1 and L2 lenses, SF spatial filter, HWP half-wave plate, QWP quarter-wave plate, S sample.

The lens L_2 collects and projects an image of the two interfering fields, which generate the PH, on the sample (S). The orthogonal linear polarizations are transformed to circular opposed polarizations by means of a quarter wave plate (QWP).

The total recording intensity and the exposure time were 50mW/cm^2 and 3 minutes, respectively. Several phase configurations have been designed in order to realize MAs including spherical, cylindrical and mixed microlenses with different focal length. When the liquid crystalline material was infiltrated into the empty cells by capillary action in isotropic phase, and slowly cooled down in the nematic phase at room temperature, the MAs appeared. Because the top and the bottom surfaces are simultaneously registered during the exposure, the planar periodic alignment propagates unperturbed through the depth of the cell to create a uniform alignment through the bulk of the cell.

In order to visualize the behavior and the diffraction efficiency of the MA holograms a circularly polarized He-Ne laser probe beam (λ_p = 633 nm) has been used. The experimental 4f setup used to reads out the recorded MA are shown in figure 1.21.

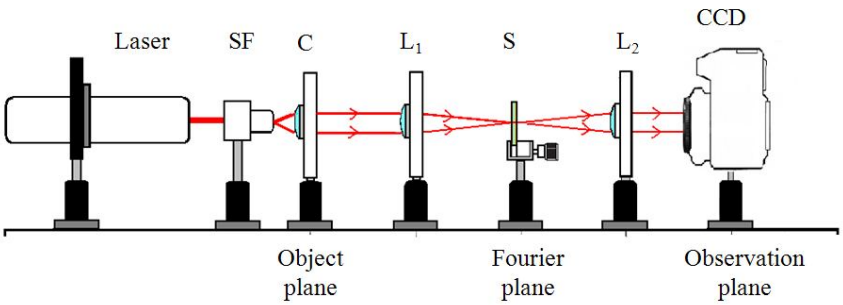

Fig. 1.21: Experimental 4f setup for characterizing the optical properties of MAs: He-Ne laser, SF spatial filter, C collimating lens, L_1 and L_2 lenses, S sample and CCD camera.

The focal length was an important parameter to characterize the property of the microlens array, the effective focal length of each recorded MA is defined as follows

$$f_{nm}^{P} = \frac{\lambda_R}{\lambda_P} f_{nm} = 0.77\, f_{nm}$$

and depends of the recording (λ_R) and probe (λ_P) wavelengths, while the total diffraction efficiency is defined as

$$\eta_{+1} + \eta_{-1} = sin^{\,2}\beta$$

We start to describe the 5x5 MA, that is composed by 25 spherical microlenses ($a_{nm} = b_{nm} = 1$), each one has a diameter of $D \approx 1.28$ mm and focal length 2.5 cm. The figure 1.22 shows the phase distribution that corresponds to the 5x5 MA, which focalizes 2.5 cm behind of the PH.

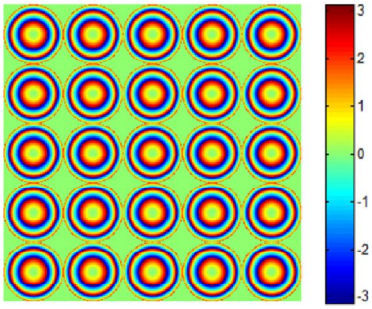

Fig. 1.22: 5x5 MA, phase distribution of the MA, which is composed by 25 spherical microlenses.

The focused array intensity is shown in figure 1.23(a) and (b). The evaluated diffraction efficiency is η = 50%, while with an applied voltage, V_a= 1.2 *Volt* the diffraction efficiency increases to η = 75%.

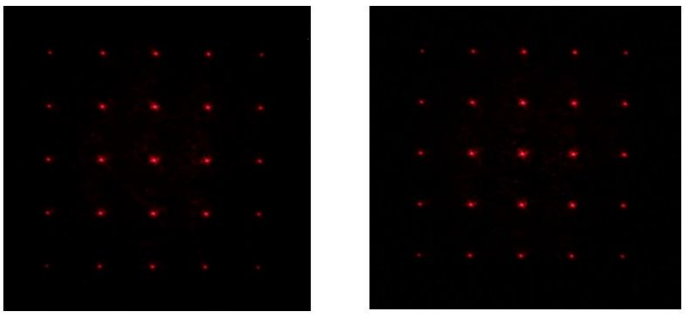

Fig. 1.23: Recorded intensity 2.5 cm behind the PH, where the 25 spherical microlenses are focused, (a) without and (b) with applied voltage (V_a= 1.2 *Volt*).

A second mixed 4 x 4 MA, where each microlens has a diameter *D*~1.6 mm, composed by 12 spherical microlenses ($a_{1j} = b_{1j} = a_{4j} = b_{4j} = a_{21} = b_{21} = a_{24} = b_{24} = a_{31} = b_{34} = 1$ with j = 1, 2, 3, 4) with focal length f_{sph} = 5cm, two horizontal cylindrical microlenses ($a_{22} = a_{33} = 1$, $b_{22} = b_{33} = 0$), all the cylindrical microlenses with focal length f_{cyl} = 10cm, is shown in figure 1.24. This

shows the phase distribution of the 4 x 4 mixed MA, which is composed by 12 spherical microlenses, two horizontal cylindrical microlenses and two vertical cylindrical microlenses.

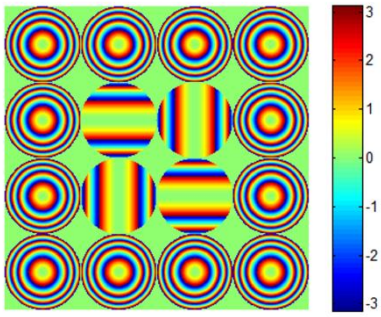

Fig. 1.24: 4x4 mixed MA, phase distribution of the MA.

The intensity recorded either 5 cm or 10 cm behind the PH, where the spherical or cylindrical microlenses are focused, is shown in figure 1.25 and 1.26, respectively.

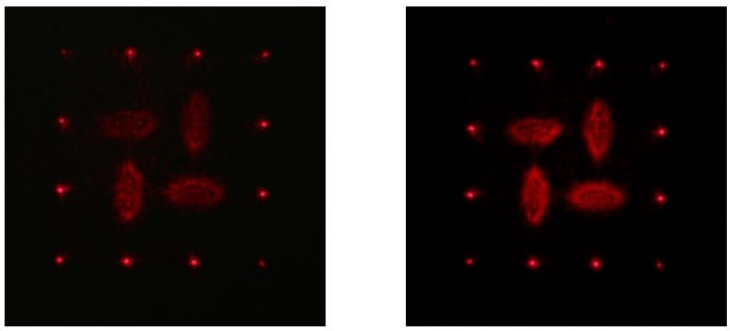

Fig. 1.25: Recorded intensity 5 cm behind of the PH, where the 12 spherical microlenses are focused, (a) without and (b) with applied voltage ($V_a = 2\ Volt$).

The evaluated diffraction efficiency is $\eta = 60\%$, while with an applied voltage, $V_a = 2\,Volt$ the diffraction efficiency increases to $\eta = 75\%$.

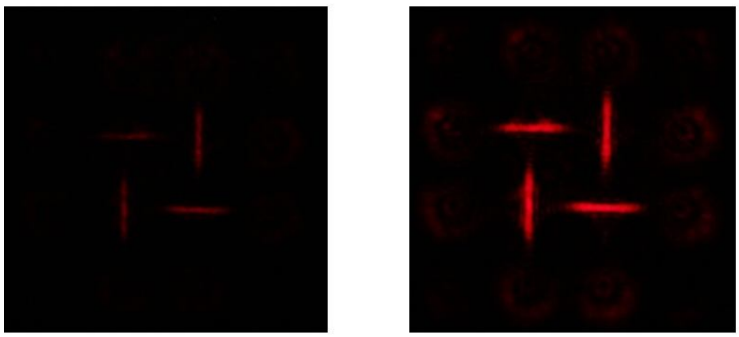

(a) (b)

Fig. 1.26: Recorded intensity 10 cm behind of the PH, where the cylindrical microlenses are focused, (a) without and (b) with applied voltage.

The evaluated diffraction efficiency is $\eta = 20\%$, while with an applied voltage, $V_a = 2\,Volt$ the diffraction efficiency increases to $\eta = 80\%$.

In order to visualize the behavior and the diffraction efficiency of the MA holograms, which is in accordance of Eqs. (1.21) we used a linear and a circularly polarized He-Ne laser probe beam ($\lambda_p = 633\,nm$). The figure 1.27 shows the recorded diffracted orders, 20 cm behind of a MA hologram, by a CCD camera. As can be seen at this distance the orders do not overlap, however these are defocused because the MA codified has a focal length of 5 cm. The diffracted orders when the incident beam is linearly or circularly polarized with and without applied voltage, $V_a = 2\,Volt$, to the sample are reported in figure 1.27(a)-(b) and 1.27(c)-(d), respectively.

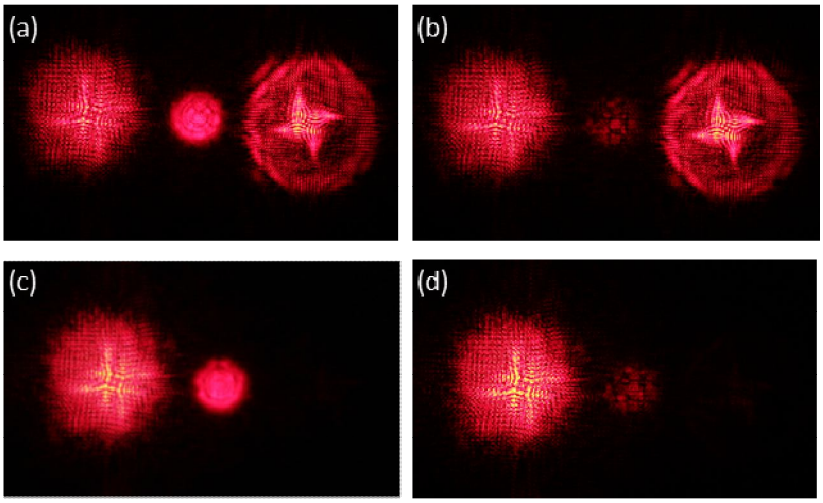

Fig. 1.27: Intensity of the diffraction orders for a PH that codifies a 4x4 mixed MA, which has focal lengths f = 5, 10 cm, these patterns were recorded 20 cm behind of the PH by a CCD. Diffraction produced by the PH when the impinging beam is linearly polarized without (a) and with (b) an applied voltage V_a = 2 V. Diffraction produced by the PH when the impinging beam is circularly polarized without (c) and with (d) an applied voltage V_a = 2 V.

The last MA reported has three spherical microlenses, three horizontal cylindrical microlenses and three vertical microlenses; the diameter is $D\sim 800\mu m$. Here in the same MA we have three different effective focal length f^{p}_{jm} = 15, 10 and 5 cm, where $j=1\text{-}3$ represents the array column index. The phase distribution of 3x3 mixed MA is reported in figure 1.28, which is composed by 9 microlenses: 3 spherical, 3 horizontal cylindrical and 3 vertical cylindrical.

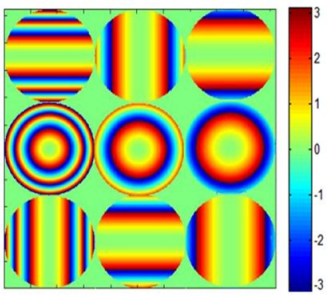

Fig. 1.28: 3x3 mixed MA, phase distribution.

Therefore, when the probe beam is focused by the microlenses in the left column ($f^p{}_{1m} = 5\ cm$) is out of focus in the central and right columns (figure 1.29).

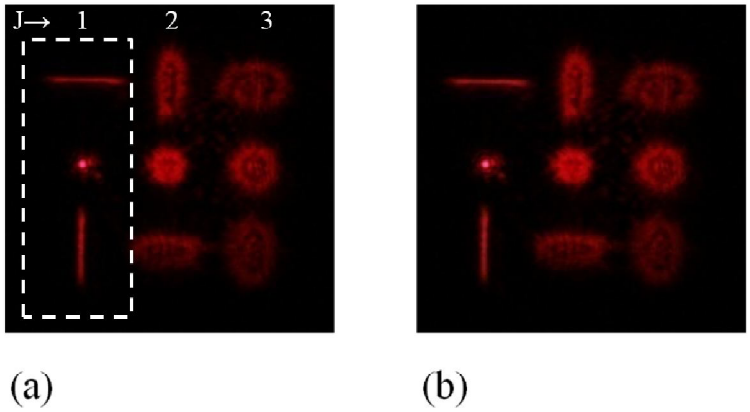

Fig. 1.29: Recorded intensity 5 cm behind of the PH, where the left column are focused, (a) without and (b) with an applied voltage.

When the probe beam is focused by the microlenses in the central column ($f^p{}_{2m} = 10\ cm$), the right and the left columns are out of focus.

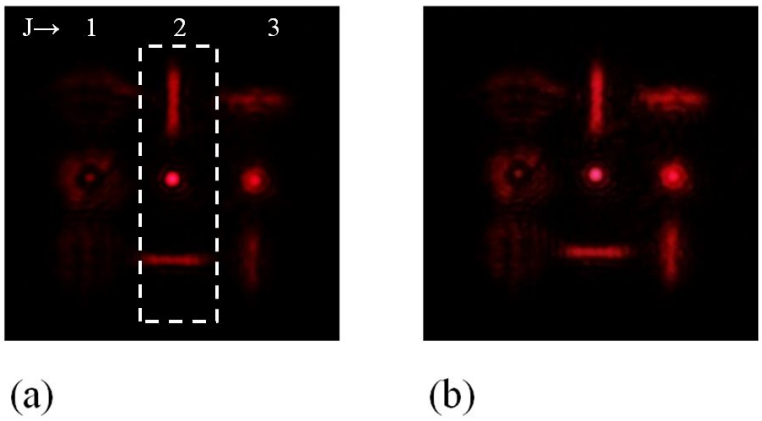

Fig. 1.30: Recorded intensity 10 cm behind of the PH, where the central column are focused, (a) without and (b) with an applied voltage

In both diffraction produced by the polarization hologram without applied voltage is $\eta = 60\%$ figures 1.29(a), 1.30(a) and with an applied voltage $V_a = 1.7\,Volt$ is $\eta = 75\%$ figures 1.29(b) 1.30(b).

In all the reported MAs the total diffracted efficiency do not reach the 100%, this is attributable to the fact that the microlenses are defined on a circular pupil, then there are dark regions between the microlenses where the PH cannot reorient the molecules of the azo-dye and accordingly to the LC. Therefore, the liquid crystal molecules are not organized, which produces light dispersion and a weak background noise. In addition, particularly for high-density coupling, diffusion, or screen applications, it is often important that the microlenses utilize the entire surface for focusing. In this way, essentially all incident light can be controlled by the array. When the entire useful surface area is employed for focusing, the array is said to possess a 100% diffraction efficiency.

On the contrary, using a highly birefringent material, such as a nematic liquid crystal, is possible to increase the diffraction efficiency of the devices simply applying a low voltage.

1.6 Spectro-polarimetric applications of OAGs

The stability of the recorded gratings and the high induced birefringence of the material, open up the possibility of interesting applications of the gratings to different optical devices. Current technologies use several optical and electro-optical elements, different absorbing polarizers, dispersive elements (prims or gratings), phase modulator, which make them very inefficient because of its intrinsic limitations in real-time and artifact-free measurements. Here we shall show how the unique polarization properties of cycloidal OAG can be used in the field of polarimetry, in particular, an CD spectrograph and a new type of photopolarimeter based on two different kinds of diffraction gratins has been realized.

1.6.1 Circular Dichroism spectrograph

Circular dichroism (CD) spectroscopy is a special technique that provides unique information on chiral molecular structures[77,78] by measuring their differential absorption with respect on the left and right circular polarization states of light. Conventional CD spectrometers take advantage of polarization modulation techniques and require several optical elements before and after the sample to be investigated. The complexity of the optical scheme and of the polarization-modulation detection method intrinsically increases the sources of instrumental artifacts. The polarization sensitive diffraction of cycloidal OAGs suggested an original approach for real-time CD spectroscopy[44] that radically reduces the sources of instrumental artifacts. In figure 1.31 is reported a simplified scheme of the diffractive CD spectrograph.

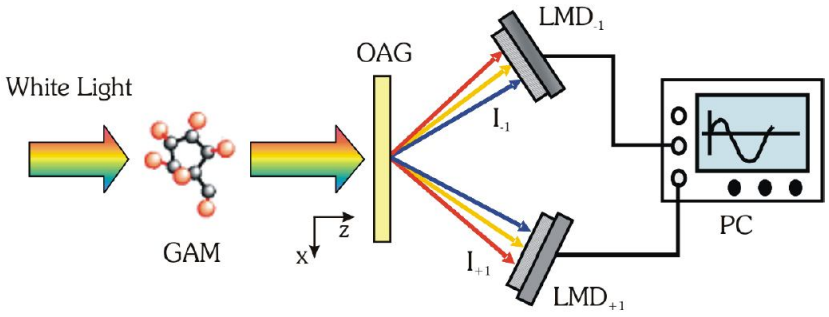

Fig 1.31: Scheme illustrating the operation principle of the method for diffractive CD spectroscopy. White unpolarized light is collimated on the sample (i.e. a general anisotropic medium, GAM) and its transmission portion is directed to the OAG. The intensities of ±1-orders are measured at each wavelength via linear multi-channel detectors (LMD). The data from the two LMDs are acquired and the CD spectra of the sample calculated.

An unpolarized white light is collimated and directed to the sample without further polarization adjustments or bandwidth, and the transmitted light is directed on the cycloidal OAG. The polarization grating diffracts the light into the zero-order (0) and the two first-order (±1) beams, whose intensities are simultaneously detected by two linear multi-channel detectors

(LMD) to evaluate the CD spectrum of the sample. We have to consider a general anisotropic medium (GAM), which exhibits all the possible anisotropies simultaneously: linear birefringence (LB) and dichroism (LD), circular birefringence (CB) and dichroism (CB).
The true CD spectrum of the sample can be estimated from the half-logarithm of the ratio of the intensities of the $\pm 1^{st}$ orders:

$$CD \cong \frac{1}{2}\log\left(\frac{I_{+1}}{I_{-1}}\right) - \frac{CBLBLD}{6} \tag{1.24}$$

where $CBLBLD/6$ is the correction term.
This proposed method does not require any complex and frequent calibration procedure related to the diffraction efficiency and the spectral response of the actual OAG because the Eq. (1.24) do not contain any reference to the optical parameters, thickness d, birefringence Δn and period Λ of the grating. The only precondition is that the diffraction efficiency of the OAG does not vanish at any wavelength in the spectral range of CD interest, otherwise the measurement of at that wavelength would be precluded (i.e., $I_{+1} = I_{-1} = 0$).

1.6.2 Two-grating photopolarimeter

Here we reported the realization of a photopolarimeter based on two different kinds of diffraction gratings able to measure simultaneously and in real-time the Stokes parameters of a electromagnetic wave, in order to evaluate its polarization state.[79] In general, a photopolarimeter is based on the acquisition of four signals, obtained with appropriate separation of the investigated beam, in which Stokes parameter S_i are calculated from the measured values I_j of these four intensities, according to the relation $S_i = A_{ij}I_j$, where A_{ij} is the matrix describing the device.

Several instruments have been developed that allow to perform real-time measurements of the Stokes parameters.[80-85] Nevertheless, the devices proposed have some limitations and drawbacks. Some of them are difficult to align and often need a complex calibration procedure.[80,81] In our case, basic elements of the proposed photopolarimeter are two diffraction gratings, through which it is possible to separate the investigated beam in the required four beams (see figure 1.32). For this reason we called our device Two Gratings Photopolarimeter (TGP). In particular, one of the two gratings, is the cycloidal OAG described before, obtained by means of a polarization holographic recording, on a photosensitive azo-compound, while, the other is an ordinary transmission grating obtained by means of an intensity holographic technique, based on the interference of two waves with parallel polarization states, on a thin layer of acrylate monomeric mixture.

Is possible to calculate the Stokes parameters of a light beam using only the polarization grating, measuring first the intensities of the $\pm 1^{st}$ orders diffracted beams I_1 and I_2 and successively the intensity of the transmitted beam, I_0 and $I_{45°}$, after the passage through a linear polarizer. For a real time measurement, we have to put the ordinary transmission grating in succession to the polarization grating. In this way, the zero order diffracted beam of the polarization grating is diffracted by the ordinary transmission grating in two first orders diffracted beams which presents the same polarization state of the impinging beam.

The functioning principle can be summarized as follows: the light beam to be measured (I) impinges onto the OAG polarization grating, and the 1^{st} diffracted orders $I_1$and I_2 ($I_{\pm 1}$) are detected by the photodiodes Ph_1 and Ph_2, respectively. The transmitted beam (zero order) is diffracted by the ordinary transmission grating in which the first orders I_3 and I_4 ($I_{45°}$ and I_0 respectively) are collected, after passing through polarizers $P_{45°}$ and $P_{0°}$, by the photodiodes Ph_3 and Ph_4. The four output signals are sent to an analog-to-digital circuit board of a computer that controls the experiment.

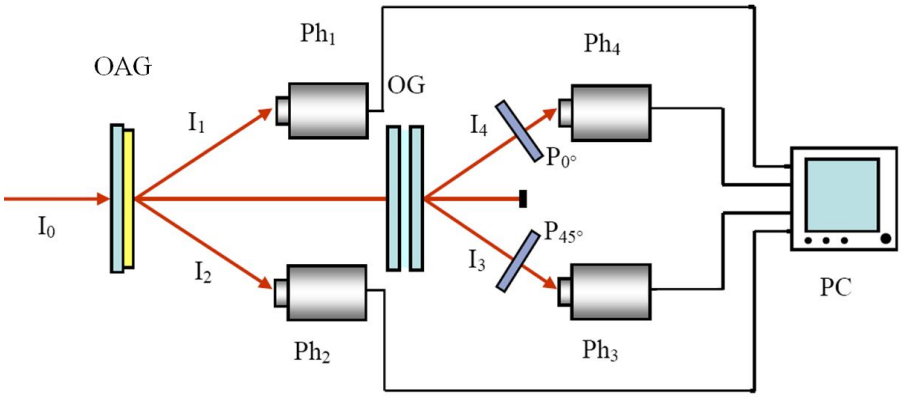

Fig. 1.32: Optical scheme of two gratings photopolarimeter. I incident beam, I_1-I_4 diffracted beams, OAG polarization grating, OG ordinary transmission grating, P0° and P45° polarizers, Ph_1-Ph_4 photodiodes, PC computer and acquisition system.

It is possible to establish a relation between the four signal registered by photodiodes and the Stokes parameters; in particular the Stokes S_0, S_1, S_2 and S_3 parameters are expressed in terms of some coefficients K_0, K_1, K_2 and K_3 that depend on the diffraction efficiency of the grating, the polarizer absorption and the photodiode sensitivities.[79] For a particular wavelength, the relationships between the four signals and the Stokes parameters are reported in [79] and the K_i coefficients are found for each wavelength by a preliminary measurements of the signals/intensities I_i and are given by the ratio of the measured intensity:

$$K_1 = \frac{I_0}{2I_1}, \qquad K_2 = \frac{I_0}{2I_2}, \qquad K_3 = \frac{I_0}{2I_3}, \qquad K_4 = \frac{I_0}{2I_4} \tag{1.25}$$

Compared with other devices employed in polarimetric measurements, TGP present several advantages, as for example: the compactness of the structure, that do not require any modulating optics or moving parts; a very short measurement time, related only to the speed of

the detectors and electronics; a great facility to align the device; absence of complex calibration procedures. In addition, because the instrument is based on diffraction gratings, it allows operation with white light source to provide spectral information. Optical alignment of the photopolarimeter is fast and very easy, and the calibration procedure is performed with a single measurement of a linearly polarized beam, of known intensity and wavelength. The easiness of the calibration procedure is related to the fact that, the polarization grating is able to recognize the polarization state of the investigated light.

1.7 Conclusions

In conclusion, taking advantage of polarization holography and of the interactions at the interface between a patterned substrate and a thin film of liquid crystal, we obtained highly efficient gratings. The diffractive devices present low scattering and high diffraction efficiency. We have seen that, for proper values of cell thickness and spatial periodicity of the grating, the director configuration in the nematic bulk is a perfect replica of the polarization gratings recorded on the aligning layer. In this way, the gratings present all the diffraction peculiarities of pure polarization holograms, and, exploiting the electro-optical manipulation of liquid crystal based devices, can be completely controlled in the diffracted energy distribution by means of an external voltage.

In particular, two fabrication strategies aimed to achieve cycloidal OAGs with optimal performances have been described and their advantage and downsides discussed. In particular, polarization holography, based on the interference of two orthogonal circular polarized beams, and photo-anisotropic aligning material have been exploited to produce cycloidal OAG in birefringent nematic layers. The latter perform as replicas of the faint polarization hologram recorded in the thin photosensitive aligning film. The cases of low molar mass nematic LC sandwiched in a planar cell and of photo-reactive mesogenic monomers spincasted on top of the aligning substrate have been studied experimentally and the results interpreted with a simple model. The LC gratings confined between substrates have demonstrated excellent

optical quality, resembling ideal cycloidal OAG. The RM gratings are less prone to optical degradation, thus exhibiting higher optical and mechanical stability, but are affected by detrimental periodic undulation of the free surface. Feasible perspectives to fabricate effective cycloidal OAGs characterized by near-ideal diffraction features, high efficiency, least optical scattering, and still being optical and mechanical robust have been anticipated.
All these features make it a very interesting device for various applications. In fact, the polarization grating has been selected as the basic element for a photopolarimeter able to measure simultaneously and in real time the Stokes parameters of an electromagnetic wave, in order to determine its polarization state and a CD spectrograph. The microdevices proposed in this work are very compact because free of modulating or moving parts, are easy to calibrate and can operate over the whole visible spectral range.

We have presented an all-optical technique to create MAs based on the SLM-assisted polarization holography. This method allows us design the GRIN of a plane liquid crystal cell in order to create different MA configurations. Two remarkable advantages respect to other techniques are short time and low intensity recording. The controllable linear birefringence and the transparency of the liquid crystal allow maximize the diffraction efficiency near to 100% in a wide range of wavelengths, through a low voltage applied to the LC cell. We have shown two MA configurations characterized by spherical and cylindrical microlenses with different focal lengths, which are in good agreement with the focalization properties of these types of elements. We have shown two MA configurations characterized by both spherical and cylindrical microlenses with different positive or negative focal lengths

References:

1. C. Provenzano, P. Pagliusi and G. Cipparrone, *Appl. Phys. Lett.* 89, 121105 (2006).
2. L.M. Blinov, G. Cipparrone, A. Mazzulla, C. Provenzano, et al, *Appl. Phys. Lett.* 87, 061105-1-061105-3 (2005).
3. L.M. Blinov, G. Cipparrone, A. Mazzulla, C. Provenzano, et al., *Molecular Crystal and Liquid Crystal* 449, 147-160 (2006).
4. M. L.Blinov, R. Barberi, G. Cipparrone, et al *Liquid Crystals* 26, 427-436 (1999).
5. V. Chigrinov, E. Prudnikova, V. Kozenkov, H. Kwok, H. Akiyama, T. Kawara, H. Takada, and H. Takatsu, *Liquid Crystals* 29, 1321-1327 (2002).
6. O. Yaroshchuk, J. Ho, V. Chigrinov, H. S. Kwok, *Jap. J. Appl. Phys.* 46, 2995-2998 (2007).
7. L. Nikolova and P. S. Ramanujam, *Polarization Holography* (Cambridge University, 2009).
8. D. Gabor. *Nature* 161, 777–778 (1948).
9. H.J. Eichler, P. Gunter, D.W. Phol, *Laser Induced Dynamic Gratings*, (Springer-Verlag, Berlin, 1986).
10. T. Huang, K.H. Wagner, *J.Opt. Soc. Am B*. 13, 282-299 (1996).
11. Sh. D. Kakichashvili. *Opt. Spectrosc*. 33, 324–327 (1972).
12. Sh. D. Kakichashvili. *Kvant. Elektr*. 1, 1435–1441 (1974).
13. Sh. D. Kakichashvili. *Polyarizatsionnaya golografiya. Leningrad: Nauka* (1989).
14. H. J. Eichler, P. Gu¨nter, and D. W. Pohl, Springer-Verlag Berlin, 13 21 (1985).
15. N. K. Viswanathan, S. Balasubramanian, L. Li, S. K. Tripathy, and J. Kumar. *Jap. J. Appl. Phys.* 38, 5928–5937 (1999).
16. F. Weigert. U¨ *Verh. Deutsch. Phys. Ges*. 21, 479–483 (1919).
17. F. Weigert, *Verh. Phys. Ges*. 21, 485 (1919).
18. F. Weigert, *Z. Phys*. 5, 410 (1921).
19. Z. Sekkat and W. Knoll, Adv. Photochem. 22, 117-195 (1997).
20. S. Xie, A. Natansohn, and P. Rochon, Chem. Mater. 5, 403 (1993).

21. H. Rau, In Photochemistry and Photophysics; J. K. Rabek, Ed; CRC Press: Boca Raton, FL, 2, 119 (1990).

22. K. Anderle, R. Birenheide, M. Eich, and J:H: Wendorff. *Makromol. Chem. Rapid Commun*., 10, 477 (1989).

23. S.P. Palto and G. Durand. *J. Phis. II France* 5, 963 (1995).

24. H. J. Eichler, P. Gunter, D.W. Pohl. *Springer-Verlag* (1986).

25. S. P. Palto, S. G. Yudin, C. Germain, G. Durand, *J. Phys. II France*, 5, 133-145 (1995).

26. G. Friedel, Annu. *Physique*, 18, 273 (1922).

27. I.C. Khoo. *Liquid Crystals Physical Properties and Nonlinear Optical Phenomena*. Wiley-Interscience, NY, 10 (1995).

28. P.J. Collings andM.Hird. *Introduction to liquid crystals: Chemistry and Physics*. Taylor and Francis, 6, 111 (1997).

29. S. R. Nersisyan, N. V. Tabiryan, L. Hoke, D. M. Steeves and B. Kimball, *Opt. Express* 17(3), 1817–1830 (2009).

30. W. M. Gibbons and S.-T. Sun, *Appl. Phys. Lett.* 65, 2542–2544 (1994).

31. J. Chen, P. J. Bos, H. Vithana and D. L. Johnson, *Appl. Phys. Lett.* 67, 2588–2590 (1995).

32. C. M. Titus and P. J. Bos, *Appl. Phys. Lett.* 71, 2239–2241 (1997).

33. T.Huang, K.H. Wagner, *J. Opt. Soc. Am. B*. 13, 282-299 (1996).

34. L. Nikolova, M. Ivanov, T. Todorov, and S. Stoyanov, *Bulg. J. Phys.* 20, 46-54 (1993).

35. R. M. A. Azzam and N. M. Bashara. *Ellipsometry and polarized light*. Elsevier.

36. G. Cipparrone, A. Mazzulla, S. P. Palto, S. G.Yudin, L. M. Blinov, *Appl. Phys. Lett.* 77, 2106-2108 (2000).

37. F. Gori, *Optics Letters* 24, 584-586 (1999).

38. G. Cipparrone, A. Mazzulla, M.L. Blinov, *J. Opt. Soc. Am. B*. 19, 1157-1161 (2002).

39. C. Provenzano, P. Pagliusi. and G. Cipparrone, *Appl. Phys. Lett.* 89, 121105 (2006).

40. L.M. Blinov, G. Cipparrone, A. Mazzulla, C. Provenzano, et al, *Appl. Phys. Lett.* 87, 061105-1-061105-3 (2005).

41. L.M. Blinov, G. Cipparrone, A. Mazzulla, C. Provenzano, et al, *Molecular Crystal and Liquid Crystal* 449, 147-160 (2006).

42. V. Chigrinov, A. Muravski, H. S. Kwok, et al *Phys. Rev. E*, 68, 061702 and references (2003).

43. V. Chigrinov, E. Prudnikova, V. Kozenkov, et al *Liquid Crystals* 29, 1321–1327 (2002).

44. P. Pagliusi, E. Lepera, C. Provenzano, A. Mazzulla and G. Cipparrone *Proc. SPIE*, 8069: 806910-14 (2011).

45. H. Sarkissian, N. Tabirian, B. Park, and B. Zeldovich, *Mol. Cryst. Liq. Cryst.* 451, 1-19 (2006).

46. J. Eakin, Y. Xie, R. Pelcovits, M. D. Radcliffe, and G. P. Crawford, 85, 1671-1673 (2004).

47. G. P. Crawford, J. Eakin, M. D.Radcliffe, A. Callan-Jones and R. J. Pelcovits, *Appl. Phys.* 98, 123102 (2005).

48. C. Provenzano, P. Pagliusi. and G. Cipparrone, *Appl. Phys. Lett*. 89, 121105 (2006).

49. H. Sarkissian, N. Tabirian, B. Park, B. Zeldovich, *Molecular Crystal and Liquid Crystal* 451, 1-19 (2006).

50. C. Provenzano, P. Pagliusi, and G. Cipparrone, *Appl. Phys. Lett*. 89, 121105 (2006).

51. S. R. Nersisyan, N. V. Tabiryan, D. M. Steeves, and B. R. Kimbal, *J. Nonlinear. Opt. Phys. Mater.* 18, 1-47 (2009).

52. M. J. Escuti, C. Oh, C. Sànchez, C. W. M. Bastiaansen, and D. J. Broer, *Proc. SPIE* 6302: 630207 (2006).

53. S. R. Nersisyan, N. V. Tabiryan, D. M. Steeses, B. R. Kimball, V. G. Chigrinov and H. S. Kwok *Appl. Opt*. 49, 1720-1727 (2010).

54. N. C. R. Holme, L. Nikolova, P. S. Ramanujam, and S. Hvilsted, *Appl. Phys. Lett.* 70, 1518-1520 (1997).

55. I. Naydenova, L.Nikolova, T.Todorov, N. C. R Holme, P. S. Ramanujam and S. Hvilsted, *J. Opt. Soc. Am. B*. 55, 1627-1631 *(1997).*

56. F. Lagugné Labarthet, T. Buffeteau and C. Sourisseau, *J. Phys. Chem. B* 102, 2654-2662 (1998).

57. F. Lagugné Labarthet, T. Buffeteau and C. Sourisseau, *J. Phys. Chem. B.* 103, 6690-6699 (1999).

58. U. Ruiz, C. Provenzano, P. Pagliusi and G. Cipparrone, *Opt. Lett.* 37, 311-3 (2012).

59. U. Ruiz, C. Provenzano, P. Pagliusi and G. Cipparrone, *Opt. Lett*. 37, 4958- 4960 (2012).

60. M. Ares, S. Royo, and J. Caum, *Opt. Lett*. 32, 769 (2007).

61. S. Dong-Hak, L. Byoungho, and K. Eun-Soo, *ETRI J.* 28, 521 (2006).

62. P. J. W. Hands, S. M. Morris, T. D. Wilkinson, and H. J.Coles, *Opt. Lett.* 33, 515-517 (2008).

63. W. Pan, L. Liu, H. Liu, and S. Deng, Chin. *Opt. Lett*. 4, 265 (2006).

64. P. Fei, Z. He, C. Zheng, T. Chen, Y. Men, and Y. Huang, Lab Chip 11, 2835-2841 (2011).

65. H. Yabu, M. Shimomura, *Langmuir* 21, 1709-1711 (2005).

66. M. V. Kunnavakkam, F. M. Houlihan, M. Schlax, J. A. Liddle, P. Kolodner, O. Nalamasu, J. A. Rogers, *Appl. Phys. Lett. 82*, 1152-1154 (2003).

67. Z. L. Liau, D. E. Mull, C. L. Dennis, R. C. Williamson, R. G. Waarts, *Appl. Phys. Lett. 64*, 1484-1486 (1994).

68. H. A. Biebuyck, G. M. Whitesides, *Langmuir 10*, 2790-2793 (1994).

69. M.-H. Wu, C. Park, G. M. Whitesides, *Langmuir 18*, 9312-9318 (2002).

70. E. Bonaccurso, H.-J. Butt, B. Hankeln, B. Niesenhaus, K. Graf, *Appl. Phys. Lett. 86*, 124101 (2005).

71. T. J. Suleski, D. C. O'Shea, *Appl. Opt.* 34, 7507-7517 (1995).

72. Q. Yang, Y. Guo, S. Liu, *Opt. Lett. 27*, 1720-1722 (2002).

73. S. Yang, G. Chen, M. Megens, C. Ullal, Y.-J. Han, R. Rapaport, E. L. Thomas, J. Aizenberg, *Adv. Mater.* 17, 435-438 (2005).

74. R. Yang, W.J. Wang, S. A. Soper, *Appl. Phys. Lett.*, *86*, 161110 (2005).

75. T. Nose and S. Sato, *Liq. Cryst.* 2, 1425-1433 (1989).

76. V. Arrizón, D. Sánchez-de-la-Llave, G. Méndez, and U. Ruiz, *Opt. Express* 19, 10553-10562 (2011).

77. N. Berova, K. Nakanishi, and R. W. Woody, Eds., Wiley-WCH, NY (2000).

78. A. Roger and B. Nordén, Oxford University Press, Oxford (1997).

79. C. Provenzano, G. Cipparrone, A. Mazzulla, *Appl. Opt.* 45, 3929-3934 (2006).

80. R. M. A. Azzam, E. Masetti, I. M. Elminyawi and F. G. Grosz., *Rev Sci. Instrum* 59, 84 (1988).

81. R. M. A. Azzam, A. M. El-Saba, M.A.G. Abushagur, *Thin Solid Films* 53, 313-314 (1998).

82. E. Masetti and A. Krasilnikova, *Thin Solid Films* 455-56, 138-142 (2004).

83. T. Todorov and L. Nikolova, *Opt. Lett.* 17, 358-359 (1992).

84. L. Nikolova, M. Ivanov, T. Todorov, and S. Stoyanov, *Bulg. J. Phys.* 20, 46-54 (1993).

85. R. M. A. Azzam and N. M. Bashara. *Ellipsometry and polarized light*. Elsevier.

Advanced Materials based on chiro-optical supramolecular architectures

2.1 Introduction

Chiral optical materials are often based on macromolecules, not only due to typical advantages of polymeric materials (e.g., processability, robustness and durability), but also due to the amplification of chirality. Chirality that is induced, controlled, monitored is a modern interdisciplinary field of research not only for fundamental science but also for a number of practical applications in such areas as catalysis,[1] nonlinear optics,[2] polymer and materials science,[3,4] molecular and chiral recognition,[5] molecular devices.[6-8] In particular, in the beginning of the nineties, it became clear that chirality can play an important role in the field of optical applications. Furthermore, it was realized that due to their lack of mirror symmetry, chiral materials could be excellent candidates for the design of optical devices.[9] Chirality may also play an important role in the field of nanotechnology and more specifically for the design of artificial nanostructures with properties usually not found in nature. Currently, several research groups of all over the world are involved with supramolecular chirality. It is clear that chiral optical materials are of interest in a wide variety of scientific disciplines. For an area of research that has been around for almost 200 years, it is surprising that chiral optical materials still continue to fascinate researchers and will continue to play a prominent role in the field of optics and materials. Especially the design of new complex and multifunctional chiral materials will stimulate new researches and will definitely lead to the development of new optical techniques and applications.

This is the framework of this second topic, that is addressed towards the development of a materials science approach to build up polymeric matrices with controllable supramolecular chiral structures and subnanometric cavities able to host molecules. The latter are based on chiral supramolecular architectures induced by a co-crystallization process between a temporary non-racemic guest and an achiral polymer host represented by syndiotactic polystyrene (s-PS).[10-14] The s-PS is a robust thermoplastic polymer which can be processed by standard industrial processes (like melt extrusion) and is produced in large quantities, several 5000 tons per year (Idemitsu). The induction and amplification of chirality in the syndiotactic polystyrene (s-PS) involves the formation of a δ phase[15-17] composed by non-racemic helical crystallites based on a racemic unit. Moreover, it is possible to replace the non-racemic guest

contained in the crystalline cavities of s-PS with achiral chromophores of suitable size and shape,[18,19] which confirmes the supramolecular nature of the induced chiral response of s-PS. In this chapter, the chiral response of the chiro-optical film was investigated by *circular dicroism* (CD) analysis but, to better discriminate between the chiral optical response of the polymer host and of the low-molecular-mass guests, *vibrational circular dichroism (VCD)* studies are also reported, with quantitative evaluations of the *anisotropy factor* (dissymmetry ratio, G) for relevant host and guest peaks. Finally, the low cost, commercial availability, robustness and easy melt processing of the polymer are expected to facilitate design and production of chiral optical materials and devices, based on co-crystalline phases of s-PS with achiral or racemic chromophores. In particular, possible applications of these films are in the field of fluorescent materials, optical memories (based on the cocrystallization of photoreactive guest molecules), non-linear optical materials (with polar guests) and chiro-optical memories (based on temporary co-crystals with chiral guest molecules).

2.2 Guest-Host strategy

Polymeric materials with optoelectronic, chiro-optic and photonic properties are usually simply based on the dispersion of chromophores in an amorphous polymer matrix although in order to reduce the diffusivity, the chemical bonding to the polymer backbone (grafting), or the inclusion of the chromophores in the polymer chain as monomers (polymerization) are frequently used. The polymerization technique has been often limited by the difficulties in synthesizing and polymerizing highly functionalized monomers while the grafting technique is often limited by the poor stability towards oxygen or water of the reactive polymeric substrates as well as by the need of several synthetic steps generally leading to low chromophore concentrations. In recent years dendrimers have been used to reduce diffusivity of dye molecules in the solid state and to prevent their self-aggregation. In fact, it has been shown that encapsulating individual chromophores can greatly enhance their optical properties. The

encapsulation of individual chromophores has been also studied in solutions, by using as host molecules not only dendrimers but also large cyclic compounds, like cyclodextrins, yclophanes and crown ethers containing many supramolecular optical sensing complexes.[20,21] A more simple alternative method to reduce the diffusivity of chromophore molecules in the solid state and to prevent their self-aggregation consists in the formation of co-crystals with suitable polymer hosts. Particularly efficient and versatile appears to be the inclusion of chromophore molecules as guest of the host nanoporous crystalline phases (the so called δ [22,23] and ε [24,25] phases) of syndiotactic polystyrene (sPS).

2.2.1 Syndiotactic polystyrene (s-PS)

Syndiotactic polystyrene (s-PS) is a promising semi-crystalline engineering plastic and is composed on a long chain hydrocarbon wherein alternating carbon centers are attached to phenyl groups (figure 2.1). Since the production of s-PS in 1985, there has been a tremendous amount of research focused on the synthesis and characterization of this stereoregular polymer.[26-33] This thermoplastic material potentially has important applications and for this reason many efforts have been done to characterize this polymer. Thus, the drive for the investigation of the behavior and properties of s-PS is due to the high melting temperature (≈ 270 ° C), solvent resistance, good electrical and mechanical properties,[34,35] the ability to crystallize from the melt very quickly.

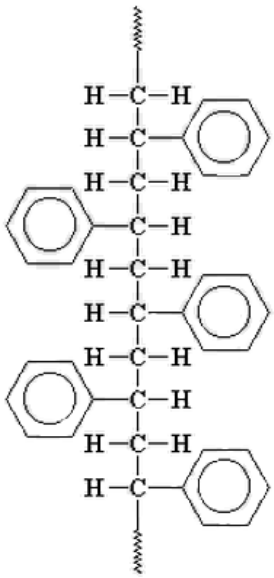

Fig. 2.1 Molecular structure of syndiotactic polystyrene, showing side chains arranged in a symmetrical regularly alternating pattern on either side of the polymer backbone.

Its relatively low cost combined to such properties has motivated the commercialization of this material by Dow Chemical Co. (QuestraTM) and Idemistsu (XarecTM) together with a substantial interest of the scientific community.[36-40] The special feature of s-PS is that is able to giving rise to *host-guest complexes*, where the host polymeric phase is a nanoporous crystalline phase and the guest molecules are organic molecules of suitable size and shape. The latter are related to its ability to co-cristallize with substances of low molecular weight, in fact exposed to particular solvents crystallizes in structures called clathrates.[41,42]

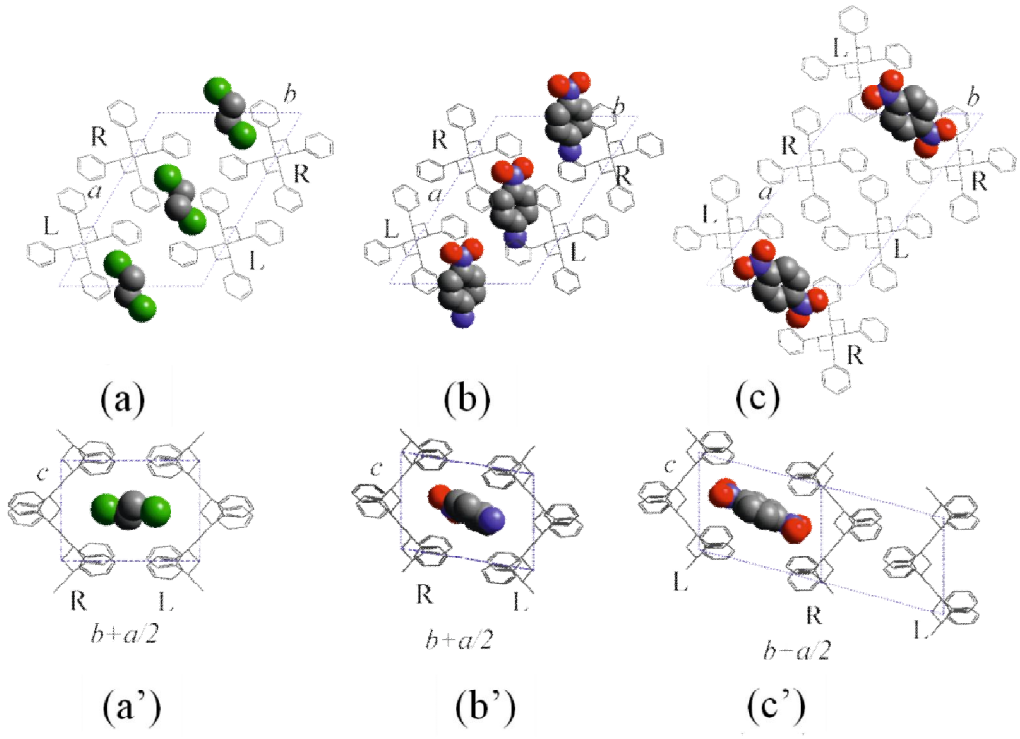

Fig. 2.2 Schematic projections along the chain (a–c) and perpendicular to the chain (a'–d') of s-PS co-crystalline forms: (a, a') δ clathrate with 1,2-dichloroethane; (b, b') δ clathrate with *p*-nitroaniline; (c, c') δ clathrate with 1,4-dinitrobenzene.

This structure enables small organic molecules to be hosted in the crystalline phase of s-PS to give the corresponding δ clathrates according to the nomenclature proposed by Guerra *et al.*[43]. The compounds that can clathrate are aromatic molecules, like benzene or toluene, small halogenated molecules, e.g. 1,2-dichloroethane, chloropropane or chloroform, or small oxygenated molecules such as tetrahydrofurane. In the δ clatrate structure of syndiotactic polystyrene, the guest molecules occupy cavities centrosymmetric isolated bounded by two adjacent polymer chains of opposite chirality left- and right- handed, see figure 2.2. And this is

precisely the peculiarity of these co-crystal structures, the formation of right-and left helixces that isolate guest molecules contained therein.

The δ-form of s-PS is a helical host-guest structure where the arrangement of the s-PS polymer chains creates nanopores that can accommodate small molecules. The δ nanoporous crystalline phase presents two identical cavities and eight styrene monomeric units per unit cell[44] (see figure 2.3). The δ-clathrated form can be transformed into the "empty" δ form (δe) by a proper treatment with acetone or acetonitrile, by which the included molecules can be removed, leaving voids in the crystalline phase.

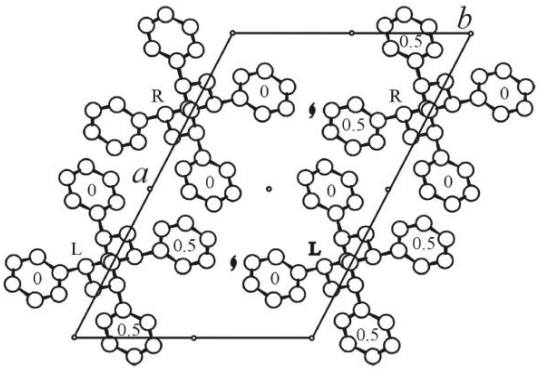

Fig. 2.3 Top view of the cristalline structure of the nanoporous cristalline δ phase. R= right handed helix, L= left handed helix.

Thus, the δe is able to sorb volatile organic compounds (both from gas phase and aqueous solutions), also when present at very low concentrations,[45-47] the sorption behavior of this structure has been studied in detail.[48-52] This crystalline phase can be considered as the first example of polymeric molecular sieves,[53] as it displays a high molecular sorption selectivity which is similar to zeolites. Then the empty δ form can also be treated with proper solvents to obtain new clathrates. The emptied clathrate form has been reported to have a lower density

than that of the amorphous phase of s-PS. The reported density of the δe-crystal of s-PS is 0.977 g/cm^3 compared to a density of 1.055 g/cm^3 for the amorphous phase of s-PS as reported by De Rosa and coworkers.[54] The s-PS co-crystalline forms exhibit, as a common feature, s(2/1)2 helical polymer conformation (Fig. 2.4), with a repetition period of nearly 7.8 Á. However, the packing of the host helices and of the guest molecules can largely change, mainly depending on the molecular structure of the guest molecules and also on the preparation procedure.

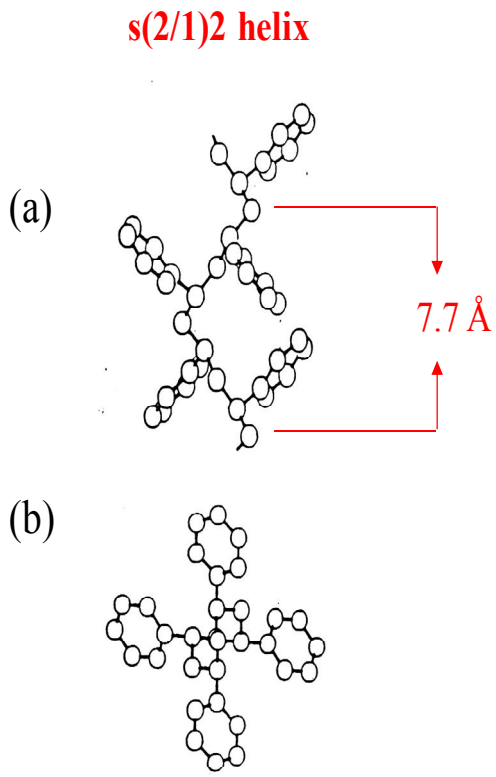

Fig. 2.4 Representation of the s(2/1)2 helical chain of s-PS: (a) lateral view and (b) top view.

The helical forms of sPS have gained considerable interest over the years due to specific arrangements of the sPS chains that can lead to the formation of nanocavities and nanochannels within the sPS crystalline phase. The potential to exploit these cavities and channels as hosts for the incorporation of different guest molecules remains to be a major research interest for the use of sPS as an inexpensive material for advanced technological applications.

2.3 Experimental section

This section describes the sample preparation procedure, also the induction of chirality in melt extruded syndiotactic polystyrene (s-PS) films of different thickness with a non-racemic guest and retained after exchange of the non-racemic guest with achiral chromophores (azulene and 4-nitro-aniline). Here, we compare the chiral optical responses of 4 and 20 μm melt extruded films. The s-PS used in this study was manufactured by Dow Chemical Company under the trademark Questra 101. The ^{13}C nuclear magnetic resonance characterization showed that the content of syndiotactic triads was over 98%. The weight-average molar mass obtained by gel permeation chromatography (GPC) in trichlorobenzene at 135°C was found to be $M_w=3.2 \times 10^5$ with the polydispersity index, $M_w/M_n=3.9$.

2.3.1 Chiral recognition and quantification

The most commonly used technique for examining chiral systems is analysis of its circular dichroism. Circular dichroism (CD) refers to a difference in absorbance (A) for left and right circular polarizations of light (ΔA = CD = $A_L - A_R$), displayed by chiral molecules and chiral materials. CD spectroscopy is commonly carried out in the ultra-violet (UV) and visible part of

the electromagnetic spectrum. The CD instrument generates LCP and RCP which are passed alternately through the sample. There is no absorption difference for achiral molecules against LCP and RCP ($A_L = A_R = \Delta A = 0$). Conversely, unpolarized light used in UV/VIS spectrophotometers is unsuitable for discrimination of enantiomers due to their identical absorption. However, LCP and RCP do interact differently with optically active materials resulting in a small but measurable difference in the light absorption of the sample. The absorption difference is expressed conventionally as $\Delta A = A_L - A_R$ and is plotted in the function of the wavelength. Accordingly, CD bands can be positive ($A_L > A_R$) or negative ($A_L < A_R$). Importantly, CD bands (called also Cotton effects) can only be measured where absorption bands are present.

A related technique that is becoming more widely applied is *vibrational circular dichroism* spectroscopy (VCD), which arises from chiral absorptions in the infrared regions, associated with bond bending and stretching. It had long been appreciated that extending natural optical activity into the vibrational spectrum could provide more detailed and reliable stereochemical information because a vibrational spectrum contains many more bands sensitive to the details of the molecular structure.[55] Vibrational circular dichroism (VCD) spectroscopy[56-58] has become a powerful tool for the determination of the absolute configurations of natural products,[59,60] metal complexes,[61] and synthetic materials, such as drugs[62] and polymers.[63,64]

For CD and VCD spectra the *anisotropy factor* G (termed also as Kuhn's dissymmetry ratio, degree of circular polarization or G factor). It is a dimensionless parameter expressing a ratio of the strength of CD to strength of light absorption of the chiral sample at specific wavelengths.

$$G = \frac{\Delta A}{A} = \frac{A_L - A_R}{{}^1/_2\ (A_L + A_R)}$$

where ΔA is the difference of the absorption of the sample against left- and right-circularly polarized light beams $(A_L - A_R)$. Due to historical reasons, most CD spectropolarimeters

produce CD spectra in units of in millidegrees (mdeg) versus wavelength (nm) although they directly measure differential absorbance values (ΔA). Thus, quantitative evaluations of the degree of circular polarization G based on the UV-Vis and CD spectra were effected by using the relationship 1mdeg = 32980 ΔA.[65]

CD spectra were measured using a Jasco J-715 spectropolarimeter. All measurements were performed using the following parameters: single scan, continuous scanning mode (350-190 nm range), 200 nm/min scanning speed, 2 nm SBW (constant bandpass mode), 0.2 nm data interval, vertical scale in autoranging mode, no baseline correction. The CD data have been expressed as the ellipticity (one mdeg equals 0.001 deg). IR and VCD measurements were recorded using a commercial Bruker Tensor 27 FT-IR spectrometer coupled to a PMA50 external module, (needed to double modulate the Infrared radiation) using a linear KRS5 polarizer, a ZnSe 50 KHz photoelastic modulator (PEM, by HINDS) with a proper antireflecting coating, an optical filter (transmitting below 2000 cm^{-1}) and a narrow band MCT (Mercury Cadmium Telluride) detector. All VCD spectra were recorded for 5 minutes of data collection time, at 4 cm^{-1} resolution. According to experimental procedures described in literature,[13] films were tested for satisfactory VCD characteristics by comparison of the VCD obtained with the film rotated by ±45°C around the light beam axis. In separate measurements with 1h data collection time, we have also tested ±90° rotation of the film, VCD bands were found to be unaffected by changing collection time as well as by changing the rotation of the film. To eliminate any possible linear dichroism influence, the CD and VCD measurements have been conducted by averaging the spectra as collected for several different in-plane rotation angles.

2.3.2 Induction of chirality with a non-racemic guest

Robust chiral-optical films, are easily obtained by co-crystallization of amorphous s-PS films as induced by sorption of many volatile non-racemic (also temporary) guest molecules.[11]

The macromolecular amplification of chirality in polymer co-crystalline phases can be produced by molecular[66] and supramolecular mechanisms. A supramolecular mechanism occurs when the non-racemic guest induces the formation of non-racemic helical crystallites, whose unit cell is a racemic one and includes both right- and left-handed polymer helices. This induction of macromolecular helicity by non-chiral guests leads to amplification of chirality that can be clearly confirmed by vibrational circular dichroism (VCD) measurements and by CD Cotton bands of the polymer in the UV region. This supramolecular mechanism has been presently observed only for syndiotactic polystyrene (s-PS).[13] This chiro optical response remains unaltered and can be erased only after thermal treatments at temperatures higher than the s-PS melting temperature ($\approx$ 270° C).

In the past, the above described chiral optical behavior have been observed for thin films obtained by spin coating (typical thickness of 0.1 μm)[11-15,18,19] but also for 20 μm thick films obtained by melt extrusion. Here, we compare the chiral optical responses of melt extruded films of different thickness 4 and 20 μm. The chirality is induced in amorphous s-PS films after sorption of non–racemic carvone (figure 2.5) for 1 hour at room temperature. R-carvone (98%, e.e. 98%), S-carvone (96%), were supplied by Aldrich and were used without further purification.

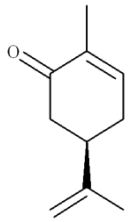

(R)-(–)-Carvone

Fig. 2.5 Molecular structure of carvone enantiomer.

In figure 2.6 are reported Fourier transform Infrared (FTIR) and VCD spectra of amorphous s-PS films after sorption of (-)-(R)-carvone and (+)-(S)-carvone shown as red and blue lines, respectively (Fig. 2 A', B').[67] For both films, according to thermogravimetric analyses, the carvone content is close to 8 wt %. The VCD spectra of figure show many intense peaks, being of opposite signs for film treated with (S)- and (R)- Carvone.

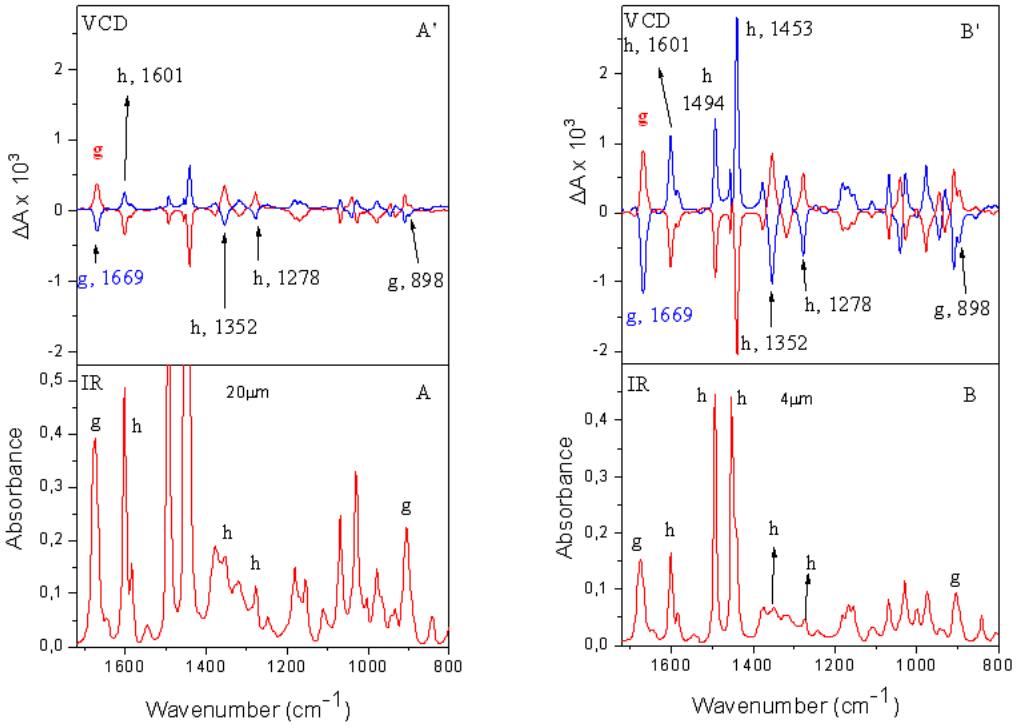

Figure 2.6 FTIR (A, B) and VCD spectra (A', B') of amorphous s-PS films, having a thickness of nearly 20μm (A, A') or 4 μm (B, B'), after crystallization induced by sorption of (-)-(R)-carvone (thin red line) or (+)-(S)-carvone (thick blue line). The main peaks of the carvone guest are labeled by **g** while some typical peaks of polymer host are indicated by **h**.

We immediately notices an amplification of chirality in the thinner film, in particular, the 4 μm film which presents lower absorbance peaks (figure 2.6B) unexpectedly presents much more

intense VCD peaks (figure 2.6B'). As a mentioned before, VCD analysis is able to give us major information about guest and host peaks, in fact large circular dichroism values are observed for many polymer host peaks, see e.g. at 1601, 1352, 1278 cm^{-1} associated with the helices of the crystalline phase,[68] visible for the thicker and thinner film and other peaks at 1494, 1453 cm^{-1} visible only for 4 μm film.[69]

Large circular dichroism values are observed not only for many polymer host peaks but also for the nonracemic guest (e.g at 1669, 898 cm^{-1}). It is also possible to extract quantitative evaluations of the anisotropy factor G for some host (G_h) and guest (G_g) peaks, collected in Table 1, confirms that by reducing the film thickness from 20 μm to 4 μm, there is an increase of the degree of circular polarization of one order of magnitude.

	$G_{g/carvone}$		G_h		
Wavenumber (cm^{-1})	**1669**	**898**	**1601**	**1352**	**1278**
4 μm film	$7x10^{-3}$	$5x10^{-3}$	$7x10^{-3}$	$1x10^{-2}$	$1x10^{-2}$
20 μm film	$7x10^{-4}$	$5x10^{-4}$	$7x10^{-4}$	$1x10^{-3}$	$1x10^{-3}$

Table 1. Quantitative evaluations based on the FTIR and VCD spectra of Figure 2, of the anisotropy factor for some peaks of the carvone guest (G_g) and of the polymer host (G_h).

The spectra of figure 2.6 and the derived Table 1 also indicate that the anisotropy factor is higher for the racemic host than for the non-racemic guest, mainly for the helical peaks (like those at 1352 and 1277 cm^{-1}) being associated with a single vibrational mode of the s(2/1)2 polymer helix.[70,71]

The same amplification of chirality is also obtained by UV-vis and CD spectra of the melt extruded s-PS amorphous film, with a thickness of 4 μm, after crystallization induced by immersion in pure (R)-carvone (red line) or (S)-carvone (blue line) see figure 2.7, respectively. The UV spectrum (figure 2.7A) clearly shows typical absorbance peaks of polystyrene,[72-75]

while the CD spectra (figure 2.7B) show intense peaks at 262, 265 and 269 nm and a less intense ill-defined band of opposite sign below 250 nm.

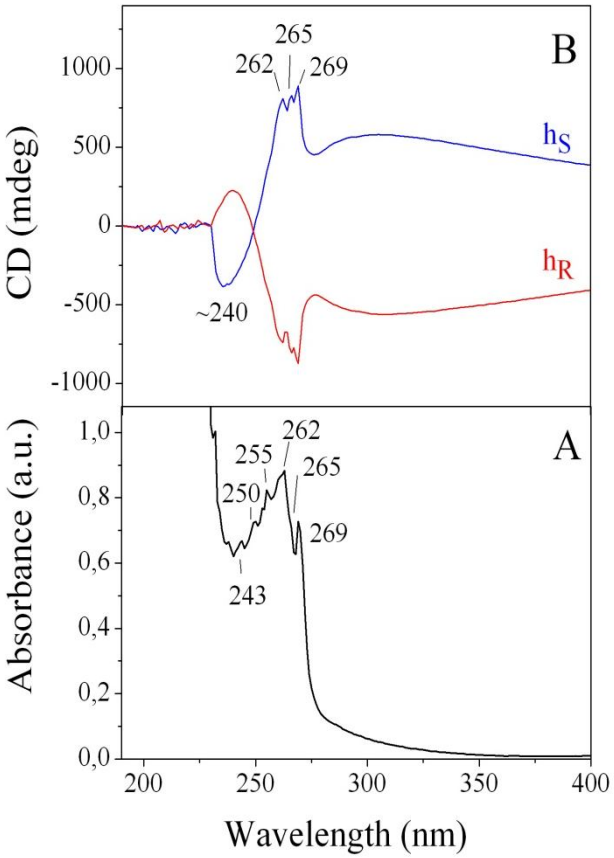

Figure 2.7 UV-Visible (A) and CD (B) spectra of a s-PS amorphous films, with a thickness of 4 μm, after (-)-(R)-carvone (red line) or (+)-(S)-carvone (blue line) induced crystallization.

These polystyrene CD peaks were not accessible for much thinner spin-coated films (0,1 μm), which only show intense peaks located at 200 and 223 nm (Figure 3C),[11-15] neither for thicker films (20 μm), which present a too high absorbance in this spectral region because it is worth

nothing that, for such a thickness for the study of the chiral sensitivity, the available UV-vis CD technique is not applicable.[76]

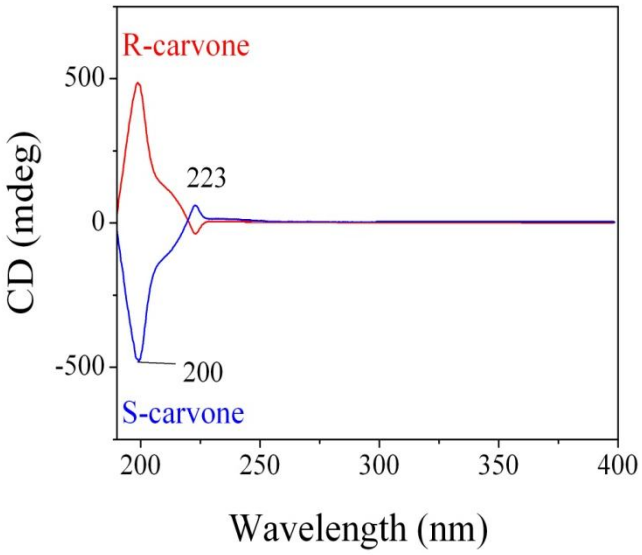

Fig. 2.8 CD spectra of s-PS spin-coated amorphous films, having a thickness of 0.1 μm, after (-)-(R)-carvone (red line) or (+)-(S)-carvone (blue line) induced crystallization.

Quantitative evaluations of the anisotropy factor *G* based on the UV-Vis and CD spectra of figure 2.7 A,B (~ 260 nm) show a G_h factor value of roughly $3 \cdot 10^{-2}$ and is a value close to those evaluated by IR and VCD measurements on the helical host peaks at 1352 and 1277 cm^{-1} (Table 1).

The formation of chiral crystallites as a consequence of co-crystallization of an amorphous s-PS film with non-racemic guest molecules is confirmed by AFM images of melt extruded chiral optical s-PS films, having a thickness of 4μm like those of figures 2.6 and 2.7, are presented in figure 2.9. Images are acquired using a commercial Atomic Force Microscope (Nanoscope IIIa, Bruker) in Tapping mode in air. The levers (Bruker) used for this

investigation have a nominal spring constant of 5N/m and resonance frequency around 130kHz, the nominal tip radius of curvature is of 10nm.

The images show helical crystallites, somewhat similar to those reported for spin-coated s-PS chiral optical films with thickness of nearly 0.1 μm (figure 8 of ref. 3b). However, for the melt extruded films of figure 2.9, the crystallites are more closely packed as well as more aligned. As observed for many different systems,[77] the molecular chirality is expressed at a scale of 370 and 160 nanometers, giving rise to coiled fiber structures that are observable by microscopic techniques.

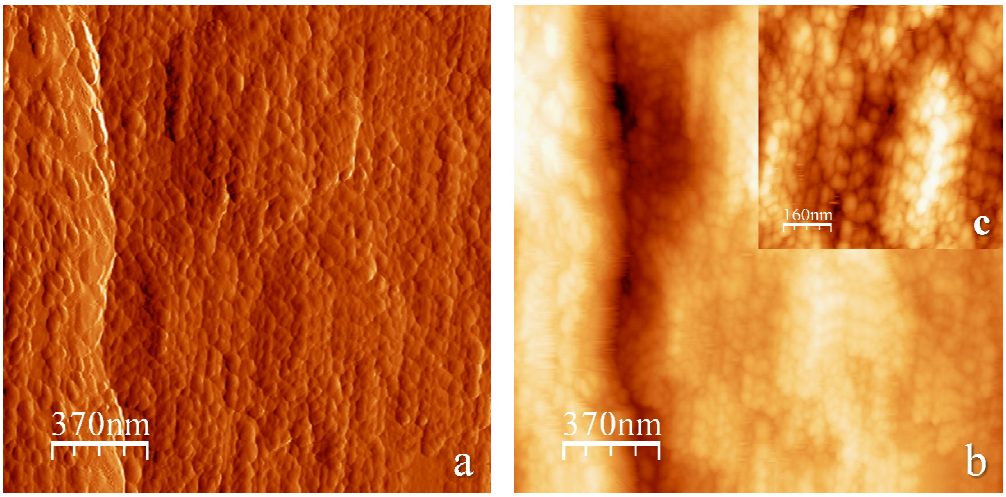

Fig. 2.9 AFM images for a s-PS melt extruded amorphous films, with a thickness of 4 μm, after carvone induced crystallization. **a** image represents the real topography of the sample (Rms Roughness: 37.21nm) while **b** and **c** images refers to the AFM amplitude signal, which is used to highlight changes in surface height and image expressed at a scale of 370 and 160 nm, respectively.

2.3.3 Stable supramolecular chirality

In the last few years, it has been also discovered that polymer co-crystallization induced by non-racemic guest molecules, as we have seen, can produce large and extremely, but also stable circular dichroism (CD) phenomena.[11] In fact, it has been observed that syndiotactic polystyrene films are able to transfer, amplify and memorize the chirality of non-racemic low-molecular-mass molecules.[78]

In figure 2.10, the VCD spectra of the same films is reported after complete carvone removal by immersion in acetonitrile for 1h (and acetonitrile complete desorption in air at room temperature). The VCD spectra show that the chiral response of the polymer host remains unaltered after complete non-racemic carvone removal, clearly indicating the induction of stable chirality in the racemic polymer. This is confirmed by quantitative evaluations of the degree of circular polarization G associated with vibrational modes of the s(2/1)2 helices of the s-PS crystalline phases[6] ($G_h(1352) \approx G_h(1278) \approx 1x10^{-2}$), which present the same values reported in table 1.

This result confirms the hypothesis (Buono et al. 2007) that CD phenomena induced in amorphous s-PS films by the temporary sorption of non-racemic guests are not due to the formation of non-racemic unit cells but to the formation of non-racemic morphologies of co-crystalline phases, which are maintained also after solvent treatments.

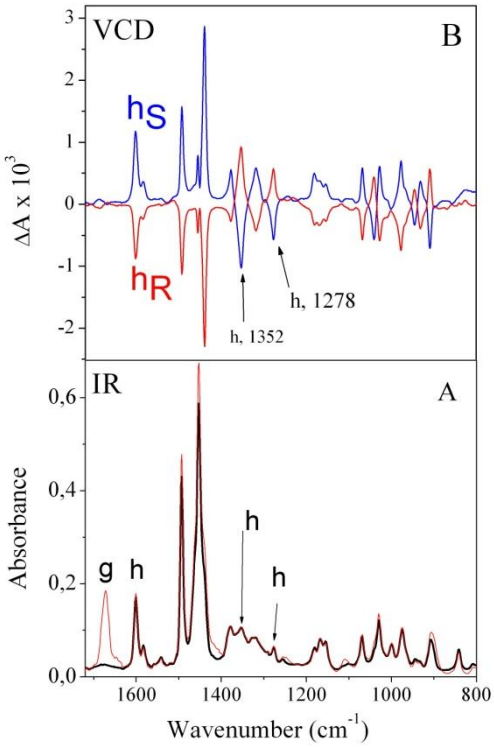

Fig. 2.10 FTIR (A) and VCD spectra (B) of amorphous s-PS films, having a thickness of nearly 4 μm, after crystallization induced by sorption of (+)-(S)-carvone (blue line) or (-)-(R)-carvone (red line) and complete carvone removal. The peak of the carvone guest is labeled by **g** while the most intense peaks of the polymer host are indicated by **h**.

The same films have been treated again by non-racemic carvone, by immersion on pure (-)-(R)- or (+)-(S)-carvone at 50°C for 1h their VCD spectra are in figure 2.11 and their VCD spectra are reported in figures 2.11A' and 2.11B', respectively. The chiral response of the host remains unchanged (h_R or h_S) while the chiral response of the guest is of kind g_R or g_S, depending on the chirality induced in the crystalline phase of the polymer host by the first crystallization and is independent of the intrinsic chirality (molecular chirality) of the guest. These results indicate that for non-racemic molecules being guest of s-PS films, the intrinsic

(molecular) contribution to the circular dichroism is negligible with respect the extrinsic (supramolecular) contribution of which exhibit supramolecular chirality.[79]

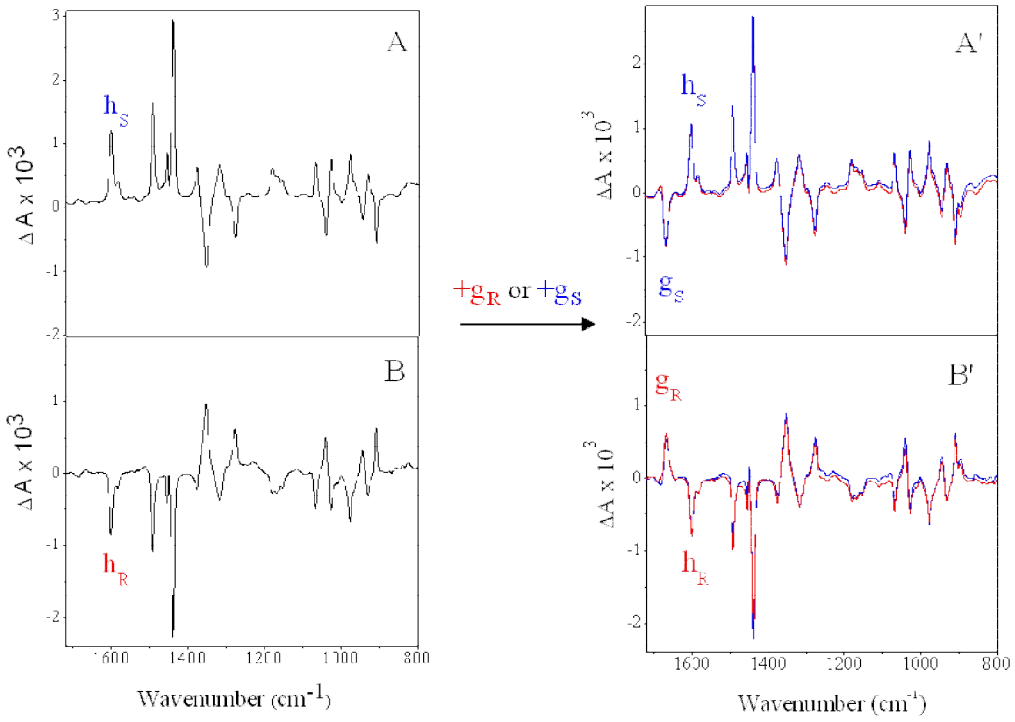

Figure 2.11 VCD spectra of chiral optical s-PS films as obtained by crystallization by (+)-(S)-carvone (A, A') or (-)-(R)-carvone (B, B'): (A,B) after complete carvone removal; (A',B') after renewed sorption of (+)-(S)-carvone (thick blue line) or (-)-(R)-carvone (thin red line) for 1h at 50°C.

2.3.4 Guest exchange with achiral chromophores

Recently, s-PS based films with intense chiral optical responses at visible wavelengths have been obtained by exchanging the non-racemic guest with achiral chromophores, provided that: the initial crystallization of s-PS has been induced by a non-racemic guest from an amorphous phase and the chromophore molecules are suitable guest of a s-PS co-crystalline form.[18,19]

In this section, we present chiral optical films based on s-PS, obtained by co-crystallization with a non-racemic guest, exhibiting stable circular dichroism phenomena also in the visible region. The chiral s-PS films have been treated with two different chromophores whose size is suitable to fit the crystalline cavity of the nanoporous δ phase,[15,16] i.e. azulene and 4-nitro-aniline (NA) (figure 2.13).

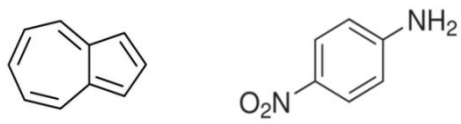

azulene 4-nitro-aniline

Fig. 2.12 Molecular structure of the achiral chromophores: azulene and 4 nitro-aniline.

Thus, intense VCD and CD phenomena have been obtained by direct guest exchange,[80,81] immersing the 20 and 4 μm films in a 3.5 wt% azulene solution in CH_2Cl_2 for 3 h, followed by CH_2Cl_2 desorption at room temperature. The results are reported in figure 2.13.[67] The thermogravimetric analyses reveals that the azulene content for both films are close to 14 wt %. The VCD spectra of figure show many intense peaks, being of opposite signs for films crystallized by (-)-(R)-carvone (red line) or (+)-(S)-carvone (blu line).

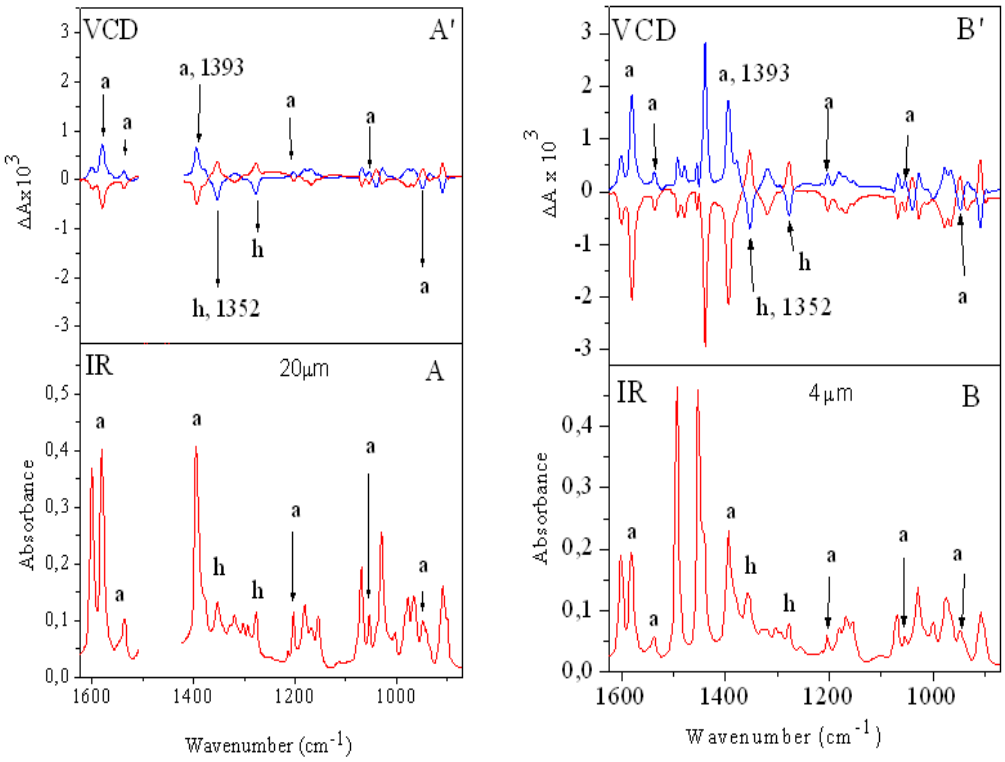

Figure 2.13 FTIR (A, B) and VCD spectra (A', B') of s-PS films, having a thickness of nearly 20μm (A, A') or 4 μm (B, B'), after crystallization induced by (-)- (R)-carvone (red line) or (+)-(S)-carvone (blue line) and exchange of the non-racemic carvone guest with the achiral azulene guest. The azulene content is close to 14 wt%. The main peaks of the azulene guest molecules are labeled by **a** while some typical polymer host peaks are indicated by **h**.

Again the thinner film which presents lower absorbance peaks (figure 2.13B) presents much more intense VCD peaks (figure 2.13B'). Thus, by the evaluation of g factor we can observe an increase of degree of circular polarization both for host and guest peaks of nearly one order of magnitude. In particular, *G* factors evaluated on the host helical peak at 1352 cm^{-1} (G_h) are

similar to *G* factor evaluated on the azulene peak at 1393 cm^{-1} (G_a) and close to $1x10^{-3}$ and $1x10^{-2}$ for the films having thickness of 20 μm and 4 μm, respectively.

The same chiral optical behavior is also observed for the UV-vis and CD spectra of the s-PS films, with a thickness of 20 μm and 4 μm, reported in figure 2.14.

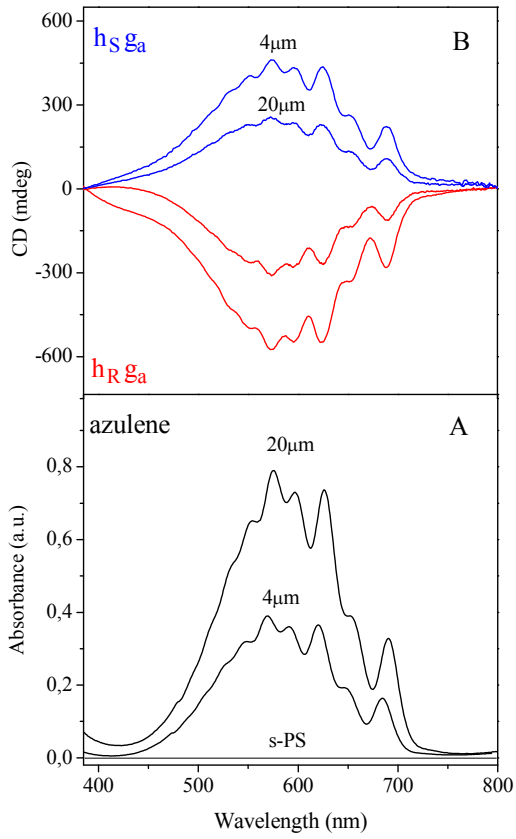

Figure 2.14 Visible (A) and CD (B) spectra, in the range 400-800 nm, of s-PS films, with thickness of 20 μm and 4 μm, after (-)-(R)-carvone (red line) or (+)-(S)-carvone (blue line) induced crystallization and replacement of the non-racemic carvone guests with the achiral azulene guest. Corresponding FTIR and VCD spectra are shown in Figure 2.13 B,B'.

The investigated range 450-710 nm presents azulene band which is negative or positive depending on the S or R chirality of the carvone used to induce the initial crystallization to amorphous s-PS (as already shown in figure 2 of ref 18). The spectra of figure 2.14 show that, also for the Visible region, the thinner film (4 μm) presents definitely more intense CD bands (figure 2.14B), although presents a much less intense absorbance band (Figure 2.14A). Quantitative evaluations of the degree of circular polarization *G* for the azulene visible band in the range 450-710nm, based on the spectra of Figure 2.14A and 2.14B, show G factors close to $1x10^{-2}$ and $4x10^{-2}$, for sPS films with a thickness of 20 μm and 4 μm, respectively.

FTIR and VCD spectra of s-PS 20 μm and 4 μm films, exhibiting δ clathrate phase with NA,[82] obtained by crystallization of amorphous film by (-)-(R)- and (-)-(S)- carvone sorption, followed by guest-exchange (by immersion in a NA saturated CH_2Cl_2 solution for 3 h) are shown in figure 2.15.

As already observed for chiral films with carvone or with azulene, it is immediately apparent that the thinner film presenting lower absorbance peaks presents more intense VCD peaks, with increases of degree of circular polarization both for host and guest peaks of nearly one order of magnitude. In particular, *G* values evaluated on the host helical peak at 1352 cm^{-1} (G_h) and of NA peak at 1620 cm^{-1} (G_{NA}) are $1x10^{-2}$ and $3x10^{-2}$, respectively.

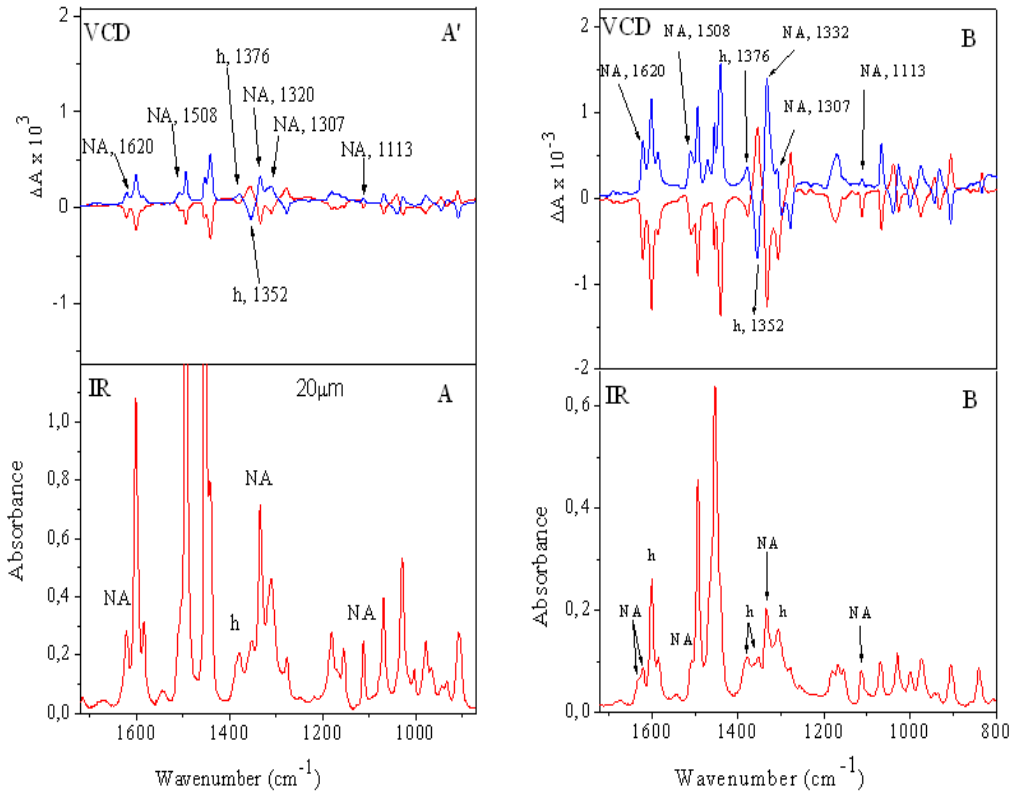

Figure 2.15 FTIR and VCD spectra of s-PS film, having a thickness of nearly 4 μm, after crystallization induced by (-)-(R)-carvone (red line) or (+)-(S)-carvone (blue line) and after exchange of the non-racemic carvone guest with the achiral NA guest (guest content close to 3 wt%). The main peaks of NA guest molecules are labeled by **NA** while some typical peaks of polymer host are indicated by **h**.

The 4-nitro-aniline has a particular behavior, it is able to enter in the crystalline and in the amorphous polymer phase, as confirmed by FTIR absorption spectrum in the N-H stretching region (3550-3300 cm^{-1}) reported in figure 2.16. The spectrum collected after partial CH_2Cl_2 desorption (in air at room temperature for 72 hours, figure 2.16 curve a) displays beside the absorption bands at 3500 ($\nu_{as}(NH_2)$[19]) and 3400 cm^{-1} ($\nu_s(NH_2)$[19]), typical of isolated NA molecules being guest of s-PS (δ or ε) clathrates,[12b,18] two more intense bands at 3483 and

3361 cm^{-1}, possibly associated with NA molecules aggregated by hydrogen bonds in the amorphous polymer phase. The spectra collected on the same film after complete CH_2Cl_2 removal by immersion in acetonitrile for 10 min, followed by partial (30 minutes) and complete (4 hours) acetonitrile desorption at room temperature, are shown in figure 2.16 curves b and c, respectively. The spectrum of figure 2.16 curve c shows that the complete removal of CH_2Cl_2 is accompanied by reduction of the NA content (from 3 wt% down to 1.5 wt%) as well as by the disappearance of N-H stretching bands at 3483 and 3361 cm^{-1}. The spectrum of figure 2.16 curve b, shows that the film subjected to a partial acetonitrile desorption presents nearly the same amount of NA (1.5 wt%) than the film of figure 2.16 curve c, for more details see ref 67.

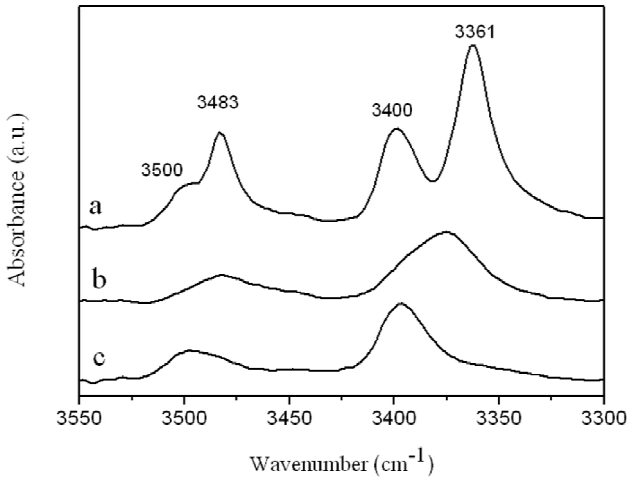

Figure 2.16 FTIR spectra in the 3550-3300 cm^{-1} range of a s-PS 4μm film exhibiting the δ clathrate form with NA, as obtained by crystallization by carvone sorption as followed by guest-exchange by immersion in a NA saturated CH_2Cl_2 solution: (a) after CH_2Cl_2 desorption at room temperature; (b,c) after immersion in acetonitrile for 10 min, followed by partial (b) or complete (c) acetonitrile desorption at room temperature.

However, the two N-H stretching bands present a component at higher wavelengths, which can be rationalized by the presence of a substantial fraction of NA molecules in the amorphous phase, due to the temporary occupation of some crystalline cavities by the volatile acetonitrile guest.[83] A rough evaluation suggests that the fraction of NA included in the polymer co-crystalline phase is lower than 50% and close to 100%, for the films of Figures 2.16 curves b and c, respectively.

Also, in this situation we observe intense phenomena of circular dichroism of the s-PS, see figure 2.17. The UV-Visible spectrum is relative of a s-PS 4 μm films with a NA content close to 3 wt% and is reported in figure 2.17A. The CD spectra present a broad intense NA band in the range 300-400 nm, beside a minor broad band in the range 275-290 nm, which are negative or positive depending on the R or S chirality of the carvone used to induce crystallization in amorphous s-PS. It is worth noting that the films presenting most NA molecules as guest of the polymer co-crystalline phase (curves c in figure 2.17B) show more intense CD peaks than the films presenting the same amount of NA but with a large fraction dissolved in the amorphous phase rather than included in the crystalline phase (curves b in Figure 2.17B); in particular, *G* values evaluated on the NA band at 343 nm are of nearly $5x10^{-2}$ and $1x10^{-1}$ for samples reported in figure 2.17B curves b and c, respectively.

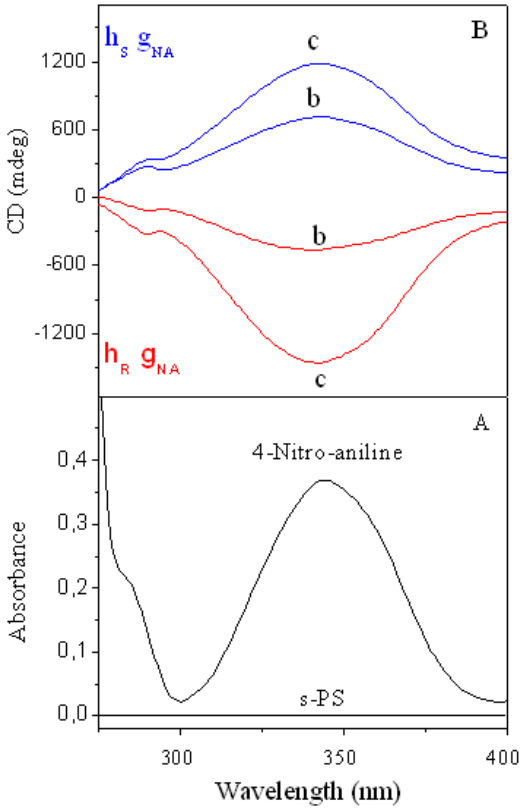

Figure 2.17 UV-Visible (A) and CD (B) spectra, in the range 275-400 nm, of s-PS 4 μm films, exhibiting the δ clathrate phase with NA, with NA content close to 3 wt%. The CD spectra labeled **b** and **c** correspond to the samples whose FTIR spectra are shown in figure 2.16b and 2.16c, for which the fraction of NA included in the polymer co-crystalline phase is lower than 50% and close to 100%, respectively. red lines and blue lines correspond to films firstly crystallized by sorption of (-)-(R)-carvone or (+)-(S)-carvone, respectively.

This is confirmed observing better the FTIR spectra of figure 2.15 in the NH_2 deformation region (1640-1620 cm^{-1}) which presents a double component located at 1632 cm^{-1} and 1620 cm^{-1}. In the VCD spectra the dichroic peak is located only at 1620 cm^{-1}; this results confirms the previous conclusion (based on comparison between VCD data of azulene molecules being guest of chiral s-PS film exhibiting δ or α crystalline forms)[8a] that the chiral optical response of

achiral guest chromophores only occurs when such molecules are included as guest in the nanoporous crystalline phase, rather than simply dissolved in the amorphous phase.

2.4 Conclusions and perspectives

The chirality induced on melt extruded s-PS films of different thickness by co-crystallization with a non-racemic guest (carvone), has been studied. The intense VCD phenomena, already observed for 20 μm films, are markedly increased for 4 μm films. In particular, the degree of anisotropy factor (*G*) relative to VCD peaks, both for polymer host and for low-molecular-mass non-racemic as well as achiral (azulene and NA) guests, increases of one order of magnitude.

The use of chiral films with a thickness of 4 μm has also allowed to identify intense CD peaks at 262, 265 and 269 nm of polystyrene, that were not accessible for much thinner spin-coated films (0,1 μm) and for thicker films (20 μm), which exhibit in this spectral region too low CD signals and too high UV absorbance, respectively.

VCD analysis of s-PS films in which non-racemic molecules are included as guest, indicate that the intrinsic (molecular) contribution to the circular dichroism is negligible with respect the extrinsic (supramolecular) contribution of which exhibit supramolecular chirality.

CD spectra of s-PS films including the co-crystalline form with NA confirm that the chiral optical response of achiral guest chromophores occurs when such molecules are included as guest in the nanoporous crystalline phase, rather than simply dissolved in the amorphous phase.

As for the chiral optical behavior of melt extruded s-PS films, as induced by co-crystallization with non-racemic guest molecules, we presently show an unprecedented strong increase of *G* with decreasing the thickness. On the basis of our analysis, we suggest that the unexpected *G* increase with reduction of the extruded film thickness, can be rationalized by a more efficient formation of chiral crystallites close to the film surfaces possibly due to the higher carvone concentration.**.** For a possible discrimination of the intensive or extensive nature of G for s-PS

chiral optical films, comparison between thin films, as obtained by spin-coating,[3] exhibiting different thickness, would be needed.

The realization of chiral optical films that exhibit stable and amplificated circular dichroism phenomena in the visible region opens the possibility to achieve s-PS based films with chiral optical response at desire wavelengths. In this respect, it is worth adding that s-PS can be easily melt processed leading not only to films but also to solid samples of any shape, which can be made fully amorphous by simple quenching procedures. As a consequence, materials and devices exhibiting chiral-optical responses in selected wavelengths, based on s-PS, can be easily designed and produced. This allows an easy production of optically active transparent films, whose CD peaks can be controlled by the choice of (also achiral) chromophore guest molecules. The capacity of syndiotactic polystyrene films, presenting a suitable nanoporous host crystalline phase, to transfer, amplify and memorize the chirality of non-racemic low molecular-mass molecules associated with a high thermal stability of these VCD phenomena, and hence of the memory of the non-racemic guest molecules suggest a possible application of these polymer films as chiro-optical memories and optical applications.

References:

1 J. S. Seo, D.Whang, H. Lee, S. I. Jun, J. Oh, Y. J. Jeon, K. Kim, *Nature.* 404, 982 (2000).

2 T.Verbiest, S. van Elshocht, M. Kauranen, L. Hellemans, J. Snauwaert, C. Nuckolls, T. J. Katz, A. Persoons, *Science* 282, 913 (1998).

3 S. K. Jha, K.-S. Cheon, M. M. Green, J. V. Selinger, *J. Am. Chem. Soc.* 121, 1665 (1999).

4 K. Akagi, G. Piao, S. Kaneko, K. Sakamaki, H. Shirakawa, M. Kyotani, *Science 282*, 1683 (1998).

5 L. J. Prins, J. Huskens, F. de Jong, P. Timmerman, D. N. Reinhoudt, *Nature* 398, 498 (1999).

6 Y. Furusho, T. Kimura, Y. Mizuno, T. Aida, *J. Am. Chem.Soc.* 119, 5267 (1997).

7 B. L. Feringa, R. A. van Delden, N. Koumura, E. M. Geertsema, *Chem. ReV.* 100, 1789 (2000).

8 S. Zahn, J. W. Canary, *Science.* 288, 1404 (2000).

9 C. Train, R. Gheorghe, V. Krstic, L.-M. Chamoreau, N. S. Ovanesyan, G. L. J. A. Rikken, M. Gruselle, and M. Verdaguer, *Nat. Mater.* 7, 729–734 (2008).

10 G. Guerra, C. Daniel, P. Rizzo, O. Tarallo, *J. Polym. Sci. Polym. Phys. Ed,* 50, 305-22 (2012).

11 A. M. Buono, I. Immediata, P. Rizzo, G. Guerra, J. *Am. Chem. Soc*., 129, 10992-93 (2007).

12 L. Guadagno, M. Raimondo, C. Silvestre, I. Immediata, P. Rizzo, G. Guerra, *J.Mater.Chem.* 18, 567-72 (2008).

13 P. Rizzo, M. Beltrani, G. Guerra, *Chirality* 22, E67-E73 (2010).

14 P. Rizzo, C. Daniel, G. Guerra, *Macromolecules* 43, 1882-87 (2010).

15 C. De Rosa, G. Guerra, V. Petraccone, B. Pirozzi, *Macromolecules* 30, 4147-52 (1997).

16 G. Milano, V. Venditto, G. Guerra, L. Cavallo, P. Ciambelli, D. Sannino, *Chem. Mater.* 13, 1506-11 (2001).

17 E. B. Gowd, N. Shibayama, K. Tashiro, *Macromolecules* 39, 8412-18 (2006).

18 P. Rizzo, T. Montefusco, G. Guerra, *J Amer Chem Soc*. 133, 9872-77 (2011).

19 G. Guerra, P. Rizzo, *Rendiconti*. 24, 217-226 (2013).

20 A. Douhal, *Chem. Rev*. 104, 1955–1976 (2004).

21 C. Lin, Y. Liu, C. Lai, S. Peng, and S. Chiu, *Chemistry 2*, 4594–4599 (2006).

22 C. De Rosa, G. Guerra, V. Petraccone, and B. Pirozzi, *Macromolecules* 30, 4147–4152 (1997).

23 G. Milano, V. Venditto, G. Guerra, L. Cavallo, P. Ciambelli, and D. Sannino, *Chem. Mater.* 13, 1506–1511 (2001).

24 P. Rizzo, C. Daniel, A. De Girolamo Del Mauro, and G. Guerra, *Chem. Mater.*19, 3864–3866 (2007).

25 V. Petraccone, O. Ruiz de Ballesteros, O. Tarallo, P. Rizzo, and G. Guerra, *Chem. Mater.* 20, 3663–3668 (2008).

26 N. Tomotsu, T. H. Newman, M. Takeuchi, R. Campbell, and J. Schellenberg *John Wiley & Sons, Inc.* (2009).

27 A. Zambelli, P. Longo, C. Pellecchia, A. Grassi, *Macromolecules 20*, 2035 (1987).

28 J. Schellenberg and N. Tomotsu Progress in *Polymer Science* 27, 1925-1982 (2002).

29 J. Schellenberg *Progress in Polymer Science* 34, 688-718 (2009).

30 E.M. Woo, Y.S. Sun, and C. P. Yang *Progress in Polymer Science* 26, 945-983 (2001).

31 E. B. Gowd, K. Tashiro, and C. Ramesh *Progress in Polymer Science* 34, 280-315 (2009).

32 N. Tomotsu, M. Malanga, and J. Schellenberg, *John Wiley & Sons, Ltd*. (2003).

33 N. Tomotsu, and N. Ishihara, In: H. Hideshi and O. Kiyoshi, editors. Studies in Surface Science and Catalysis, vol. Volume 121: Elsevier, pp. 269-276 (1999).

34 R.N. Tharanathan, N. Saroja, *J. Sci. Ind. Res.* 60, 547-559 (2001).

35 T. Fiola, A. Okada, M. Mihara, and K. Nichols Applications of Syndiotactic Polystyrene: *John Wiley & Sons, Inc.* (2009).

36 R. Po, N. Cardi, *Prog. Polym. Sci*. 21, 47 (1996).

37 N. Tomotsu, N. Ishihara, T. H. Newmann, M. T. Malanga, *J.Mol. Catal.* 128, 167, (1998).

38 M. T. Malanga, *Adv. Mater*. 12, 1869 (2000).

39 J. Schellenberg, N. Tomotsu, *Prog. Polym. Sci*. 27, 1925 (2002).

40 S. D. Amin, T. S. Marks, *Angew. Chem*. 47, 2, (2008).

41 C. De Rosa, P. Rizzo, O. Ruiz de Ballesteros, V. Petraccone, G. Guerra, *Polymer* 40, 2103-10 (1999).

42 O. Tarallo, V. Petraccone, A. R. Albunia, C. Daniel, G. Guerra, *Macromolecules* 43, 8549-58 (2010).

43 G. Guerra, V. M. Vitagliano, C. De Rosa, V. Petraccone, C. Corradini *Macromolecules*. *23*, 1539 (1990).

44 C. De Rosa, G. Guerra, V. Petraccone, and B. Pirozzi, *Macromolecules* 30, 4147–4152 (1997).

45 C. Manfredi, M. A. Del Nobile, G. Mensitieri, G. Guerra, and M. Rapacciuolo, *J. Polym. Sci.* 35, 135–140 (1997).

46 C. Daniel, D. Alfano, V. Venditto, S. Cardea, E. Reverchon, D. Larobina, G. Mensitieri, and G. Guerra, *Adv. Mater* 17, 1515–1518 (2005).

47 C. Daniel, D. Sannino, and G. Guerra, *Chem. Mater* 20, 577–582 (2008).

48 C. Manfredi, M. A. Del Nobile, G. Mensitieri, G. Guerra, and M. Rapacciuolo *Journal of Polymer Science Part B: Polymer Physics* 35, 133-140 (1997).

49 D.A. Rani, Y. Yamamoto, A. Saito, M. Sivakumar, Y. Tsujita, H. Yoshimizu, and Kinoshita T. *Journal of Polymer Science Part B: Polymer Physics* 40, 530-536 (2002).

50 M. Sivakumar, KPO. Mahesh, Y. Yamamoto, H. Yoshimizu, and Y. Tsujita Journal of *Polymer Science Part B: Polymer Physics*. 43, 1873-1880 (2005).

51 G. Guerra, C. Manfredi, P. Musto, and S. Tavone *Macromolecules.*31, 1329-1334 (1998).

52 KPO. Mahesh, M. Sivakumar, Y. Yamamoto, Y. Tsujita, H. Yoshimizu, and S. Okamoto *Journal of Membrane Science* 262, 11-19 (2005).

53 G. Guerra, G. Milano, V. Venditto, P. Musto, C. De Rosa, and L. Cavallo, *Chem. Mater.* 12, 363–368 (2000).

54 C. De Rosa, G. Guerra, V. Petraccone, and B. Pirozzi *Macromolecules* 30, 4147-4152 (1997).

55 L.D. Barron, Molecular Light Scattering and Optical Activity, *2nd edn, Cambridge University Press, Cambridge* (2004).

56 L. A. Nafie, *Vibrational Optical Activity, Wiley, Chichester* (2011).

57 G. Yang, Y. Xu, *Top. Curr. Chem*. 298, 189 – 236 (2011).

58 Y. He, W. Bo, R. K. Dukor, L. A. Nafie, *Appl. Spectrosc*. 65, 699 – 723 (2011).

59 E. BurgueÇo-Tapia, C. M. C. Garc_a-Rojas, P. Joseph-Nathan, *Phytochemistry* 74, 190 – 195 (2012).

60 J. M. Batista, A. N. L. Batista, J. S. Mota, Q. B. Cass, M. J. Kato, V. S. Bolzani, T. B. Freedman, S. N. Lopez, M. Furlan, L.A. Nafie, *J. Org. Chem*. 76, 2603 – 2612 (2011).

61 H. Sato, H. Uno, H. Nakano, *Dalton Trans*. 40, 1332 –1337 (2011).

62 Freedman T. B., Dukor R. K., van Hoof P. J. C. M.,. Kellenbach E. R,. Nafie L. A, *Helv. Chim. Acta.* 85, 1160 – 1165 (2002).

63 C. Merten, A. Hartwig, *Macromolecules* 43, 8373 – 8378 (2010).

64 H.-Z. Tang, E. R. Garland, B. M. Novak, J. Polavarapu, P. L. He, F. C. Sun, S.S. Sheiko, *Macromolecules* 40, 3575 – 3580 (2007).

65 Alison Rodger and Bengt Nordén, *Oxford chemistry masters* (1997).

66 D. La Camera, V. Petraccone, S. Artimagnella, O. Ruiz de Ballesteros, *Macromolecules* 34, 7762-66 (2001).

67 E. Lepera, P. Rizzo, G. Guerra, ACS Photonics, submitted.

68 E. Grana, D. Katsigiaannopoulos, A.E. Karantzalis, M. Baikousi, A. Avgeropoulos *European Polymer Journal* 49,1089-1097 (2013).

69 F. J. Torres, B. Civalleri, A. Meyer, P. Musto, A. Albunia, P. Rizzo, G. Guerra, *J. Phys. Chem. B*. 113, 5059 (2009).

70 A.A. Albunia, P. Musto, G. Guerra, *Polymer* 47, 234-42 (2006).

71 F.J. Torres, B. Civalleri, A. Meyer, P. Musto, A.R. Albunia, P. Rizzo, G. Guerra, *J. Phys. Chem. B*. 113, 5059-71 (2009).

72 M. C. Gupta, A. Gupta, J. Horwitz, D. Kliger, *Macromolecules* 15, 1372-76 (1982).

73 B. Wandelt, *Polymer* 32, 2707-11 (1991).

74 E. Grana, D. Katsigiaannopoulos, A.E. Karantzalis, M. Baikousi, A. Avgeropoulos *European Polymer Journal* 49, 1089-1097 (2013).

75 Guillet, J.Polymer Photophysics and Photochemistry, Cambridge University Press: Cambridge, Chapter 7 (1985).

76 P. Rizzo, T. Montefusco, G. Guerra, *J Amer Chem Soc*. 133, 9872-77 (2011).

77 A. Brizard, R. Oda, I. Hic, *Top. Curr. Chem.* 256, 167-218 (2005).

78 A. Buono, P. Rizzo, I. Immediata, and G. Guerra, *J. Am. Chem. Soc*. 129, 10992–10993 (2007).

79 P. Rizzo, E. Lepera, G. Guerra ACS submitted.

80 Y. Chatani, Y. Shimane, Y. Inoue, T. Inagaki, T. Ishioka, T. Ijitsu, T. Yukinari, *Polymer* 33, 488-92 (1993).

81 P. Rizzo, S. Della Guardia, G. Guerra, *Macromolecules* 37, 8043-49 (2004).

82 O. Tarallo, V. Petraccone, C. Daniel, G. Guerra, *Cryst. Eng. Commun*. 11, 2381-90 (2009).

83 C. Daniel, N. Galdi, T. Montefusco, G. Guerra, *Chem. Mater*. 19, 3302-308 (2007).

Photo-induced linear and circular birefringence in azo-polymers

3.1 Introduction

Rapid development of various modern systems for recording, transfer, processing, and display of data, visualization of images, as well as miniaturization of the optical devices requires, both solving numerous technological problems and creating new materials capable of providing rapid and reliable response to the control signals transmitted by electromagnetic fields, particularly by the light and laser actions. Among various inorganic and organic photoresponsive materials usually referred to as "smart or intelligent materials", the photochromic liquid crystalline (LC) polymers systems are of indubitable interest.[1-12] This class of polymers successfully combine the physico-chemical properties of macromolecular compounds (with their ability of forming films, fibers, elastomers) with the mesomorphic properties of low-molar-mass liquid crystals and photosensitivity of chromophores, covalently incorporated into the polymer chain as the side groups. The binary nature of photochromic LC polymers offers great advantages with respect to processing properties, photoactivity, stability of the stored information, and possible data recording on the thin polymer films. The presence of photochromic groups in the macromolecules of LC polymers or in the mixtures of dopants with polymers accounts for their sensitivity with respect to light or laser irradiation, induces certain photochemical transformations. The photochromic groups play the role of effective 'switchers' capable of sharply changing their configuration and conformation upon photoisomerization and other reactions. Their ability for self-organization and formation of various ordered supramolecular structures under the action of external fields[13] creates interest in the development of new materials with local properties controlled by optical methods. These materials could be used as new effective media for optical storage devices for electronics, electrooptics, and holography. [6,14-18]

Among photochromic LC polymers, azobenzene binary LC copolymers are the most common compounds.[19] They have been studied in detail, and their optical properties were reported in different works.[20-22] To get a better understanding of how the functionalities (chirality, azobenzene moities) affects the optical storage properties of the materials, we have performed a series of experiments measuring the intrinsic values of linear and circular birefringence of the

liquid crystal azo-polymers before the exposition at an incident pump beam and the time evolution of the photo-induced anisotropies during the irradiation.

3.2 Functionalized polymeric materials

In recent years, organic molecular materials have attracted considerable interest and continue to inspire new analyses and researches. The attention to these materials is primarily due to the possibility to design molecules with properties tailored for specific applications, that can give rise to intermolecular interactions with high added value. The macromolecular structure of high-molar-mass compounds provided by the presence of long and flexible chains is responsible for the principal features of such compounds, and in due time this direction constituted a new branch of science referred to as Polymer Science or Macromolecular Science.[19,23] The chain structure of both natural and synthetic polymers offers almost unlimited options in the molecular design when one macromolecule may contain numerous identical or different structural units (monomer units), and their arrangement presents the primary structure of high-molar-mass compounds. LC polymers show one specific feature: as a rule, they contain flexible and rigid (mesogenic) fragments shaped as rods or disks. Mesogenic groups are the fragments with a sufficient anisotropy in both attractive and repulsive forces in a molecule or macromolecule which provide the development of LC phase in both low-molar-mass and polymeric compounds. These fragments are connected to each other in different ways.[23]

Thus, the molecular structure of such polymers consists of fragments with different functionalities chemically linked to the main chain (*main-chain polymers*) or in side chains (*side-chain polymers*) via flexible aliphatic (or hydroxyaliphatic) spacers with a variable length. A potential synthesis of LC polymers constructed of macromolecules with different combinations of mesogenic and non-mesogenic fragments offers ample opportunities for the molecular design of new polymer LC compounds. On one hand, such compounds provide new and rather complex objects for scientific cognition where their synthesis and characterization

present an evident academic interest. On the other hand, there exists the problem concerning their practical application and potential areas of utilization.

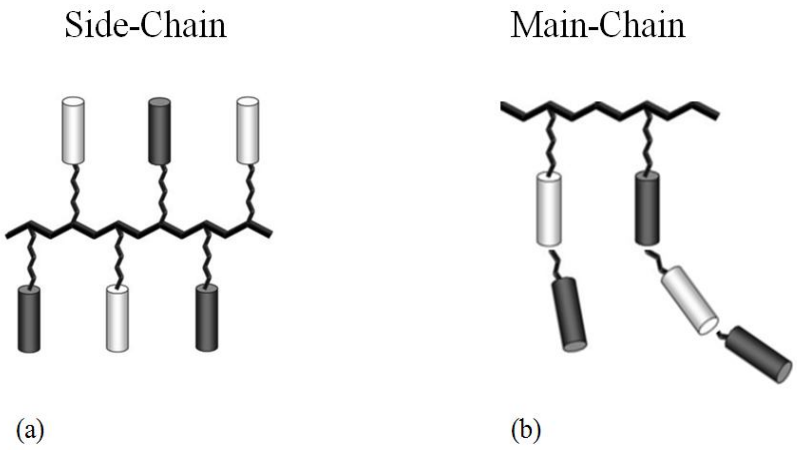

Fig. 3.1 Schematic representations of macromolecules with two functionalities linked in the side chain (a) and in the main chain (b) of the polymer.

The pronounced ability of these compounds for self-organization and formation of various ordered supramolecular structures present a considerable interest from the standpoint the development of new "smart" materials with optically controlled supramolecular structure and physical properties (optical data storage, display technology, holography,etc.).[22] A key rule to determining the optical properties of these polymer belongs to the photoisomerizable side group (azobenzene) which play the role of effective "switchers" capable of significantly changing their configuration and conformation under the polarized light action. For instance, the photochromic groups of azobenzene containing LC copolymers may undergo a reversible *trans–cis* (*E–Z*) isomerization due to the light irradiation with an appropriate wavelength. This leads to the photochemical configurational changes of azobenzene groups which are transformed from rigid-rode (mesogenic) shape to a nonmesogenic bent shape. As a result the supramolecular structure and the optical properties of polymer films are dramatically changed the photochromic and (together with them) nematogenic groups are oriented so that their long

axes would be perpendicular to the electric vector direction of the polarized light. In other words, the light irradiation effectively selects molecules by orientating them in a preset direction that causes the appearance of a considerable photoinduced birefringence ($\Delta n \sim 0.25–0.30$) due to a cooperative character of the orientational process. The appearance of induced birefringence in the films of such polymers under the action of polarized light and possible applications of such materials for data recording have been studied in detail.

3.3 Experimental Part I: Intrinsic and induced anisotropy analysis.

In anisotropic materials the velocity of light propagation depends on the propagation direction. The *anisotropy* is connected with the structure of the material. In some materials illumination with polarized light causes selective destruction of absorbing molecules or centers, reordering of these absorbing centers, or some other changes depending on light polarization. This results in polarization-dependent changes in the absorption coefficient or/and in the refractive index of the material, that is, in optical anisotropy. The dependence of the absorbance on light polarization is called *dichroism* and the dependence of the refractive index on light polarization is called *birefringence*. Birefringence (double refraction) is an important property of optically anisotropic media, which can be classified as either *linear* or *circular*. In the former case, the birefringence effects are determined by changes in the principal axis angle and phase retardance of the optical medium as the result of variations in the externally-applied stress. In the latter case, the birefringence effects are the result of a particular property of some optical media known as “optical activity”, which causes right-circularly polarized light to be transmitted at a different velocity through the medium than left-circularly polarized light.

Methods to accurately determine optical properties of optoelectric materials or bio-sample make the promising applications in the future devices for inspection and therapeutic or

diagnostic detection. As a result, the literature contains many proposals for measuring the fundamental optical properties of anisotropic materials including linear and circular dicroism (LD, CD) linear birefringence (LB)[24,25] and circular birefringence (CB).[26,27] As shown in Kaminsky et al.[28-30] papers, they constructed a single microscope for measuring and separating the contributions of LB, LD, CB and CD through modifications of the optical path and mechanically modulated linearly and circularly polarized light input. They employed the Jones calculus for extract the characteristic of optical samples. They used different tools for each optical properties, therefore, the measured results from the sample may be easily contaminated by other irrelated properties if the purification process is not conducted. Chenault and Chipman[31-34] proposed a technique to measure LD and LB spectra of infrared materials in transmission. The intensity modulation that resulted from the rotation of the sample was fourier analyzed, and the linear dichroism and linear birefringence of the sample were calculated from the Fourier series coefficients for each wavelength. However, in extracting the sample parameters, an assumption was made that the principal birefringence and diattenuation axes were aligned. Chen *et al.*[35] also proposed a technique for measuring the LB and LD of an optical sample using a polarimeter based on the Mueller matrix formulation and the Stokes parameters. Also, Lo et al[36] proposed a technique for measuring the effective LB, LD and CB of an optical fiber based on the similar method. Unlike the existing methods introduced above, the LB and LD parameters were decoupled within the analytical model. However, certain anisotropic materials (e.g. liquid crystal polymers) have not only the LB and LD, but also CB effects are present at the same time, for example in many liquid crystal displays. Therefore, in designing, manufacturing and characterizing the optical performance of such applications, a requirement exists for methods capable of obtaining simultaneous measurements of both the linear and the circular birefringence properties.

In the proposed approach, the cycloidal grating, described in chapter 1, is used to extract concurrently LB and CB values of the Mueller matrix of the sample of interest by means of change of the polarization state of a light.

3.3.1 Theoretical model

The present study proposes a method based on the Mueller matrix formulation and the Stokes parameters for determining the effective optical parameters of an anisotropic material. Before performing polarization-holographic measurements, it may be worthwhile to determine the birefringence that can be induced in the material and its stability in time. Thus, we propose an analytical method for determining the effective LB and CB properties of an anisotropic optical material utilizing the cycloidal OAG described in chapter 1. In this method, the linear birefringence properties of the composite sample are extracted from the output Stokes vectors corresponding to three different input polarization states, namely one linear polarization state and two circular polarization state (right- and left- handed).

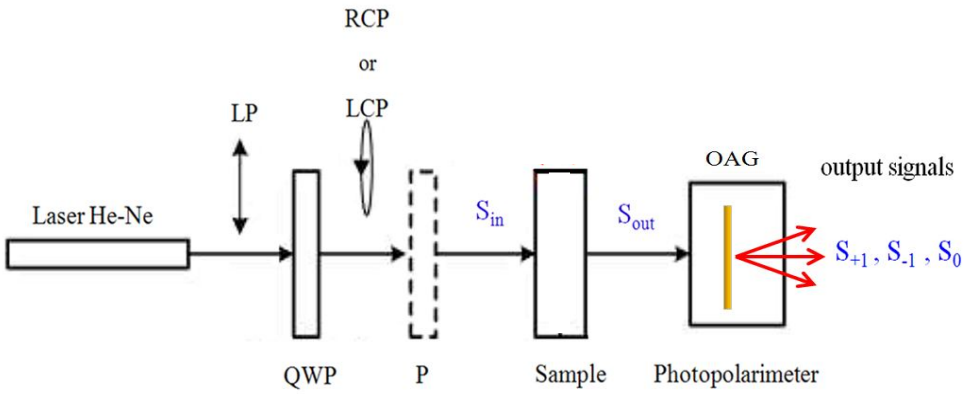

Fig. 3.2 Schematic diagram of model used to characterize LB and CB of an anisotropic material.

Figure 3.2 presents a scheme of the setup proposed in this study for characterizing the LB and CB properties of an optically anisotropic material. As shown in figure 3.2 , P is a polarizer and QWP is a quarter-wave plate, which are used to produce various linear polarization lights and right-/ left- handed circular polarization lights (R- or L- CP); S_{in} and S_{out} are input and output Stokes vector, respectively. The state of polarization of a light beam can be completely

described by the Stokes vector $S = \{S_0 , S_1, S_2 , S_3\}^T$, in which the four components are given by[37]:

$$S_0 = a_x^2 + a_y^2 = I_x + I_y$$

$$S_1 = 2a_x a_y \cos\theta = I_{45^\circ} + I_{-45^\circ}$$

$$S_2 = 2a_x a_y \sin\theta = I_{rcp} + I_{lcp}$$

$$S_3 = a_x^2 - a_y^2 = I_x - I_y$$

where S_0 is the total light intensity; S_1 is the intensity difference between +45° and −45° polarized components; and S_2 is the intensity difference between right- and left-circularly polarized components; S_3 is the intensity difference between horizontally and vertically polarized components. Any optical component which changes the polarization state of a light beam can be modeled by a 4 x 4 Mueller matrix.

As shown by Troxell and Scheraga[38], the Mueller matrix of interest can be expressed in a very convenient way:

$$\hat{M} = e^{-Ae}(I - \hat{F} + \frac{1}{2}\hat{F}^2 - \frac{1}{3!}\hat{F}^3 + \frac{1}{4!}\hat{F}^4 \ldots) \quad (3.1)$$

in which, Ae is the mean absorbance and I the identity matrix. In this study, we assumed that the samples have both linear and circular birefringence with its optical axis parallel to the x axis.[39] Thus, F can be expressed as follows:

$$\hat{F} = \begin{bmatrix} 0 & 0 & 0 & 0 \\ 0 & 0 & LB & CB \\ 0 & -LB & 0 & 0 \\ 0 & CB & 0 & 0 \end{bmatrix} \quad (3.2)$$

The parameters LB and CB reported in Eq. 3.2 are defined according to Table II in Ref. 38 as:

$$LB = \frac{2\pi(n_x - n_y)l}{\lambda_0} = \frac{2\pi\Delta n_{lb} l}{\lambda_0} \tag{3.3}$$

and

$$CB = \frac{2\pi(n_- - n_+)l}{\lambda_0} = \frac{2\pi\Delta n_{cb} l}{\lambda_0} \tag{3.4}$$

where n stands for refractive index, l for pathlength through the medium, λ_0 for the vacuum wavelength of light. Subscripts specify the polarization of light as x, y, circular right (+), or left (−). The Mueller matrix $\hat{M}$ for a linear and circular birefringent material can be obtained easily from a simple computation of Eq. (3.1)

$$\hat{M} = e^{-Ae}\begin{bmatrix} 1 & 0 & 0 & 0 \\ 0 & 1-\frac{1}{2}(CB^2+LB^2) & -LB+\frac{1}{6}(CB^2LB+LB^3) & -CB+\frac{1}{6}(CBLB^2+CB^3) \\ 0 & LB-\frac{1}{6}(CB^2LB+LB^3) & 1-\frac{1}{2}LB^2 & 1-\frac{1}{2}CBLB \\ 0 & CB-\frac{1}{6}(CBLB^2+CB^3) & -\frac{1}{2}CBLB & 1-\frac{1}{2}CB^2 \end{bmatrix} \tag{3.5}$$

The inner product of this Mueller matrix $\hat{M}$ and the Stokes vector representing the polarization state of the incident light yields a Stokes vector S which describes the polarization state of the light exiting the optical sample. According to the Stokes-Mueller formulation, the Stokes vector of the output light can be derived as follows

$$S_{out} = \hat{M} \cdot S_{in} \tag{3.6}$$

For an incident beam right circularly polarized (RCP)

$$S_{in,RCP} = \begin{pmatrix} 1 \\ 0 \\ 1 \\ 0 \end{pmatrix}$$

the output Stokes vector is

$$S_{out} = \begin{pmatrix} 1 \\ -LB + \frac{1}{6}(CB^2LB + LB^3) \\ 1 - \frac{1}{2}LB^2 \\ -\frac{1}{2}CBLB \end{pmatrix} \tag{3.7}$$

The S_{out} beam impinges onto the cycloidal OAG, we obtain three outgoing beams. Using the Mueller matrices of the ±1 diffracted beams of an OAG, reported in[40]

$$T_{+1} = \frac{sin^2\Delta\phi}{2}\begin{pmatrix} 1 & 0 & +1 & 0 \\ 0 & 0 & 0 & 0 \\ -1 & 0 & -1 & 0 \\ 0 & 0 & 0 & 0 \end{pmatrix}, \quad T_{-1} = \frac{sin^2\Delta\phi}{2}\begin{pmatrix} 1 & 0 & -1 & 0 \\ 0 & 0 & 0 & 0 \\ +1 & 0 & -1 & 0 \\ 0 & 0 & 0 & 0 \end{pmatrix} \tag{3.8}$$

and according to the operating diagram reported in figure 3.2, the Stokes vectors of the ±1 orders, when a S_{out} light beam, which contains information about the anisotropy of the material, impinges on the OAG are given by

$$S_{c_{+1}} = 2|b^2| \begin{pmatrix} 1+1-\frac{1}{2}LB^2 \\ 0 \\ -1-1+\frac{1}{2}LB^2 \\ 0 \end{pmatrix}, \qquad S_{c_{-1}} = 2|b^2| \begin{pmatrix} 1-1+\frac{1}{2}LB^2 \\ 0 \\ 1-1+\frac{1}{2}LB^2 \\ 0 \end{pmatrix} \tag{3.9}$$

And the intensity of the ±1 –orders of diffraction are

$$Ic_{+1} = 2|b^2|(1+1-\tfrac{1}{2}LB^2) \tag{3.10}$$

$$Ic_{-1} = 2|b^2|(1-1+\tfrac{1}{2}LB^2) \tag{3.11}$$

From these relations is possible to obtain LB

$$LB = \sqrt{\frac{4Ic_{-1}}{Ic_{+1}+Ic_{-1}}} \tag{3.12}$$

Instead, considering an left circular polarized (LCP)

$$LB = \sqrt{\frac{4Ic_{+1}}{Ic_{-1}+Ic_{+1}}} \tag{3.13}$$

According to Eqs. (3.10) and (3.11) linear birefringence of a anisotropic optical material can be estimated using a circular polarization beam.

In order to derive the circular birefringence we must consider a linear polarized S incident beam:

$$S_{in,s} = \begin{pmatrix} 1 \\ 0 \\ 0 \\ -1 \end{pmatrix}$$

we obtain

$$S_{out} = \begin{pmatrix} 1 \\ CB - \frac{1}{6}(CBLB^2 + CB^3) \\ \frac{1}{2}CBLB \\ -1 + \frac{1}{2}CB^2 \end{pmatrix} \quad (3.14)$$

As seen before, we obtain the Stokes vectors of the ±1 –orders of diffraction in output from the cycloidal OAG:

$$S_{S_{+1}} = 2|b^2| \begin{pmatrix} 1 + \frac{1}{2}CBLB \\ 0 \\ -1 - \frac{1}{2}CBLB \\ 0 \end{pmatrix}, \; S_{S_{-1}} = 2|b^2| \begin{pmatrix} 1 - \frac{1}{2}CBLB \\ 0 \\ 1 - \frac{1}{2}CBLB \\ 0 \end{pmatrix} \quad (3.15)$$

Considering the Stokes vector of the ±1 orders reported in Eq, (3.13) is possible to calculate their intensities

$$Is_{+1} = 2|b^2|(1 + \frac{1}{2}CBLB) \quad (3.16)$$

$$Is_{-1} = 2|b^2|(1 - \frac{1}{2}CBLB) \quad (3.17)$$

thus CB is given by

$$CB = \frac{2(Is_{+1} - Is_{-1})}{Is_{+1} + Is_{-1}} / LB \quad (3.18)$$

3.3.2 Materials:
Chiral/achiral liquid crystal azo-polymers.

The organic materials studied in this proposal are polymers bearing two functional groups, *photosensitive azoaromatic groups*, directly linked to the side chain, and *chiral groups*, dispersed in the polymer matrix. They therefore possess the two functionalities that are the basis for optical storage based on induced modulation of the refractive index and chiro-optical switch. The photo-induced anisotropy obtained by irradiating the molecular materials by single beam with different polarization states will be studied, in order to analyze and characterize the formation of structures connected to the birth of linear and circular birefringence.

In particular, the selected photochromic polymers may be conditionally classified into two groups: achiral and chiral systems. The achiral one used to perform the investigation are *nematic liquid crystal azo-containing polymers*, in particular polymethacrylic copolymers that

have in the side-chains oxycyano-azobenzene fragments (photosensitive achiral azobenzene groups) and cooperative mesogenic units whose chemical formula is reported in figure 3.3.

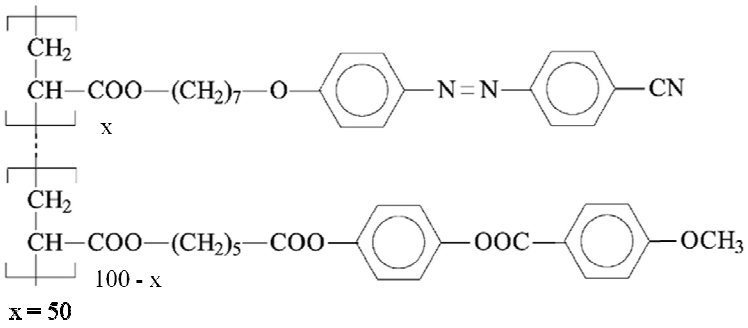

Fig. 3.3 Achiral polymeric structure.

We also used a mixtures of this nematic liquid cristal azo-polymer with low-molar-mass of chiral-photochromic dopants having a right-handed conformer, see figure 3.4 .

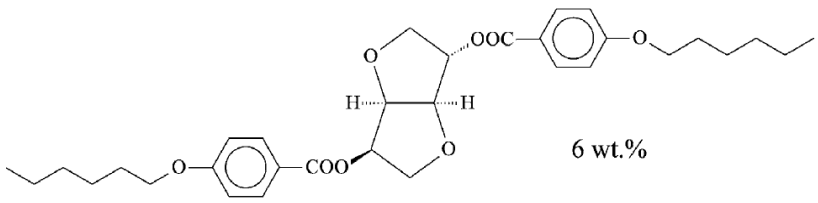

Fig. 3.4 Chiral low-molar-mass dopant molecular structure.

In figure 3.5 is reported the absorption spectrum of the two polymers, in which the probe beam wavelength $\lambda = 633$ nm is highlighted.

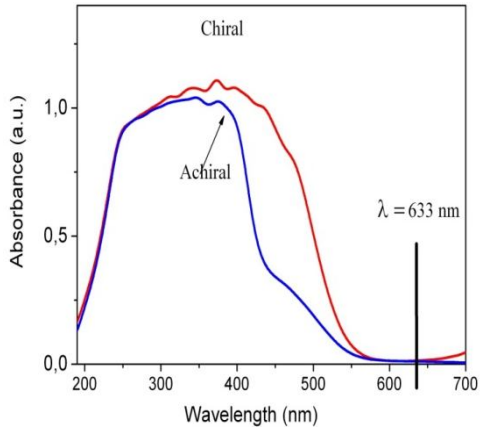

Fig. 3.5 Absorption spectrum of achiral and chiral liquid crystal azo-polymer.

The polymer samples was prepared in the form of a 10 μm thick film placed between two ITO glass plates, prepared by melting the polymer above the *Tg* (119 °C) and cooling it down to room temperature. The indium tin oxide glasses are coated with polyimide (PI) rubbed layers in order to provide planar nematic alignment.

3.3.3 Experiment and Results

The following experimental setup has been employed for the determination of optical anisotropy. Two lasers, one serving as a pump laser (a Ar^+ laser at $\lambda = 488\,nm$) and the other in the red as a probe laser, are employed. The induced anisotropy at the red laser wavelength (a He-Ne laser at 633 nm) is detected, this wavelength is far from the absorption band of the

photochromic azo-groups. In the set-up shown in figure 3.7, the He-Ne beam is linearly or circularly polarized with a polarizer and a quarter-wave plate, respectively. After passing through the sample the output beam impinges on a cycloidal OAG and thus the beam is split into two circular polarized components. The intensities of these two beams are measured by two photodiodes.

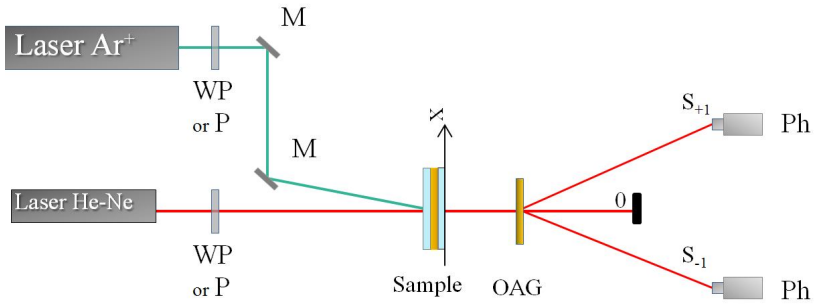

Fig.3.7 Experimental set-up used to measure optical anisotropies: WP wave plate; P polarizer; M mirror; sample; OAG grating; S_{+1} and S_{-1} diffracted beams; Ph photodiode.

The first experiment has been performed on the chiral LC polymer using only the He-Ne laser, this means that only the intrinsic birefringence Δn^0_{lb} and Δn^0_{cb} evaluation were carried out. Following the operation scheme reported in figure 3.2 and considering the Eqs.(3.3) and (3.12), when an incident RCP or LCP probe beam impinges on the chiral polymer cell we obtain $\Delta n^0_{lb} = 0{,}0031$. We noticed that there are no differences between the LCP or RCP probe beam, this means that we can use only one during the analysis.

Furthermore, using the relation reported in Eq.(3.4) and (3.18), when the probe beam is linear S polarized we extract $\Delta n^0_{cb} = -0{,}0035$.

To measure the photo-induced linear and circular birefringence we exposed the sample for 60s to an incident Ar^+ pump beam linearly S and circularly polarized with intensity (I = 10 mW/cm^2).

The plots displayed in figure 3.8 represent the signal of the ±1st order of diffraction collected on the photodiodes when the pump is linearly S polarized and the probe is linearly S and circularly polarized.

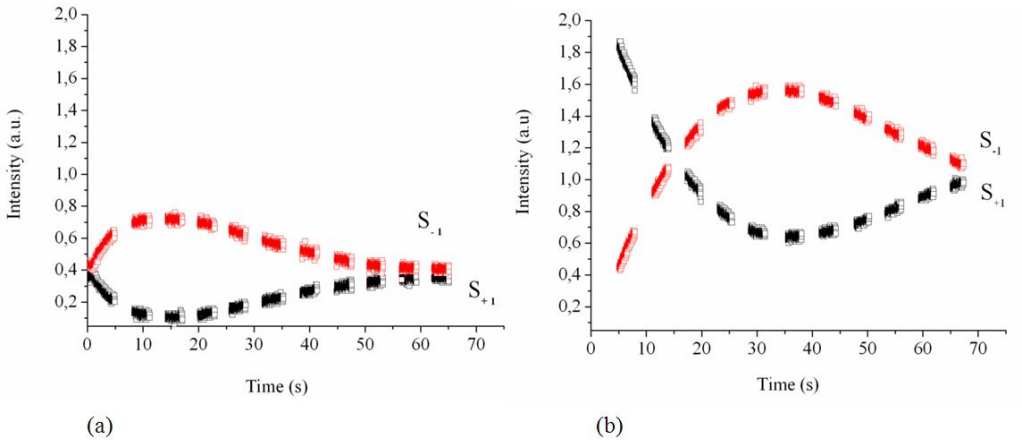

Fig. 3.8 Temporal behavior of the S_{+1} and S_{-1} output signal when the impinging pump beam is linearly S polarized: the probe beam is linearly (a) and circularly polarized (b).

Using the relation reported in Eq. (3.12) and the experimental data obtained when the probe is circularly polarized, figure 3.8(b) is possible to obtain the temporal evolution of the induced linear birefringence Δn_{lb}^{ind}, see figure 3.9(a). Considering the Eq. (3.18) and the data obtained when the probe is S polarized, figure 3.8 we can also obtain the evaluation of induced circular birefringence Δn_{cb}^{ind} in time, see figure 3.9(b).

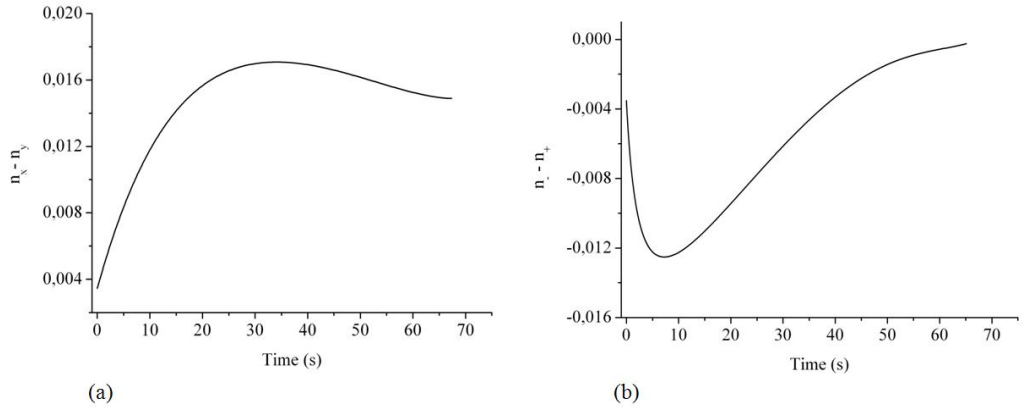

Fig. 3.9 Time dependence of laser-induced birefringence Δn_{lb}^{ind} (a) and Δn_{cb}^{ind} (b) for an incident S polarized pump beam.

In figure 3.10 we report the results when the pump beam is circularly RCP polarized and the probe beam is linearly S and circularly polarized.

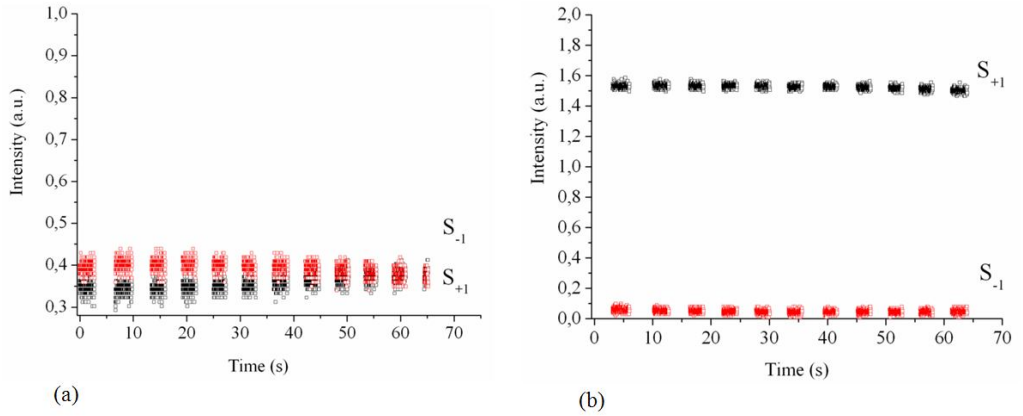

Fig. 3.10 Temporal behavior of the S_{+1} and S_{-1} output signal when the impinging pump beam is RCP: the probe beam is linearly (a) and circularly polarized (b).

Thus, the extracted values of Δn_{lb}^{ind} and Δn_{cb}^{ind} are reported in figure 3.11.

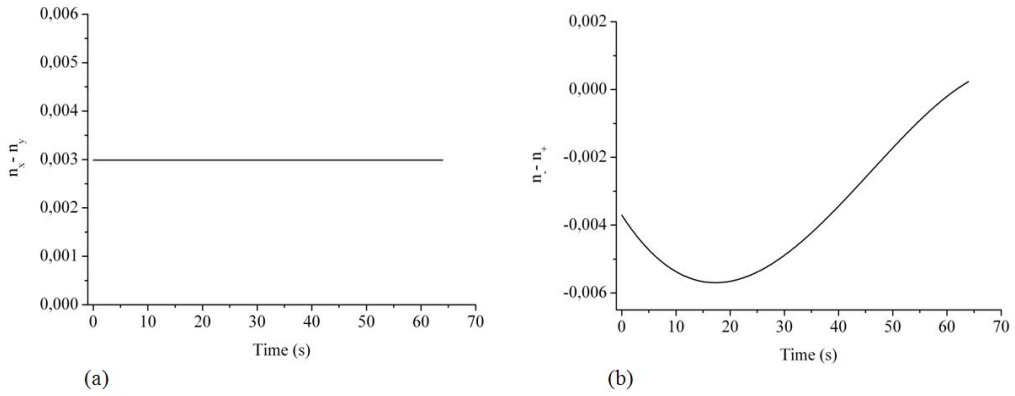

Fig. 3.11 Time dependence of laser-induced birefringence Δn_{lb}^{ind} (a) and Δn_{cb}^{ind}(b) for an incident RCP polarized pump beam.

Finally, in figure 3.12 we reported the results when the pump beam is circularly LCP polarized and the probe beam is linearly S and circularly polarized.

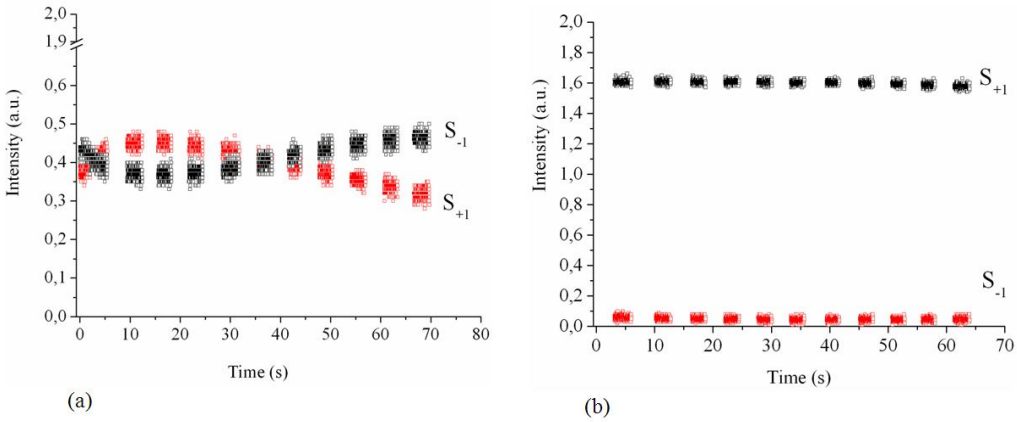

Fig. 3.12 Temporal behavior of the S_{+1} and S_{-1} output signal when the impinging pump beam is LCP: the probe beam is linearly (a) and circularly polarized (b).

Using the data reported in figure 3.12 we obtain Δn_{lb}^{ind} and Δn_{cb}^{ind}

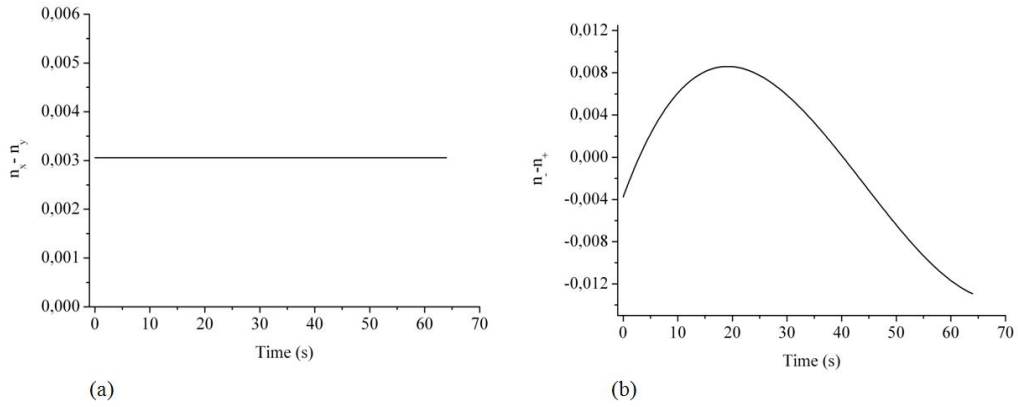

Fig. 3.13 Time dependence of laser-induced birefringence Δn_{lb}^{ind} (a) and Δn_{cb}^{ind} (b) for an incident LCP polarized pump beam.

As shown by the results, the photochromic groups and mesogenic fragments orient so that their long axes are perpendicular to the electric field vector direction of the laser beam. In other words, the laser irradiation effectively selects molecules by orienting them in a preset direction. This photo-stimulated orientation, takes place in solid polymer films and leads to the appearance of induced birefringence Δn_{lb}^{ind} and Δn_{cb}^{ind}, changing the optical properties of irradiated films. As expected, the analysis of data on the optical properties of chiral LC polymer films before and after laser irradiation showed that the photoinduced linear birefringence appears and reached the value $2 \cdot 10^{-2}$. For linear S and RCP incident pump beam, the photo-induced circular birefringence reaches the zero value, obtaining in this way a racemic polymer. The photoinduced circular birefringence appears only for LCP and reached $1{,}2 \cdot 10^{-2}$. We apply the same analysis at the nematic liquid crystal polymer. As seen before, the first experiment have been performed using only the He-Ne laser and following the operation scheme reported in figure 3.2, we obtain the intrinsic birefringence values of the achiral polymer $\Delta n_{lb}^{0} = 0{,}0012$ and $\Delta n_{cb}^{0} = 0$, respectively. The plots displayed in figure 3.14 represent the signal of the $\pm 1^{st}$ order of diffraction collected on the photodiodes when the pump is linearly S polarized and the probe is linearly S and circularly polarized.

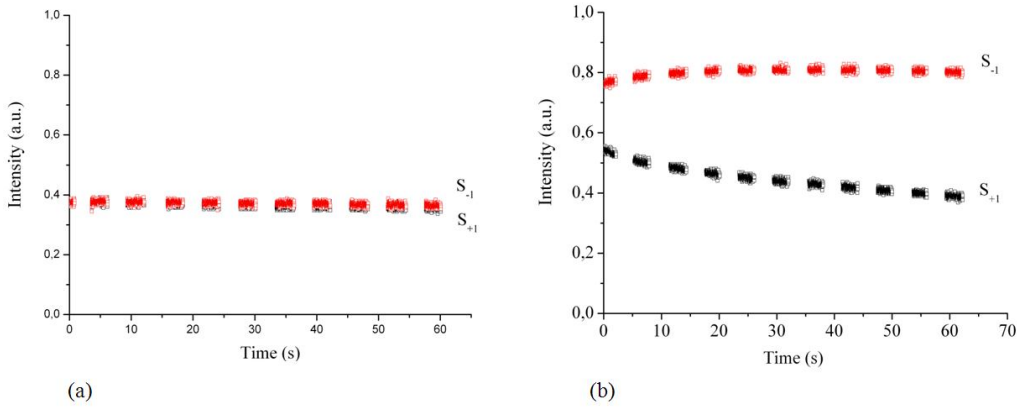

Fig. 3.14 Temporal behavior of the S_{+1} and S_{-1} output signal when the impinging pump beam is linearly S polarized: the probe beam is linearly (a) and circularly polarized (b).

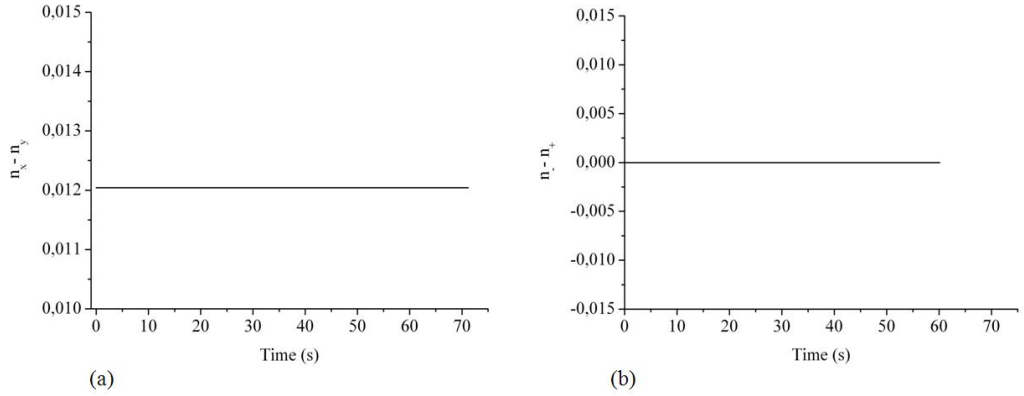

Fig. 3.15 Time dependence of laser-induced birefringence Δn_{lb}^{ind} (a) and Δn_{cb}^{ind} (b) for a incident S polarized pump beam.

In figure 3.16 we report the results when the pump beam is circularly RCP polarized and the probe beam is linearly S and circularly polarized.

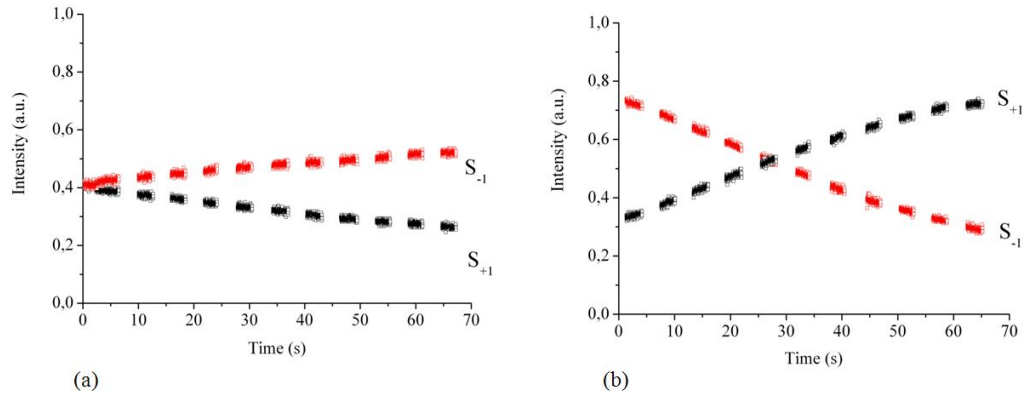

Fig. 3.16 Temporal behavior of the S_{+1} and S_{-1} output signal when the impinging pump beam is linearly RCP: the probe beam is linearly (a) and circularly polarized (b).

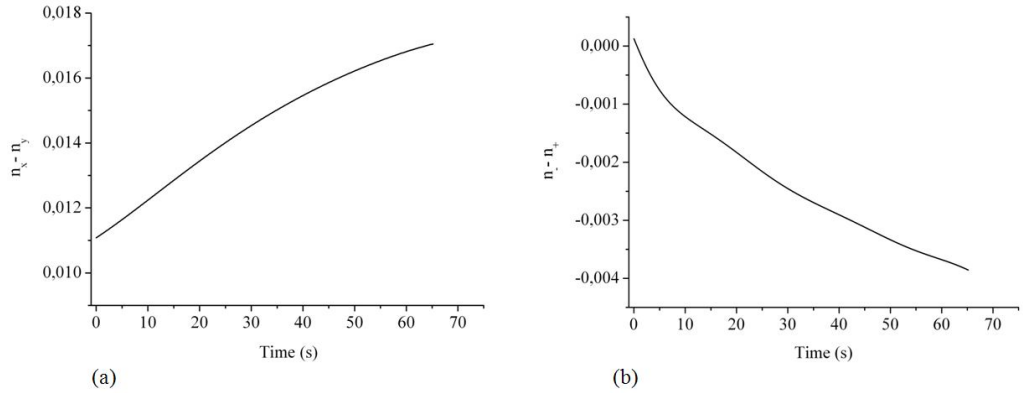

Fig. 3.17 Time dependence of laser-induced birefringence Δn_{lb}^{ind} (a) and Δn_{cb}^{ind} (b) for a incident RCP polarized pump beam.

Finally, in figure 3.18 we reported the results when the pump beam is circularly LCP polarized and the probe beam is linearly S and circularly polarized.

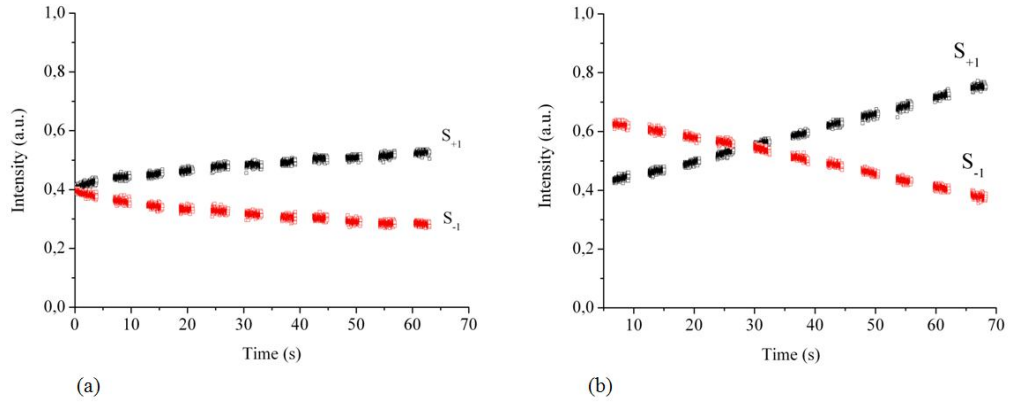

Fig. 3.18 Temporal behavior of the S_{+1} and S_{-1} output signal when the impinging pump beam is linearly LCP polarized: the probe beam is linearly (a) and circularly polarized (b).

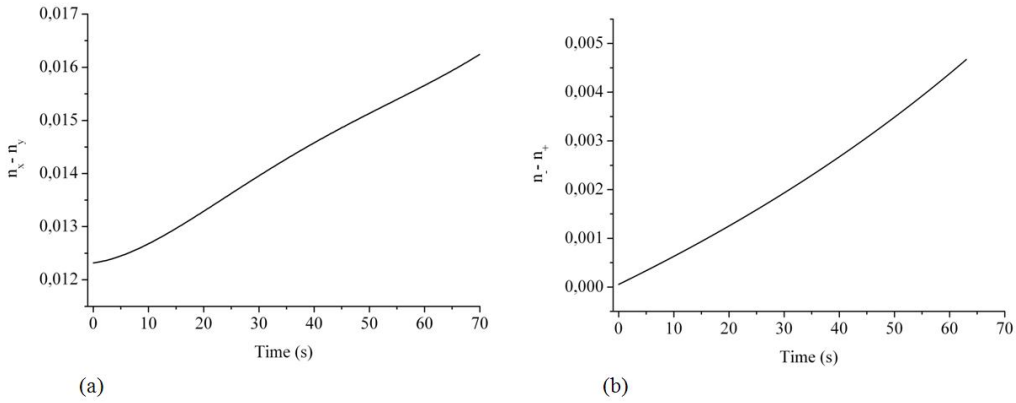

Fig. 3.19 Time dependence of laser-induced birefringence Δn_{lb}^{ind} (a) and Δn_{cb}^{ind} (b) for a incident LCP polarized pump beam.

The analysis of data on the optical properties of achiral LC polymer films before and after laser irradiation showed that upon linear S irradiation the photoinduced birefringence increases (Δn_{lb}^{ind}) ,while after circular irradiation appears Δn_{cb}^{ind}. As seen previously also in this case, the photoinduced linear birefringence is about $2 \cdot 10^{-2}$. Furthermore, the photoinduced circular

birefringence depends of the handedness of the incident circular polarization. For a RCP beam the photo-induced circular birefringence reached negative values, while for a LCP the values are positive. This is primarily due to a supramolecular orientation of the chormophores which shows a complexity of the phenomenon that requires a more detailed investigation.

3.4 Conclusions and perspectives

This study has proposed an analytical technique based on the Mueller matrix method and the Stokes parameters for extracting LB and CB properties of anisotropic optical materials. This method make possible the real time measurement of the linear and circular birefringence properties of a material during the irradiation an optical sample. Although only two different input polarization lights, namely one circular and one linear polarization lights are enough to obtaining all the elements. With this method we have investigated two liquid crystal azo-polymers: chiral and achiral. For both polymers the photo-induced linear birefringence are comparable, in contrast to that observed for the photo-induced circular birefringence. In particular, in the chiral azopolymer the induced linear and circular birefringence can be ascribed to an induced supramolecular organization. The extracted values of birefringence are compatible with the values generally founded by these molecules. For the achiral azo-polymer, the photo-induced circular birefringence depends of the handedness of the induced polarization. The results shows that we reached an amplification of circular birefringence tree times larger than that the initial value, however, the phenomena that give rise to this effect are due to a supramolecular orientation of chromophores and requires further analysis. In future work, the proposed method can be extended to extract other parameters of polymeric materials.

References

1. PJ. Flory Principles of polymer chemistry. Ithaca, NY: Cornell University Press (1953).
2. HG. Elias An introduction to polymer science. Weinheim: VCH (1997).
3. NA. Plate, VP. Shibaev Plenum Press, New York (1987).
4. M. Gordon, N. Plate, editors Advances in polymer science, vol. I–III. Berlin: Springer (1984).
5. A. Blumsteim, editor. Polymeric liquid crystals. New York: Plenum Press (1985).
6. C. McArdle, editor. Side chain liquid crystal polymers. London: Blackie (1989).
7. A. Ciferri, editor. Liquid crystallinity in polymers: principles and fundamental properties. Berlin: VCH (1991).
8. AM. Donald, A. Windle Liquid crystalline polymers. Cambridge: Cambridge University Press (1992).
9. VP. Shibaev, L. Lam, editors. Liquid crystalline and mesomorphic polymers. New York: Springer (1994).
10. AA. Collyer, editor. Liquid crystal polymers: from structure to applications. London: Elsevier (1992).
11. D. Acierno, AA. Collyer, editors. Pheology and processing of liquid crystal polymers. London: Chapman & Hall (1996).
12. Plate N, editor. Liquid crystal polymers. New York: Plenum Press (1993).
13. U. Ruiz, P. Pagliusi, C. Provenzano, V.P. Shibaev, and G. Cipparrone. *Adv. Funct. Mater. 22*, 2964–2970 (2012)
14. V. Shibaev, editor. Polymers as electrooptical and photooptical active media. Heidelberg: Springer (1996).
15. RG. Weiss Photochemical processes in liquid crystals. In: Ramamurthy V, editor. Photochemistry in organized and constrained media. New York: VCH (1991).
16. S. Elston, R. Sambles, editors. The optics of thermotropic liquid crystals. London: Taylor & Francis (1998).

17. J.C. Crano, RJ. Guglielmetti, editors. Organic photochromic and thermochromic compounds, vol. 1. New York: Kluwer Academic Publishers/Plenum Press (1998).

18. C. McArdle, editor. Applied photochromic polymer systems. London: Blackie (1992).

19. V.P. Shibaev, A. Bobrovsky, N. Boiko. *Prog. Polym. Sci*. 28,729–836 (2003).

20. V.P. Shibaev, S.V. Belyaev *Polym.Sci.USSR* 42:2384 (1990).

21. V.P. Shibaev, S.G. Kostromin, S.A. Ivanov *Polym Sci A* 39:36 (1997).

22. U. Ruiz, C. Provenzano, P. Pagliusi and G. Cipparrone *Opt. Lett.* (2012).

23. G. F. Smith, *Constitutive equations for anisotropic and isotropic materials*, (North-Holland, 1994).

24. B. Wang and T. C. Oakberg, *Rev. Sci. Instrum.* 70, 3847–3854 (1999).

25. Y. L. Lo, J. F. Lin, and S. Y. Lee, *Appl. Opt.* 43, 2013–2022 (2004).

26. B. D. Cameron and G. L. Cóte, "Noninvasive glucose sensing utilizing a digital closed-loop polarimetric approach," IEEE Trans. Biomed. Eng.44,1221–1227 (1997).

27. Y. L. Lo and T. C. Yu, *Opt. Commun.* 259, 40–48 (2006).

28. W. Kaminsky, K. Claborn, and B. Kahr, *Chem. Soc. Rev.* 33, 514–525 (2004).

29. W. Kaminsky et al., *J. Phys. Chem.* 107, 2800–2807 (2003).

30. K. Claborn et al., *J. Am. Chem. Soc*. 125, 14825–14831 (2003).

31. D. B. Chenault and R. A. Chipman, *Appl. Opt*. 32, 3513–3519 (1993).

32. D. B. Chenault and R. A. Chipman, *Appl. Opt*. 32, 4223–4227 (1993).

33. D. B. Chenault, R. A. Chipman, and S. Y. Lu, *Appl. Opt*. 33, 7382–7389 (1994).

34. E. A. Sornsin and R. A. Chipman, *Proc. SPIE* 3121, 156–160 (1997).

35. P. C. Chenet al., *Opt. Exp*. 17, 15860–15884 (2009).

36. Y. L. Lo, T. T. H. Pham, and P. C. Chen, *Opt. Exp*. 18, 9133– 9150 (2010).

37. H.P. Jensen, J.A. Schellman and T. Troxell. *Appl. Spectr.* 32(2)

38. T.C. Troxell and H.A. Scheraga, *Macromolecules* 4, 519 (1971).

39. Y. Shindo, M. Nakagawa and Y. Ohmi, 39,860-868 (1985)

40. C. Provenzano, P. Pagliusi, A. Mazzulla, G. Cipparrone, *Opt. Lett.* 35,1822-1824 (2010)

Summary

The main object of this research was to control through external stimuli or enantiomeric interactions the macroscopic structures, functions and properties of two different class of polymers. During our investigation, we have found a number of interesting results that can be summarized as follows.

- We obtained highly efficient liquid crystal based polarization gratings exploiting polarization holographic technique recorded on a photosensitive azo-dye layer. This patterned substrate in contact with a thin film of liquid crystal provide a periodic alignment to liquid crystalline materials (LC). The resulting diffractive element is characterized by a very high efficiency and peculiar diffractive properties useful to develop polarimetric devices. Using a conventional polarization holographic method and photo-anisotropic aligning material, two different approaches have been investigated.
- Low molar mass nematic LC sandwiched between holograms substrates and photo-reactive mesogenic monomers spincasted on top of the aligning substrate have been studied experimentally and the results interpreted with a simple model.

  The LC gratings confined between substrates have demonstrated excellent optical quality, like ideal cycloidal OAG. The RM gratings are less prone to optical degradation, thus exhibiting higher optical and mechanical stability, but are affected by detrimental periodic undulation of the free surface.
- Some examples of polarimetric applications of the cycloidal OAG have been reported: a photopolarimeter able to measure simultaneously and in real time the Stokes parameters of an electromagnetic wave and a CD spectrograph. The spectro-photopolarimetric systems proposed in this work has an extreme simplicity of use, are compact devices because free of modulating or moving parts, and are easy to calibrate.
- The same approach to generate the cycloidal OAG has been adopted to create microlens arrays (MAs). The all optical method is based on the coupling of liquid

crystal cell having photosensitive aligning substrates and a spatial light modulator (SLM)-assisted polarization holographic technique. The adopted approach allows us to design the gradient index refraction (GRIN) modulation of a planar liquid crystal cell in order to create different MA configurations. The flexible and easy technique to fabricate MAs shows two remarkable advantages respect to other techniques: short time and low intensity recording. Two MA configurations characterized by spherical and cylindrical microlenses with different focal lengths have been reported and characterized. The controllable linear birefringence and the transparency in the visible range of the liquid crystal allow maximize the efficiency near to 100% in a wide range of wavelengths, by a low applied voltage.

- We studied the induction of chirality on melt extruded s-PS films of different thickness as induced by co-crystallization with a non-racemic guest (R or S carvone) and retained after exchange of the non-racemic guest with achiral chromophores (azulene and 4-nitro-aniline). The intense induced circular dichroism (CD) and vibrational CD (VCD) phenomena, both for the polymer host and for its achiral chromophore guests, are markedly increased with film thickness reduction (4 μm).
- The preparation of chiral films of few microns has also allowed to identify additional intense polystyrene CD peaks at 262, 265 and 269 nm.
- VCD analysis of s-PS films in which non-racemic molecules are included as guest, indicate that the intrinsic (molecular) contribution to the circular dichroism is negligible with respect the extrinsic (supramolecular) contribution of which exhibit supramolecular chirality.
- CD spectra of s-PS films including the co-crystalline form with NA confirm that the chiral optical response of achiral guest chromophores occurs when such molecules are included as guest in the nanoporous crystalline phase, rather than simply dissolved in the amorphous phase.
- The use of a low cost commercially available robust thermoplastic polymer, which can be processed by standard industrial processes (like melt extrusion), followed by simple liquid bath treatments, and the possibility to get chiral optical responses at

wavelengths of achiral chromophores suggest that s-PS-based chiral optical materials and devices can be easily designed and produced.

- We have reported an experimental and theoretical method based on the Mueller matrix formulation and the Stokes parameters for determining the optical properties of chiral and achiral liquid crystal azo-polymers. This method makes possible the concurrent measurement of the linear and circular birefringence. polarization grating (cycloidal OAG) we determined the effective and the photo-induced optical anisotropies (LB and CB).

List of publications:

1. P. Pagliusi, E. Lepera, C. Provenzano, A. Mazzulla and G. Cipparrone "Polarization gratings allow for real-time and artifact-free circular dichroism measurements". *Proc. SPIE*, 8069, 806910 (2011)

2. E. Lepera, C. Provenzano, P. Pagliusi, G. Cipparrone "Liquid crystal based polarization gratings for spectro-polarimetric applications" *Molecular Crystals and Liquid Crystals*, 558, 109-119 (2012).

3. E. Lepera, P. Rizzo, G. Guerra. "Melt Extruded Films of a Commercial Polymer with Intense Chiral Optical Response of Achiral Guests " submitted to *ACS Photonics* (2013).

4. P. Rizzo, E. Lepera, G. Guerra. "Molecular and Supramolecular Circular Dichroism of non-racemic guests of polymeric co-crystalline films" submitted to *ACS* (2013).

5. Post Graduate Master in designing, molding and characterization of new polyolefin based engineering thermoplastics.
   Project Partnership:
   Treofan Group, leader in films for packaging
   Sapa, plastic knowledge leading company
   Fiat, group automobiles
   CRdc tecnologie Scarl
   University of Naples "Federico II"
   University of Salerno.

List of conferences:

1. P. Pagliusi, E. Lepera, C. Provenzano, A. Mazzulla and G. Cipparrone "Polarization gratings allow for real-time and artifact-free circular dichroism measurements". Contribution to *International school of Liquid Crystals* poster session**,** 3-10/07 2011 Erice (Italy).

2. *6th International conference on times of polymers (TOP) & composites,* June 10-14/6 2012 Ischia (Italy).

3. E. Lepera, P. Pagliusi, C. Provenzano and G. Cipparrone "Photorefractivity in chiral azopolymers". Contribution to *13th International Symposium on Colloidal and Molecular Electrooptics* poster session, 2-5/09 2012 Gent (Belgium).

4. ISOPSC 2012 *"New and Old Polymers for Sustainable Chemistry",* 5–7/9 2012 Dipartimento di Chimica e Biologia, University of Salerno (Italy).

5. P. Rizzo, E. Lepera, G. Guerra "Chiral optical response of strereoregular crystalline polymers and of their achiral guests". Oral presentation *Natta's Seeds Grow*, 21-22/11 2013. Politecnico di Milano (Italy)

La scienza è un importante strumento
di conoscenza. L'errore è
pensare che sia il solo.

T. Terzani